Multiscale Modeling & Virtual Sensing for Structural Health Monitoring

by

Chuntao Luo

A Dissertation Presented in Partial Fulfillment
of the Requirements for the Degree
Doctor of Philosophy

Approved June 2011 by the
Graduate Supervisory Committee:

Aditi Chattopadhyay, Chair
Lenore Dai
Hanqing Jiang
Antonia Papandreou-Suppappola
Jian Li

ARIZONA STATE UNIVERSITY

August 2011

ABSTRACT

Damage assessment and residual useful life estimation (RULE) are essential for aerospace, civil and naval structures. Structural Health Monitoring (SHM) attempts to automate the process of damage detection and identification. Multiscale modeling is a key element in SHM. It not only provides important information on the physics of failure, such as damage initiation and growth, the output can be used as "virtual sensing" data for detection and prognosis. The current research is part of an ongoing multidisciplinary effort to develop an integrated SHM framework for metallic aerospace components.

In this thesis a multiscale model has been developed by bridging the relevant length scales, micro, meso and macro (or structural scale). Micro structural representations obtained from material characterization studies are used to define the length scales and to capture the size and orientation of the grains at the micro level. A microvoid model accounting for size and crystal orientation effects is developed first. Parametric studies are conducted to estimate material parameters used in this constitutive model. Numerical and experimental simulations are performed to investigate the effects of Representative Volume Element (RVE) size, defect area fraction and distribution. A multiscale damage criterion accounting for crystal orientation effect is developed next. This criterion is applied for fatigue crack initial stage prediction. A damage evolution rule based on strain energy density is modified to incorporate crystal plasticity at the microscale (local). A damage tensor is derived using optimization theory to characterize the local damage state. The micro scale damage information is passed

from local to grain level, bridging microscale and mesoscale, in the form of a damage vector via averaging techniques. Finally, the damage evolution rule for a meso RVE, which contains several grains, is calculated by modifying the Kreisselmeier-Steinhauser (KS) function, which is used in multiobjective optimization applications, to obtain lower and upper bounds of damage envelopes. The weighted averaging method is also used to obtain the corresponding damage evolution direction for the meso RVE. A critical damage value is derived to complete the damage criterion for fatigue life prediction in Aluminum 2024 test articles. A wave propagation model is incorporated with the damage model to detect changes in sensing signals due to plastic deformation and damage growth.

To

my mom Wenhui Deng and dad Changgeng Luo

all my family and my friends

ACKNOWLEDGMENTS

It is a pleasure to express my sincere thankfulness to all who encouraged and supported me during my Ph.D. studies at Arizona State University. I would like to thank my parents, Wenhui Deng and Changgeng Luo, at the first place for inculcating me the principles to work and to be better human beings.

I owe my deepest gratitude to my advisor, Dr. Aditi Chattopadhyay, whose encouragement, guidance and support from beginning to end enabled me to understand my research. She always encouraged me to participate and to present my work in different conferences, where I can be aware of other researchers' work in my filed and get inspirations and suggestions from different perspectives. It is an honor for me to say that she is not only my thesis advisor, but also a great mentor.

I would like to thank Dr. Pedro Peralta for his technical and experimental support in this research. His knowledge of material science and metallurgy helped me to fundamentally understand the material used in my study. This thesis would not have been possible without his constructive suggestions.

I would like to show my gratitude to Dr. Hanqing Jiang for his help in the development of the size-dependent void model, and to Dr. Jun Wei for teaching me how to use ABAQUS. I also would like to thank Dr. Antonia Papandreou-Suppappola for her suggestions. My special thanks to my committee members, Dr. Lenore Dai, and Dr. Jian Li for their participation in the completion of my degree. I also would like to thank Kay Vasley for all her help. Future more, I am indebted to my many of my colleagues to support me.

This project is supported by the Department of Defense, AFOSR Multidisciplinary University Research Initiation (MURI) program, FA95550-06-1-0309. I would like to convey my gratefulness to the program managers, Dr. Victor Giurgiutiu and Dr. David Stargel, and all the advisory board members for their useful feedback which keeps our research in the right direction.

TABLE OF CONTENTS

Page

LIST OF TABLES ix

LIST OF FIGURES x

CHAPTER

Chapter 1 Introduction 1

1.1 Motivation 1

1.2 Multiscale Modeling 3

1.3 Damage Model 5

1.4 Objectives of the Work 7

1.5 Outline of the Thesis 8

Chapter 2 Constitutive Model 10

2.1 Introduction 10

2.2 Single crystal plasticity 10

2.3 Time integration scheme & incremental formulation 14

2.4 User-defined material subroutine 16

2.5 Numerical Results 18

2.6 Parametric study 23

2.7 Concluding Remarks 28

Chapter 3 Size-Dependent Void Model 30

3.1 Introduction 30

3.2 Taylor Dislocation Model 33

3.3 Damage Model Accounting for Size & Orientation Effects 35

Page

3.3.1 Continuum Model with Cylindrical Microvoid 37

3.3.2 Continuum Model with Spherical Microvoid 41

3.4 Simulation Studies 44

3.5 Concluding Remarks 50

Chapter 4 Single Crystal-Based Damage Model 51

4.1 Introduction 51

4.2 Constitutive Model 52

4.3 Multiscale Damage Criterion 53

4.3.1 Damage Criterion for Crystalline Material 53

4.3.2 Microscale Damage Tensor 57

4.3.3 Mesoscale Damage Vector 62

4.3.4 Critical Damage Value for Crack Nucleation 66

4.4 Results & Validation 67

4.4.1 Lug Joint Fatigue Tests 67

4.4.2 Lug Joint Numerical Simulations 68

4.4.3 Cruciform Fatigue Tests 77

4.4.4 Experiment Setup & Fatigue Tests 81

4.4.5 Cruciform Simulation Results 84

4.5 Concluding Remarks 91

Chapter 5 Virtual Sensing 92

Page

5.1 Introduction 92

5.2 Physics-based Multiscale Model 94

5.3 Virtual Sensing 95

5.3.1 Finite Element Model 95

5.3.2 Experiment Setup 99

5.4 Results 101

5.5 Concluding Remarks 105

Chapter 6 Summary and Future Directions 107

6.1 Summary 107

6.2 Innovative Nature of the Research 110

6.3 Future Directions 111

REFERENCES 113

LIST OF TABLES

Table Page

2.1 Material properties used in copper FCC structure 18

2.2 Material properties used for Al2024 19

3.1 Comparison of elastic stiffness for different damaged structures 46

3.2 Elastic stiffness reduction for different crack lengths 49

4.1 Normal and slip direction of the critical slip system 56

4.2 Eigenvector corresponding to the maximum eigenvalue of deviatoric part ... 61

4.3 Twelve slip systems 61

4.4 No. of cycles for 1mm crack in Lug joint fatigue tests 67

4.5 Average grain size and estimation of failure for different meso RVEs 75

4.6 Fatigue tests to 1mm crack 84

4.7 Simulation results about failure of meso RVE 90

5.1 Material properties of Al 6061, adhesive layer & piezoelectric material 98

LIST OF FIGURES

Figure Page

1.1 Integrated Structural Health Monitoring Framework 3

2.1 Multiplicative decomposition of deformation gradient 11

2.2 Flowchart of UMAT 16

2.3 Crystal orientation and loading direction..... 20

2.4 Cyclic loading condition 20

2.5 Stress-strain response..... 20

2.6 Accumulated shear strain 20

2.7 EBSD Scan..... 21

2.8 Finite Element model..... 21

2.9 Load image in OOF 21

2.10 Pixel selection to group grains..... 22

2.11 (a) Mises stress distribution; (b) Stress-strain response in different grains .. 23

2.12 Stress-strain curve for simple tension test 24

2.13 RVE containing 167 grains for parametric study 25

2.14 Parametric study reevaluating parameters used in Asaro's hardening rule .. 25

2.15 Stress-strain curve for cyclic loading test 26

2.16 Comparison between compression and tension 26

2.17 Deformation of the sample..... 27

2.18 Parametric study for cyclic loading 28

3.1 Cylindrical microvoid with two slip systems..... 39

3.2 Dimensionless flow stress vs microvoid growth rate D..... 40

Figure Page

3.3 Dimensionless flow stress vs slip system orientation 40

3.4 Three activated slip systems 42

3.5 The flow stress vs microvoid growth rate D 43

3.6 The flow stress vs spherical coordinate θ 43

3.7 The flow stress vs spherical coordinate ϕ 44

3.8 Mises stress distribution 47

3.9 Comparison of stress-strain curve 47

3.10 Undamaged structure 47

3.11 Structure with void 47

3.12 Comparison of stress-strain curve 48

3.13 Healthy structure (Case1) and different damaged structures (Case2-5) 48

3.14 Crack length effect on material degradation 49

3.15 Elastic stiffness vs. RVE size 50

4.1 Finite Element model 55

4.2 Accumulative shear strain in 12 slip systems 56

4.3 Fatigue damage evolution in 12 slip systems 56

4.4 X-Y plane projection of the normal 57

4.5 Simulation for simple tension on a pre-cracked single crystal plate. 60

4.6 SEM micrograph showing the slip prior to the crack tip 61

4.7 KS function 63

4.8 Lab setup for fatigue tests 68

4.9 Finite element mesh of lug joint 69

Figure Page

4.10 Mises stress distribution of lug joint 70

4.11 (a) Damage evolution in each grain; (b) Linear damage growth 71

4.12 (a) Damage distribution in grains; (b) Location of critical grain 71

4.13 Microstructure and grain size distribution of the meso RVE 73

4.14 Normalized damage index for meso RVE vs. No. of cycles 73

4.15 (a) Histogram of damage direction; (b) Cracking directions 74

4.16 Finite element meshes of different lug joints 74

4.17 (a) Direct EBSD scan; (b) Finite element meshes created from OOF 76

4.18 Crack reaches 1.5 mm 76

4.19 Histogram for potential crack direction 77

4.20 Detail dimensions of the cruciform specimen 79

4.21 (a) A quarter part of the cruciform specimen; (b) Mises stress distribution in the cruciform quarter part under equibiaxial loading 79

4.22 Cruciform specimen with a hole at the center for fatigue test 80

4.23 Cruciform specimen with a 45o notch at the center hole for fatigue test 80

4.24 (a) Two length scale mesh of cruciform specimen; (b) Enlarged image of mesh at the hole; (c) Enlarged image of mesh at the tip of the notch 81

4.25 Experiment setup 82

4.26 Crack propagation in cruciform sample 82

4.27 Fatigue experiment 82

4.28 Initial crack directions in four fatigue tests 83

4.29 (a) Refined mesh; (b) Mises stress distribution around the notch tip 85

Figure Page

4.30 Damage evolution in each grain for 20 cycles 89

4.31 Damage index growth of meso RVE 89

4.32 Potential crack direction obtained from simulation 90

4.33 Crack direction from fatigue test 90

5.1 (a) Six selected locations; (b) Damage information of the six locations 95

5.2 Finite element model of the Al 6061 plate 97

5.3 (a) Finite element mesh; (b) boundary condition used for the analysis 98

5.4 Dimensions of a plate made of Al 6061 in inches 100

5.5 Data acquisition system 100

5.6 Comparison between simulated sensing signal with experiment data 102

5.7 Propagation of Lamb waves in plate at three different times 103

5.8 Comparison between sensing signals with/without RVE 103

5.9 (a) Sensing signal comparison between loading/unloading case and healthy sample; (b) Enlarged subtraction 104

5.10 (a) Sensing signal comparison between 10 cyclic loading case and healthy sample; (b) Enlarged subtraction 105

Chapter 1

Introduction

1.1 Motivation

Damage detection and condition monitoring of aerospace vehicles with a view to improve safety and reliability have always been associated with significant labor and economic costs. Past investigations have consistently relied on empirical models, non-destructive evaluation (NDE) techniques, and observations, rather than acquiring a fundamental understanding of structural health monitoring concepts [1, 2]. Over the last few years, however, Structural Health Monitoring (SHM), has emerged as an exciting new field of multidisciplinary investigations, with academic conferences and scientific journals that are devoted today exclusively to SHM [3-7] issues.

While the use of SHM technologies is becoming increasingly common, there is a need to develop a comprehensive framework for damage identification strategies that successfully address the structural reliability and sustainability of critical components. The applications include aerospace, civil, and mechanical infrastructure. An integrated framework that includes modeling, sensing, detection, and information management (Fig. 1.1) is currently being developed by Chattopadhyay and her research group [8]. As shown in Fig. 1.1, the sensing portion of SHM involves selection of sensor and their optimal placement, damage detection methodologies, data acquisition and signal processing approaches. The goal of this element in SHM is to detect the smallest possible damage in a structure. Although considerable research has been conducted on developing

different sensing techniques [9-12], existing sensors pose considerable limitation on the size of detectable damage. This problem can be overcome by a modeling-based virtual sensing technique. Results from a multiscale modeling technique which is capable of tracking damage initiation at the microscale and providing damage information at the macroscale, can be used in conjunction with data from physical sensors, resulting in a hybrid data base for damage detection. The decision making component can use the hybrid data base to isolate, quantify and classify damage. Finally, the information can be fed to the prognosis module for predicting damage evolution and most importantly to estimate the residual useful life of a system.

In this thesis, effort has been dedicated to develop a physics-based multiscale modeling approach and associated damage criterion for the estimation of damage initiation and propagation which is essential to diagnosis and prognosis. Important issues regarding different length and time scales, anisotropic behavior at microscale due to crystal orientation effect, and grain size effect are addressed in this research. Background of relevant research is discussed in the following sections.

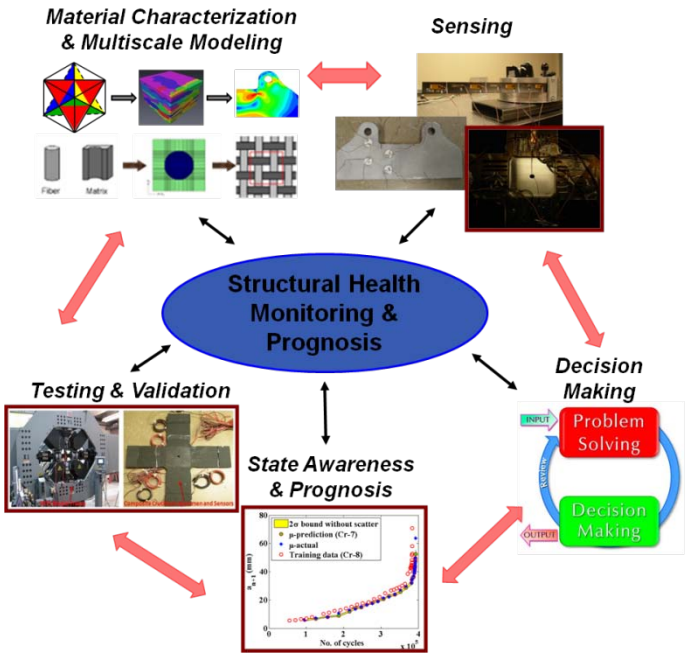

Figure 1.1 Integrated Structural Health Monitoring Framework

1.2 Multiscale Modeling

Cyclic loading is one of the common loading conditions for aerospace vehicles [13]. The associated phenomenon of fatigue inherently involves multiple scales due to the presence of microcracks (initiation and growth at microscale) or inclusions which can lead to structural damage and subsequent failure. Therefore, it is necessary to develop a scale-dependent, physics-based model for accurate simulation in order to understand material performance/degradation in various operational environments and to ultimately assess the survivability of aerospace vehicles. This scale associated modeling approach, referred as multiscale modeling, must address important features at different scales, including multiple spatial and/or temporal scales. A review of multiscale modeling techniques

addressing the different elements such as mechanics, mathematics, physics, numerical methods, and material science can be found in Ref. 14.

A significant amount of research has been conducted on multiscale modeling [15-21]. For instance, the hierarchical approach based on the bottom-up description of the material structure has proved to be successful in a wide range of applications [16-19]. Unit representative cells are identified based on a multi-scale decomposition of the material microstructure. A single macroscopic constitutive relation is built hierarchically from one scale to another using cell-averaging technique. Microstructure parameters are included as variables in the resulting relation. An alternative approach to the homogenization is provided by the global–local analysis [20, 21]. In this approach, the material response at a point is calculated simultaneously with the global simulation by performing a cell model. The key advantage of this method is that a homogenized constitutive relation is not needed, and therefore, no empirical determination of material constants is required. However, this class of method does not start from material characterization. The microstructures used in such approaches are generated by Voronoi diagram which neglects the real grain size and shape effects. In addition, microvoids are arbitrarily introduced in the structure. Thus, the damage initiation is not considered in those models.

In this thesis, multiscale modeling approach is developed by addressing a material constitutive relations and damage evolution model at relevant length scales. The research starts from the material characterization to incorporate microstructural accurate information. The effects of grain orientation and size on

the material mechanical response at microscale and the grain distribution effect on the damage evolution are studied in detail. The developed framework is capable of predicting damage initiation and growth, including the failure of representative volume element (RVE) at meso scale.

1.3 Damage Model

Structures under cyclic loading often exhibit fatigue damage and subsequent failure. An early description of fatigue damage can be found in the work of Ewing and Humfrey [22]. They found that repeated alterations of stress in metals showed up in the form of slip-lines on crystals that were very similar in appearance to those that occurred in simple tension tests. Further loading resulted in appearance of additional slip-lines. After many cycles, the slip-lines changed into comparatively wide bands and continued to broaden as the number of cycles increased. Cracks occurred along broadened slip-bands from crystal and soon coalesced to form a long continuous crack across the surface of the specimen. Once the long crack developed, it took a few more cycles of loading to cause fatigue fracture. Therefore, it can be concluded that fatigue damage is a result of material structural change at the microscale. Thus, a comprehensive fatigue damage model should include important microscale features of the material, such as grain orientations, and reflect changes of those features at macroscale. In addition, engineering structural components are usually subjected to varying loads of different amplitudes and frequencies along different directions. This will give

rise to biaxial or multiaxial stress state and a prediction of fatigue life should consider such loading condition for reliable assessment.

Considerable research efforts have been devoted to developing methodology for modeling fatigue damage [23]. Many researchers have dedicated efforts to developing fatigue criteria over the years. A comprehensive overview on fatigue criteria is found in [24]. In general, fatigue criteria can be categorized roughly according to the physical quantity upon which the criteria are based. Depending on different fatigue damage mechanisms, fatigue criteria are developed as based on stress, energy, and fracture mechanics. In earlier research, stress or plastic strain amplitudes were adopted for fatigue life prediction. For example, Gough et al. [25, 26] proposed empirical relationships that reduce to shear stress for ductile materials and principal stress for brittle materials. Since fatigue damage is found to be primarily driven by plastic strain energy, this parameter was believed to be a rational parameter for fatigue damage evaluation. However, most early attempts of fatigue model development based primarily on the energy concept without considering loading history related parameters seem unsatisfactory [24]. Modifications are also needed to apply those models for complex loading conditions such as multiaxial loading, and non-proportional loading.

The work presented in this thesis is focused on developing a multiscale fatigue damage criterion incorporated with single crystal plasticity. This criterion can be classified as energy based since the damage parameter is directly related to the plastic strain energy density. Two important aspects are addressed in this criterion: i) relating damage to the material microstructure features; ii) applicable

to multiaxial loading without modification. The derivation of the multiscale fatigue damage criterion and some applications of this damage model for different structural components and load conditions are presented in the chapter 4.

1.4 Objectives of the Work

The present work aims at the following objectives:

1) Implement a single crystal plasticity theory at microlevel, and modify a user defined material subroutine (UMAT) to incorporate kinematic and isotropic hardening into this model.
2) Develop a size-dependent void model.
3) Determine key material parameters via a parametric study.
4) Investigate effects of representative volume element (RVE) size and defect area fraction and distribution on material properties via numerical simulations.
5) Incorporate a fatigue damage criterion for single crystal plasticity and develop damage tensor at the microscale based on the energy density concept. The formulation of damage tensor involves selecting the optimal set of equations, relating damage parameter to damage tensor.
6) Develop a damage vector at mesoscale, which indicates the amount of damage and direction of damage evolution simultaneously using weighted averaging techniques and the Kreisselmeier-Steinhauser function.

7) Perform damage analysis using multiscale modeling and develop multiscale damage criterion in lug joints under uniaxial loading and in cruciform sample under biaxial loading.
8) Incorporate the multiscale damage model in a wave propagation model for virtual sensing.

1.5 Outline of the Thesis

The thesis is structured as follows. Six chapters are presented.

Chapter 2 provides an introduction to single crystal plasticity theory. The main governing equations are presented. A nonlinear kinematic hardening rule of the Armstrong-Frederick type and isotropic hardening is added to the single crystal plasticity theory. Then the forward gradient time integration scheme and incremental formulation are provided followed by the UMAT algorithm. Procedures to construct the 2D microstructure from Electron Backscattering Diffraction (EBSD) scans are discussed. Details of the parametric studies conducted to find the key material parameters are presented.

Chapter 3 presents the development of a void model accounting for the size and orientation effects. Different shapes of microvoids are studied by applying the size-dependent void model. Results from a simulation study conducted to investigate the effects of RVE size and defect area fraction and distribution on material performance is also presented.

Chapter 4 starts with an introduction of a comprehensive fatigue damage criterion that can be applied for multiaxial and nonproportional loading. For

computational efficiency, the damage criterion is modified incorporating single crystal plasticity. Damage parameters within the 12 slip systems are calculated at each integration point and are used to construct a damage tensor at the microscale. Average and optimization techniques, used to bring the key damage parameters from microscale to mesoscale, are discussed. Details of derivation for the mesoscale damage parameter from the microscale are presented. Applications of the damage criterion in lug joint and cruciform sample under different load conditions are shown at the end of this chapter.

Chapter 5 presents the virtual sensing technique by incorporating the wave propagation model with the multiscale model. The determinations of maximum element size and time increment are presented in this chapter. Preliminary results on some initial investigation of sensing signal change due to microstructure under different load conditions are also presented.

Chapter 6 summarizes the work reported in this thesis and the innovative contributions made in this research in multiscale damage modeling and finite element based virtual sensing technique are highlighted. Ideas for future work are discussed at the end of the chapter.

Chapter 2

Constitutive Model

2.1 Introduction

One of the most important concerns for crystalline materials is to incorporate microstructure, crystallinitiy, and micromechanics into the continuum description of finite strain plasticity. The subject has led to the development of a sound physical and mathematical foundation where the work of Taylor [27, 28] is considered a significant contribution. Taylor discovered that crystal dislocation provided a clear atomistic interpretation of the slip process and strain hardening, demonstrating that micromechanics could be incorporated into a macroscopic analysis of plastic flow. Hill, Rice, Asaro, and Bassani [29-35] extended this theory by demonstrating that crystal plasticity did, in fact, incorporate important micromechanical features of plastic flow into macroscopic analysis.

2.2 Single crystal plasticity

The single crystal plasticity theory is used to capture crystallographic orientation effects not considered by classical isotropic models of metal plasticity. The kinematic theory for single crystal deformation presented here follows the pioneering work of Taylor [28] and its precise mathematical theory developed by Hill, Hill and Rice, and Asaro [29-34]. It starts from the deformation gradient $\mathbf{F} = \partial \mathbf{x}/\partial \mathbf{X}$, where the deformation gradient is decomposed into elastic and plastic components (shown in Fig. 2.1) under the standard multiplicative

decomposition assumption. Equation (2.1) shows the formula to decompose the deformation gradient.

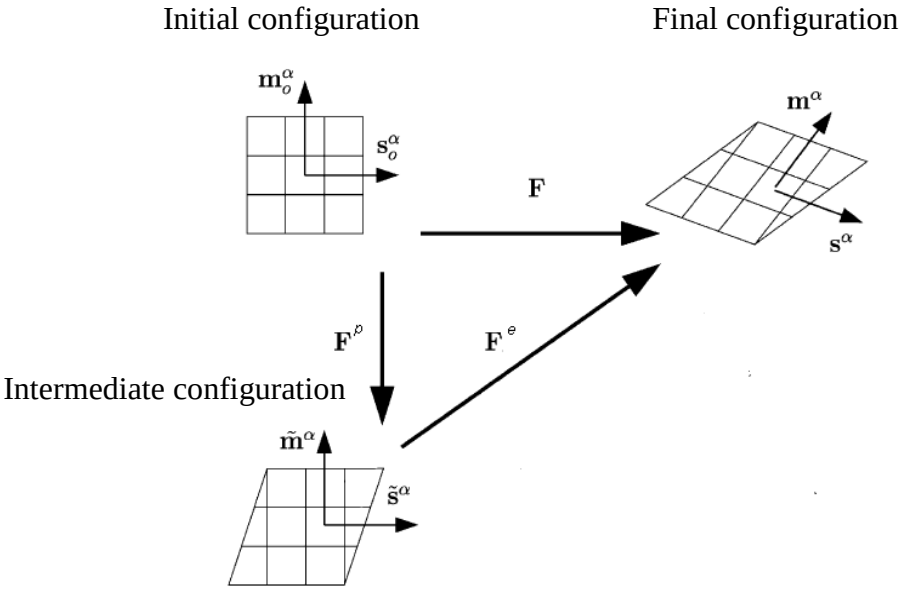

Figure 2.1 Multiplicative decomposition of deformation gradient

$$\mathbf{F} = \mathbf{F^e} \cdot \mathbf{F^p} \tag{2.1}$$

where $\mathbf{F^p}$denotes plastic deformation of the material in an intermediate configuration in which the lattice orientation and spacing remain the same as in the reference configuration. $\mathbf{F^e}$denotes the elastic component of the deformation gradient, which includes stretching and rotation of the lattice. The velocity gradient, $\mathbf{L} = \partial \mathbf{v} / \partial \mathbf{x}$, in the current configuration is related to the deformation gradient by:

$$\mathbf{L} = \dot{\mathbf{F}}\mathbf{F^{-1}} = \mathbf{L^e} + \mathbf{L^p} \tag{2.2}$$

where $\mathbf{L^e} = \dot{\mathbf{F}}^\mathbf{e}\mathbf{F^{e-1}}$ and $\mathbf{L^p} = \mathbf{F^e}\dot{\mathbf{F}}^\mathbf{p}\mathbf{F^{p-1}F^{e-1}}$ represent the elastic and plastic components of the velocity gradient, respectively.

Assuming that the inelastic deformation of a single crystal arises solely from the crystalline slip, the plastic velocity gradient can be rewritten in terms of the resolved slip rate $\dot{\gamma}^{(\alpha)}$, the slip direction $\mathbf{s}^{(\boldsymbol{\alpha})}$, and the normal $\mathbf{m}^{(\boldsymbol{\alpha})}$ to the slip plane as below:

$$\mathbf{L}^{\mathbf{p}} = \sum_{\alpha} \dot{\gamma}^{(\alpha)} \mathbf{s}^{(\boldsymbol{\alpha})} \otimes \mathbf{m}^{(\boldsymbol{\alpha})} \tag{2.3}$$

where $\boldsymbol{\alpha}$ denotes the $\boldsymbol{\alpha}$ th slip system. The resolved shear stress, which plays a vital role in promoting slip, has been derived from the Cauchy stress tensor and is given by:

$$\tau^{(\boldsymbol{\alpha})} = \boldsymbol{\sigma} : (\mathbf{s}^{(\boldsymbol{\alpha})} \otimes \mathbf{m}^{(\boldsymbol{\alpha})})_{\mathbf{sym}} \tag{2.4}$$

It is important to note that the slip direction and the vector normal to the slip plane used in Eqn (2.4) are defined for the deformed configuration, but not for the reference configuration. The slip direction and normal vector for the deformed configuration can be expressed in terms of the reference configuration as follows:

$$\mathbf{s}^{(\boldsymbol{\alpha})} = \mathbf{F}^{\mathbf{e}} \mathbf{s_0}^{(\boldsymbol{\alpha})} \text{ and } \mathbf{m}^{(\boldsymbol{\alpha})} = \mathbf{m_0}^{(\boldsymbol{\alpha})} \mathbf{F}^{\mathbf{e-1}} \tag{2.5}$$

The velocity gradient in the current state can be decomposed into the symmetric rate of stretching tensor $\mathbf{D}$ and the antisymmetric spin tensor $\boldsymbol{\Omega}$ as follows:

$$\mathbf{L} = \mathbf{D} + \boldsymbol{\Omega} \tag{2.6}$$

Furthermore, the stretching and spin tensor can be decomposed into lattice part and plastic part, respectively:

$$\mathbf{D} = \mathbf{D}^{l} + \mathbf{D}^{p} \text{ and } \boldsymbol{\Omega} = \boldsymbol{\Omega}^{l} + \boldsymbol{\Omega}^{p} \tag{2.7}$$

Satisfying:

$$\mathbf{D}^l + \mathbf{\Omega}^l = \dot{\mathbf{F}}^{\mathbf{e}} \cdot \mathbf{F}^{\mathbf{e-1}}$$
$$\mathbf{D}^p + \mathbf{\Omega}^p = \sum_{\alpha} \dot{\gamma}^{(\alpha)} \mathbf{s}^{(\alpha)} \otimes \mathbf{m}^{(\alpha)} \tag{2.8}$$

Following Hill and Rice's work, the stretching tensor and the Jaumann rate of Cauchy stress $\tilde{\boldsymbol{\sigma}}$ have the following relation:

$$\tilde{\boldsymbol{\sigma}} + \boldsymbol{\sigma}(\mathbf{I}: \mathbf{D}^l) = \mathbf{L}: \mathbf{D}^l \tag{2.9}$$

A power-law is used in the flow rule to calculate the slip increments, as follows [36, 37]:

$$\dot{\gamma}^{(\alpha)} = \dot{\gamma_0}^{(\alpha)} \left| \frac{\tau^{(\alpha)} - \chi^{(\alpha)}}{g^{(\alpha)}} \right|^n sign(\tau^{(\alpha)} - \chi^{(\alpha)}) \tag{2.10}$$

where $\dot{\gamma_0}^{(\alpha)}$ is the reference strain rate on slip system $\boldsymbol{\alpha}$, n is the strain rate exponent, $g^{(\alpha)}$and $\chi^{(\alpha)}$ represent the isotropic and kinematic hardening, respectively. The hardening law for $g^{(\alpha)}$ and $\chi^{(\alpha)}$ are presented below:

$$\dot{g}^{(\alpha)} = \sum_{\beta} h_{\alpha\beta} \dot{\gamma}^{\beta} \tag{2.11}$$

$$\dot{\chi}^{(\alpha)} = b\dot{\gamma}^{(\alpha)} - r\chi^{(\alpha)} \left| \dot{\gamma}^{(\alpha)} \right| \tag{2.12}$$

where $h_{\alpha\beta} = \begin{cases} h(\gamma) = h_0 \, \mathbf{sech^2} \left| \frac{h_0 \gamma}{\tau_s - \tau_0} \right|, & \alpha = \beta \\ q h(\gamma), & \alpha \neq \beta \end{cases}$ are called self and latent hardening moduli, respectively. b, r, and q are material constants, h_0 is the initial hardening modulus, τ_s is the stage I stress, and τ_0 is the yield stress. The cumulative shear strain on all slip systems can be obtained by:

$$\gamma = \sum_{\alpha} \int_0^t \left| \dot{\gamma}^{(\alpha)} \right| dt \tag{2.13}$$

The details of hardening for crystalline materials can be found in the work of Asaro [33, 34, 38].

2.3 Time integration scheme & incremental formulation

Huang's implementation of the single crystal plasticity theory using the user-material subroutine (UMAT) [39], has been used in this research. This procedure is summarized in this section. The tangent modulus method for rate dependent solid developed by Peirce, Shih, and Needleman [40] is implemented in the UMAT. The linear interpolation within a time increment Δt is as follows:

$$\Delta\gamma^{(\boldsymbol{\alpha})} = \Delta t[(1-\theta)\dot{\gamma}_t{}^{(\alpha)} + \theta\dot{\gamma}_{t+\Delta t}{}^{(\alpha)}] \tag{2.14}$$

The parameter θ , ranging from 0 to 1, controls the interpolation scheme. When $\theta = 0$, the Eqn. (2.14) returns to the simple Euler time integration scheme. When $\theta = 1$, it becomes fully implicit integration scheme. A value of $\theta = 0.5$ is chosen for all simulations in this research following the recommendation from Peirce's work [40].

The resolved shear stress increment $\Delta\boldsymbol{\tau}^{(\boldsymbol{\alpha})}$ can be obtained from Eqn. (2.4), (2.7), (2.8) and the elastic constitutive law (Eqn. (2.9)):

$$\Delta\tau^{(\boldsymbol{\alpha})} = \left[C_{ijkl}\mu_{kl}^{(\alpha)} + \omega_{ik}^{(\alpha)}\sigma_{jk} + \omega_{jk}^{(\alpha)}\sigma_{ik}\right] \cdot \left[\Delta\varepsilon_{ij} - \sum_{\beta}\mu_{ij}^{(\beta)}\Delta\gamma^{(\beta)}\right] \tag{2.15}$$

where **C** is the elastic stiffness tensor, μ is the Schmid factor and ω is a tensor related to the spin tensor **Ω**. These can be expressed in terms of the slip direction and normal of each slip system as follows:

$$\mu_{ij}^{(\alpha)} = \frac{1}{2}\left[s_i^{(\alpha)} m_j^{(\alpha)} + s_j^{(\alpha)} m_i^{(\alpha)}\right] \tag{2.16}$$

$$\omega_{ij}^{(\alpha)} = \frac{1}{2}\left[s_i^{(\alpha)} m_j^{(\alpha)} - s_j^{(\alpha)} m_i^{(\alpha)}\right] \tag{2.17}$$

The increments of current hardening function $\Delta g^{(\boldsymbol{\alpha})}$ are derived from Eqn. (2.11):

$$\Delta g^{(\boldsymbol{\alpha})} = \sum_{\beta} h_{\alpha\beta} \Delta\gamma^{(\beta)} \tag{2.18}$$

In general, the slip rate $\dot{\gamma}^{(\boldsymbol{\alpha})}$ is a function of the resolved shear stress $\tau^{(\boldsymbol{\alpha})}$ and the current strength $g^{(\boldsymbol{\alpha})}$, which yields:

$$\dot{\gamma}_{t+\Delta t}{}^{(\alpha)} = \dot{\gamma}_t{}^{(\alpha)} + \frac{\partial \dot{\gamma}^{(\alpha)}}{\partial \boldsymbol{\tau}^{(\alpha)}} \Delta\boldsymbol{\tau}^{(\alpha)} + \frac{\partial \dot{\gamma}^{(\alpha)}}{\partial g^{(\boldsymbol{\alpha})}} \Delta g^{(\boldsymbol{\alpha})} \tag{2.19}$$

Thus Eqn. 2.14 becomes:

$$\Delta\gamma^{(\alpha)} = \Delta t[\dot{\gamma}_t{}^{(\alpha)} + \theta \frac{\partial \dot{\gamma}^{(\alpha)}}{\partial \boldsymbol{\tau}^{(\alpha)}} \Delta\boldsymbol{\tau}^{(\alpha)} + \theta \frac{\partial \dot{\gamma}^{(\alpha)}}{\partial g^{(\boldsymbol{\alpha})}} \Delta g^{(\boldsymbol{\alpha})}] \tag{2.20}$$

Therefore the linear solution of $\Delta\gamma^{(\boldsymbol{\alpha})}$ can be obtained by substituting the incremental relations (Eqn. 2.15 & Eqn. 2.18) into Eqn. (2.20). By using Eqn. (2.10), the nonlinear function of $\Delta\gamma^{(\boldsymbol{\alpha})}$ can be obtained as:

$$\begin{aligned} &\Delta\gamma^{(\alpha)} - (1-\theta)\Delta t \dot{\gamma}_t^{(\alpha)} \\ &- \theta \Delta t \dot{\gamma}_0^{(\alpha)} \left| \frac{\tau_t^{(\alpha)} + \Delta\tau^{(\alpha)} - \chi_t^{(\alpha)} - \Delta\chi^{(\alpha)}}{g_t^{(\alpha)} + \Delta g^{(\alpha)}} \right|^n sign\left(\tau_{t+\Delta t}^{(\alpha)} - \chi_{t+\Delta t}^{(\alpha)}\right) \\ &= 0 \end{aligned} \tag{2.21}$$

where $\Delta\chi^{(\alpha)}$ can be calculated through Eqn. (2.12). This nonlinear equation of $\Delta\gamma^{(\boldsymbol{\alpha})}$ is solved using a Newton-Rhapson iterative method, and the linear solution obtained from Eqn. (2.20) is taken as an initial estimation. The details can be

found in Huang's work [39]. The main difference between Huang's work and the work in this dissertation is that the power-law used here includes the kinematic term reflected in the backstresses.

2.4 User-defined material subroutine

ABAQUS is a widely used commercial finite element program. It provides an interface where users can write a subroutine to define their own constitutive model. This user-defined material subroutine referred to as UMAT will provide the material Jacobian matrix, $\boldsymbol{\partial \Delta \sigma / \partial \Delta \varepsilon}$ to update the stresses and the solution dependent state variables values at the end of the increment, once it is called by ABAQUS [41].

Figure 2.2 shows the flowchart of the UMAT subroutine based on single crystal plasticity.

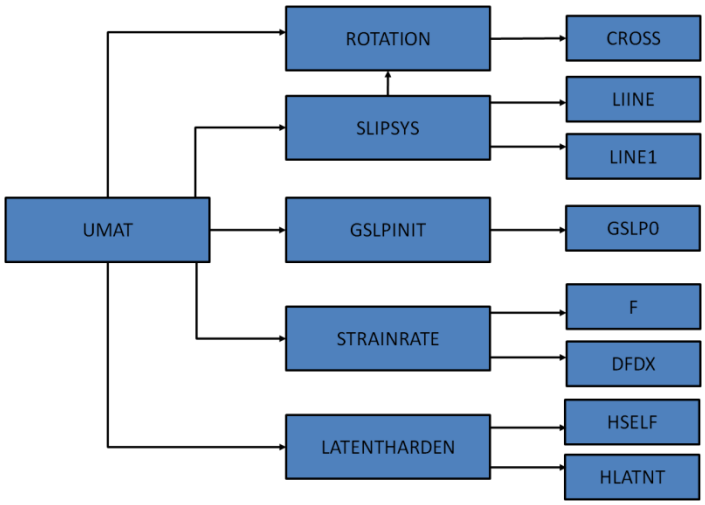

Figure 2.2 Flowchart of UMAT

UMAT--- main subroutine

ROTATION---orientation of local cubic system in global system

CROSS---cross product of two vectors

SLIPSYS---generating all slip systems

LINE---[mmm] type of slip systems

LINE1---[0mn] type of slip systems

GSLPINIT---initial values of current strain hardening functions in all slip systems

GSLP0---user-supplied functional subroutine for the initial value in each system

STRAINRATE---shear strain-rates in all slip systems

F---user-supplied functional subroutines for the shear strain-rate in each system

DFDX---user-supplied functional subroutine for the derivative of function F

LATENTHARDEN---hardening matrix, i.e. self- and latent-hardening in all slip systems

HSELF---user-supplied functional subroutine for the self-hardening modulus

HLATNT---user-supplied functional subroutine for the latent-hardening modulus

2.5 Numerical Results

In order to verify the constitutive model for fatigue analysis, a copper bar has been analyzed in ABAQUS using the UMAT code based on Huang's work [39], using the same material properties listed in Table 2.1.

Table 2.1 Material properties used in copper FCC structure

Elastic moduli	C_{11}=168.4GPa	C_{12}=121.4GPa	C_{44}=75.4GPa	
Material constants in power law	n=10	$\dot{\gamma}_0 = 0.001\text{sec}^{-1}$		
Material constants in hardening	$h_0 = 541.5MPa$	$\tau_s = 109.5MPa$	$\tau_0 = 60.8MPa$	q=1.0

The bottom and left edges of the foremost surface coincide with the crystal [-101] and [010] directions, respectively, and the loading direction is parallel to [101] (Fig. 2.3). Since copper consists of FCC crystal structures, there are well-defined families of slip planes and slip directions, i.e., {111} <110>. A single FCC crystal will contain 12 slip systems, comprised of four slip planes each with three slip directions. Figure 2.4 shows the cyclic load condition (displacement control), and Fig. 2.5 shows the stress-strain response using single crystal plasticity theory. Two important aspects, cyclic hardening and saturation, are clearly exhibited in Fig. 2.5. The accumulated shear strain, which is directly related to the micro-damage, has also been investigated. Figure 2.6 demonstrates that accumulated shear strain increases with the number of cycles. This is an important parameter for fatigue damage studies and will be used in the fatigue damage criterion section to calculate the fatigue damage parameter.

The single crystal plasticity theory applied at the micro level can now be implemented at the meso level. The material used in this research is Al2024. Relevant material parameters are shown in Table 2.2. The material hardening constants used in Asaro's hardening model are adopted from Ref. 34 (shown in Table 2). In the mesoscale model, the original structure contained 547 grains, which is sufficient to be a representative volume element (RVE). Each grain has a single crystal structure. To ensure computation efficiency, the original structure was reduced to a structure with 64 grains by combining smaller grains with larger or similar ones. Smaller grains were chosen using a heuristic approach based on the relative size and orientation of nearby grains; this ensures that no significant effects are excluded. The approach used in this model for fatigue simulation at the meso scale is generalized in the following three steps.

Table 2.2 Material properties for Al2024

Elastic moduli (GPa)	D_{1111}=112 D_{2233}=57.5 D_{3312}=-1.09 D_{3313}= -1.12 D_{2223}=1.86	D_{1122}=59.5 D_{3333}=114 D_{1212}=26.7 D_{1213}=-1.92 D_{3323}=0.068	D_{2222}=114 D_{1112}=1.67 D_{1113}=1.25 D_{1313}= 26.2 D_{1223}=-0.125	D_{1133}=59 D_{2212}=-0.574 D_{2213}=-0.125 D_{1123}=-1.92 D_{1323}= -1.09
	D_{2323}=24.7			
Material constants in power law	n=10	$\dot{\gamma}_0$= 0.001sec^{-1}		
Material constants in self and latent hardening	$h_0 = 8.9\tau_0$	$\tau_s = 1.8\tau_0$	$\tau_0 = 76MPa$	q=1.0

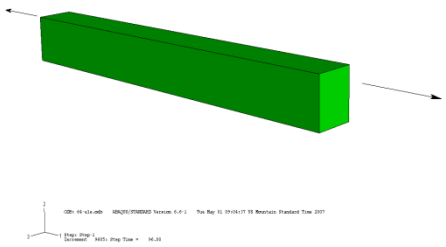

Figure 2.3 Crystal orientation and loading direction

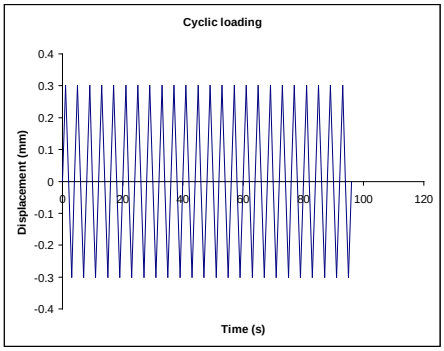

Figure 2.4 Cyclic loading condition

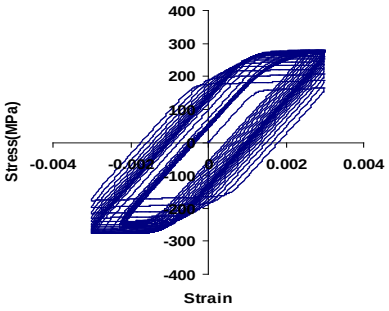

Figure 2.5 Stress-strain response

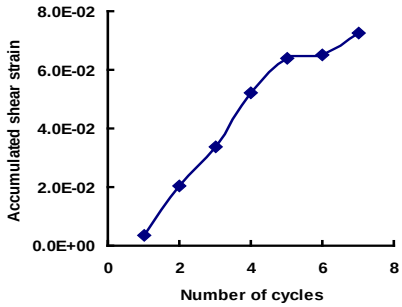

Figure 2.6 Accumulated shear strain

The process begins when Electron Backscattering Diffraction (EBSD) scans (Fig. 2.7) are used to determine the crystal orientations in terms of three Euler angles ($\theta_1, \theta_2, \theta_3$). The following rotation matrix relates the Euler angles to the crystal axes of each grain, which are parallel to the global axes.

$$\begin{pmatrix} \cos(\theta_3)\sin(\theta_1)+\cos(\theta_1)\cos(\theta_2)\sin(\theta_3) & \cos(\theta_1)\cos(\theta_2)\cos(\theta_3)-\sin(\theta_1)\sin(\theta_3) & -\cos(\theta_1)\sin(\theta_2) \\ -\cos(\theta_1)\cos(\theta_3)+\cos(\theta_2)\sin(\theta_1)\sin(\theta_3) & \cos(\theta_2)\cos(\theta_3)\sin(\theta_1)+\cos(\theta_1)\sin(\theta_3) & -\sin(\theta_1)\sin(\theta_2) \\ \sin(\theta_2)\sin(\theta_3) & \cos(\theta_3)\sin(\theta_2) & \cos(\theta_2) \end{pmatrix} \tag{2.22}$$

The rows of the matrix are unit vectors describing the crystallographic axes parallel to the global XYZ axes; therefore, this is the rotation matrix from local axes to global axes.

The next step uses the software package OOF (Object-Oriented Finite), a finite element analysis tool available through National Institute of Standards and Technology (NIST), is used to create and mesh the meso scale structure from the EBSD scan (Fig. 2.8). Grains are represented by various colors and each grain has the same material properties, but different crystal orientations.

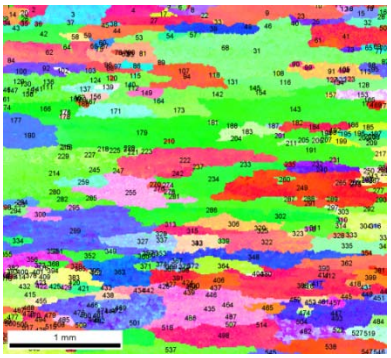

Figure 2.7 EBSD Scan

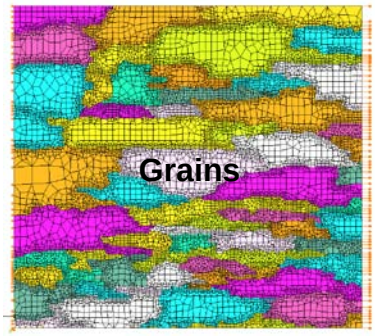

Figure 2.8 Finite Element model

The procedure to use OOF for meshing is:

1. Load a EBSD scan in microstructure page (shown in Fig. 2.9)

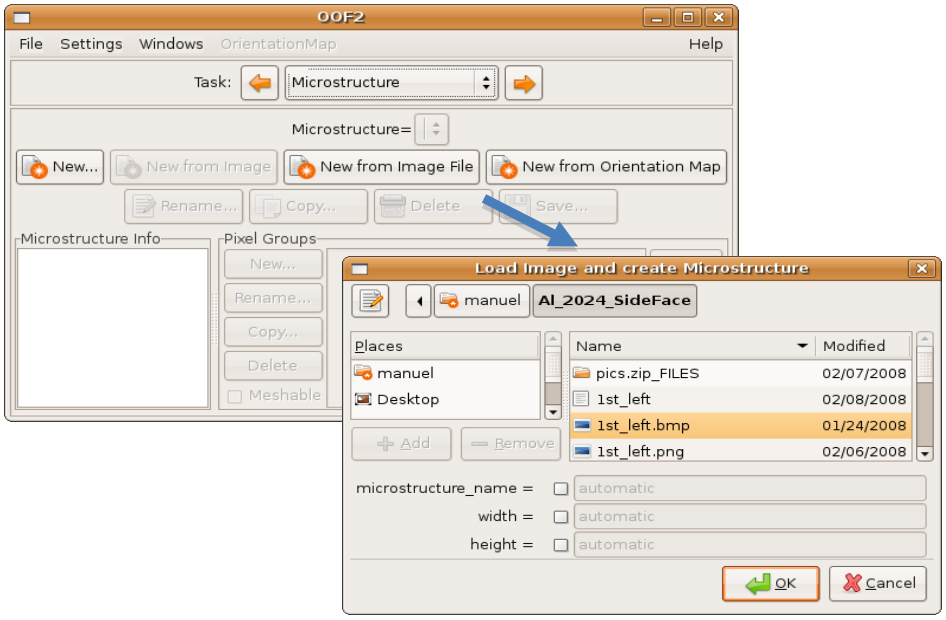

Figure 2.9 Load image in OOF

2. In the graphics window, group each grain by pixel selection as shown in Fig. 2.10

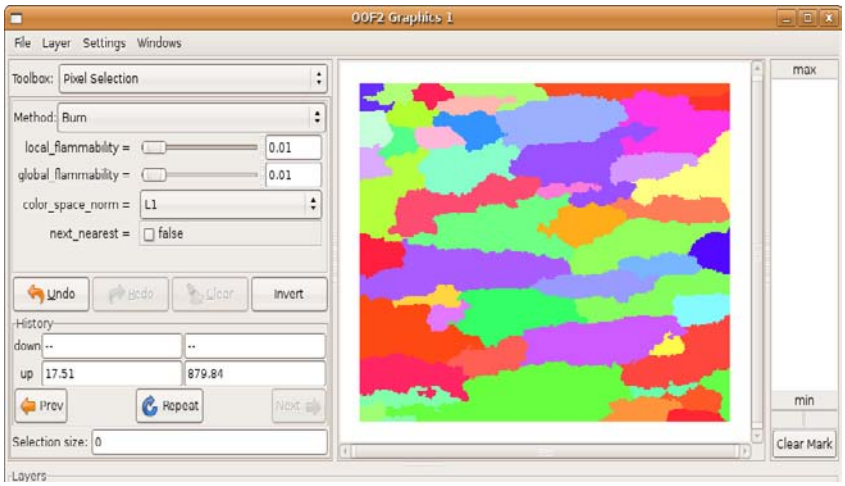

Figure 2.10 Pixel selection to group grains

3. In the Skeleton page, an initial skeleton can be generated. The mesh can be refined by adjusting the value of threshold and alpha. Using the Snap Nodes option and setting the proper value for threshold and alpha, nodes can be fixed at boundaries. Also, interface pixels can be chosen between grains to refine the mesh.

The commercial FEA software ABAQUS and the previously developed UMAT are used to obtain stress distributions and stress-strain responses for individual grains, as shown in Fig. 2.11. The specimen is tested under cyclic displacement control by applying displacement at the right edge of the meso-scale structure. In Fig. 2.11 (a), the cool-colored grains (green and cooler) are still under elastic deformation while the warm-colored grains (yellow and red) experience plastic deformation. This indicates that the material has an anisotropic,

heterogeneous response at the grain level due to different crystal orientations and grain shapes. The stress-strain response of two adjacent grains is presented in Fig. 2.11 (b). From the plots, the indicated adjacent grains exhibit different material behaviors. The red grain has higher stress, but lower strain compared to the other one. This provides evidence that the model used in this research is able to capture the orientation effects on material behavior at the grain level.

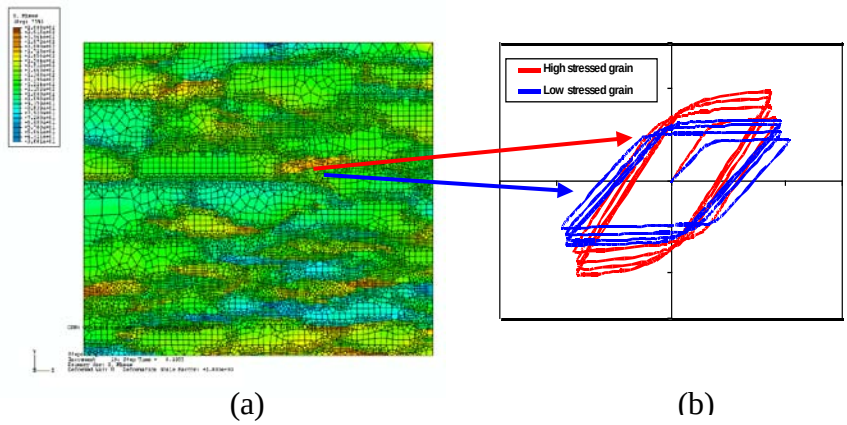

Figure 2.11 (a) Mises stress distribution, (b) Stress-strain response in different grains

2.6 Parametric study

As mentioned in section 2.5, the simulation results show that under similar loading conditions, the material exhibits an anisotropic behavior at the grain level due to different crystal orientations (Fig. 2.11). The result shows a distinct difference in material behavior between the two adjacent grains.

At larger length scales, however, where the anisotropic material behavior is eliminated due to a large number of randomly oriented grains, a homogenous material behavior can be observed at the macroscale. A simple tension test was

conducted on a standard dogbone sample to obtain the global stress-strain curve at the macroscale (shown in Fig. 2.12).

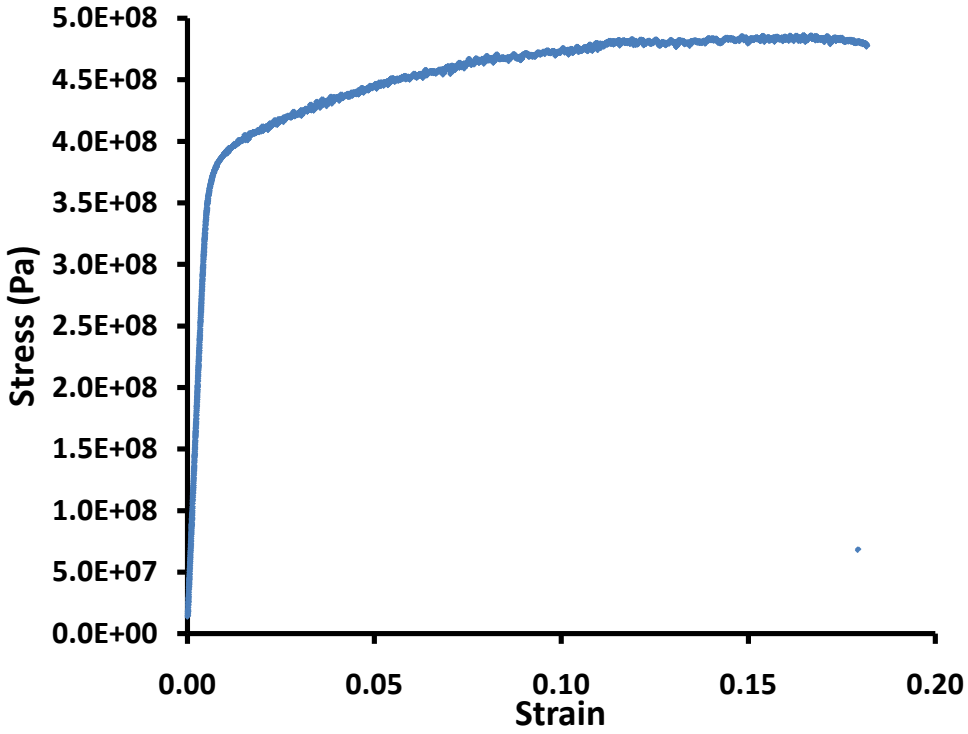

Figure 2.12 Stress-strain curve for simple tension test

The purpose of the parametric study is to determine values of the material parameters used in crystal plasticity. The procedure allows the material to exhibit anisotropic behavior at the microscale due to crystalline orientations, and maintain the overall material behavior at larger scales in accordance with the isotropic macroscale material behavior from the experimental tests. This parametric study for evaluating the three material parameters associated with Asaro's hardening rule (Eqn. (2.23)) in single crystal plasticity ensures that overall stress-strain response from a RVE containing a sufficient number of grains matches the test data.

$$h(\gamma) = h_0 \sec h^2 \left| \frac{h_0 \gamma}{\tau_s - \tau_0} \right| \qquad (2.23)$$

where h_0 is initial hardening modulus, τ_s is stage I stress and τ_0 is initial strength. h_0 controls the slope of stress-strain curves at the plastic region and τ_0 controls the yield point. A total of 15 analyses have been conducted for the parametric study to determine the three parameters as: h_0=5MPa, τ_s=375MPa, and τ_0=146MPa. Figure 2.13 shows an RVE that contains 167 grains and Figure 2.14 shows four simulation curves where h_0 and τ_s are fixed and only τ_0 is varied.

Figure 2.13 RVE containing 167 grains for parametric study

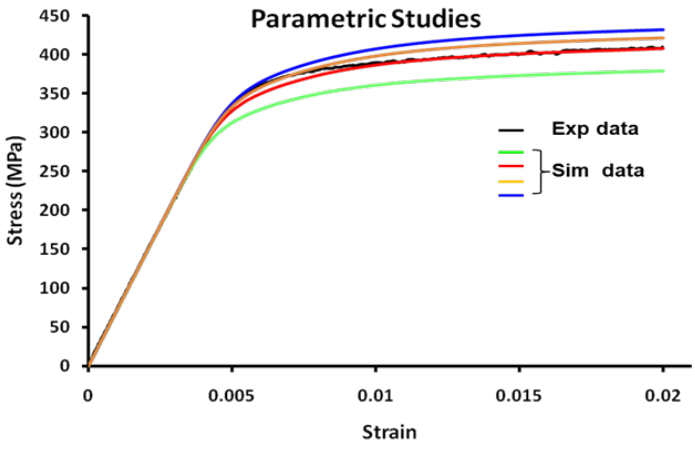

Figure 2.14 Parametric study reevaluating parameters used in Asaro's hardening rule

In cyclic loading, an essential factor is kinematic hardening. In order to determine the material parameters (b & r) used in the Armstrong- Frederick hardening type (Eqn. 2.12), a cyclic loading test and parametric study were conducted. Figure 2.15 shows the stress-strain curve under cyclic loading.

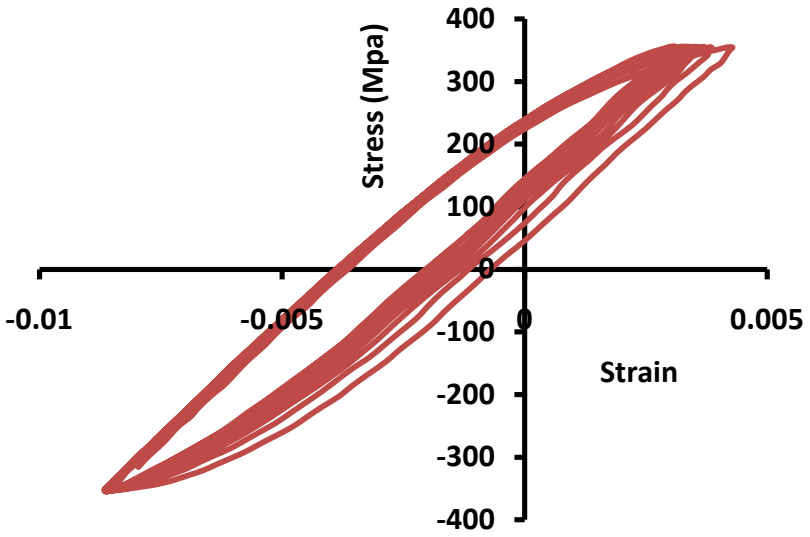

Figure 2.15 Stress-strain curve for cyclic loading test

When the compression response is compared with the tension response (shown in Fig. 2.16), it is clear that initial backstresses are present due to the manufacturing rolling process.

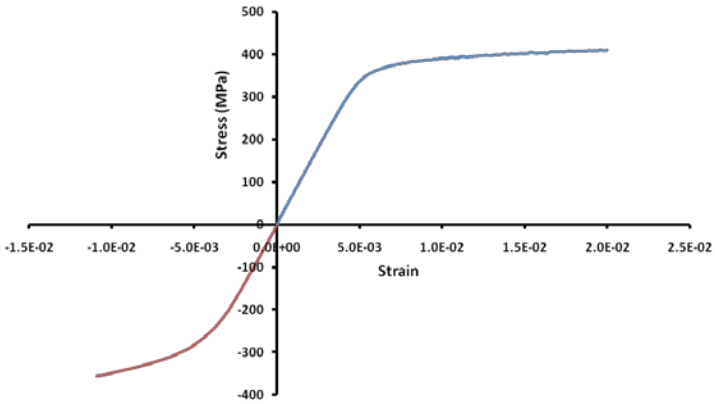

Figure 2.16 Comparison between compression and tension

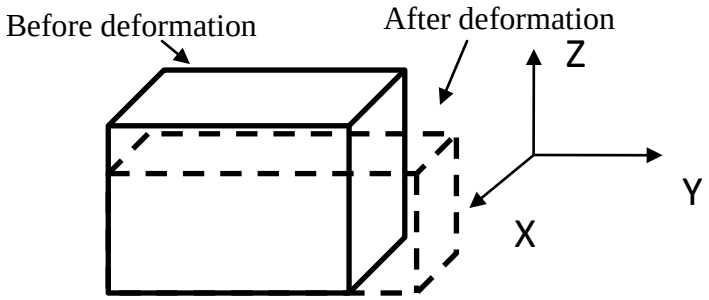

Figure 2.17 Deformation of the sample

In order to simplify the problem, an assumption is made that the deformation along X direction shown in Fig. 2.17 can be neglected. The Y direction is along the rolling direction and the X-Y plane is parallel to the surface of the sample. Using an incompressive assumption:

$$\dot{\varepsilon}_{xx} + \dot{\varepsilon}_{yy} + \dot{\varepsilon}_{zz} = 0 \tag{2.24}$$

By applying the zero deformation along X direction, it gives:

$$\dot{\varepsilon}_{yy} \approx -\dot{\varepsilon}_{zz} \tag{2.25}$$

The backstress components, thus, can be derived as:

$$\begin{cases} \chi_X \approx 0.0 \\ \chi_Z \approx -\chi_Y \end{cases} \tag{2.26}$$

For crystal plasticity, the backstress needs to be resolved along different slip systems through Eqn. 2.27:

$$\chi^{(\alpha)} = \boldsymbol{\chi} \cdot \boldsymbol{\mu} \tag{2.27}$$

where $\boldsymbol{\chi}$ and $\boldsymbol{\mu}$ are the backstress tensor and Schmid factor tensor in the Cartesian coordinate system. The initial backstress component is also calculated from Fig. 2.16.

$$\begin{cases} \sigma_{Tension} = 375MPa \\ \sigma_{Compression} = -312MPa \\ \chi_Y = \dfrac{\sigma_{Tension} + \sigma_{Compression}}{2} = 31.5MPa \end{cases} \tag{2.28}$$

The simulation results from the parametric study are compared to the experimental data in order to determine the material parameters, as shown in Fig. 2.18. From the parametric study, one conclusion can be obtained that the influence of initial backstress on the cyclic loading stress-strain response is much higher than the material parameters *b* and *r* in Eqn 2.12. Therefore, the values of material parameters *b*=350 and *r*=1 are chosen for Al 2024.

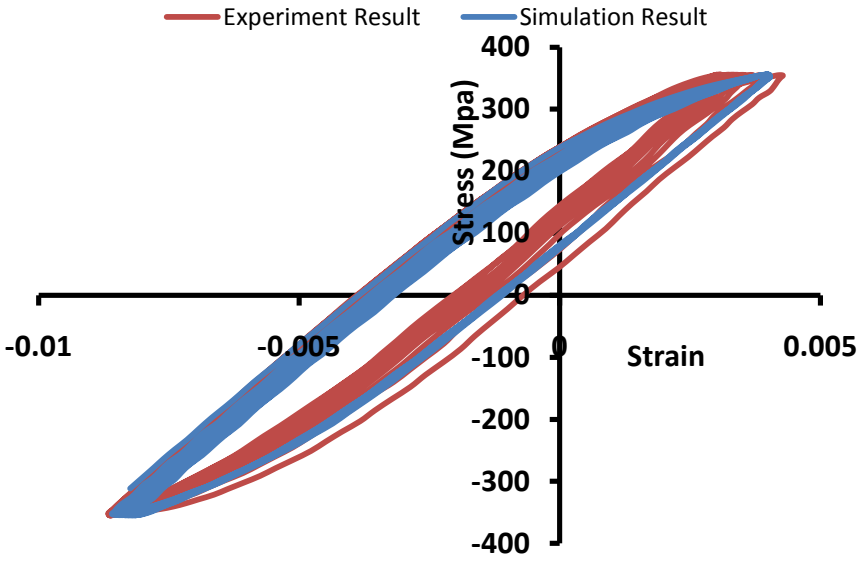

Figure 2.18 Parametric study for cyclic loading

2.7 Concluding Remarks

Single crystal plasticity was used to account for the orientation and size effect of each grain at the micro level. The results show that the model can capture local anisotropic material behavior at grain level. In order to make the global stress-

strain curve match the experimental results, a parametric study was conducted and fitted to the experimental data under simple tension loading conditions. A parametric study for cyclic loading conditions was also conducted to determine the key material parameters used in the Armstrong- Frederick hardening rule. Initial backstress due to manufacturing process is determined through experiments.

Chapter 3

Size-Dependent Void Model

3.1 Introduction

Failure of engineering structures as a result of fracture can lead to catastrophic outcomes. Fracture is caused by damage due to microvoid nucleation, growth, and coalescence in ductile materials. The physical characteristics of structures, such as fracture toughness and stress intensity factor can be easily measured via experiments; however other factors, such as incipient damage and damage evolution, are often more difficult to assess. Therefore, physically-based theoretical modeling is necessary to complement the experimental research in damage diagnosis and prognosis. Currently, significant research efforts are underway in developing experimental and theoretical methods for damage monitoring, design of early warning systems, and evaluation of the remaining life of engineering structures for the prevention and/or prediction of failure. Health and condition monitoring techniques, for instance, involve damage detection and quantification that can be used to take preventive measures before failure occurs [42, 43].

The field of damage mechanics, historically, has offered many theories, some rooted in a phenomenological framework and others based on the concept of microvoid growth. Over the last three decades, numerous theoretical models have emerged that study dominant failure mechanisms in ductile materials. Rice and Tracey [44] investigated the growth of a single void in an infinite matrix and established that the void growth rate increases exponentially with the hydrostatic

stress, $\sigma_{kk,}$ imposed on the solid. Gurson [45] adopted a unit-cell model of a single void in a finite matrix, where the volume ratio of the void to the unit cell gives the void volume fraction *f*. In this work, Gurson established a yield criterion that depends not only on the von Mises effective stress (as in classical plasticity), but also on the hydrostatic stress and void volume fraction *f*. Tvergaard [46] modified the Gurson model to obtain a better agreement with the finite element analyses of void growth, as well as to account for the effect of plastic work hardening.

However, the void models developed by Tvergaard and Gurson lacked two important factors impacting material damage, namely the effect of size and of crystal orientation. Numerous microscale experiments have shown that materials exhibit strong size effect when the characteristic length is down to microscale [45-57]. Although there have been some attempts to include the size effect in the damage mechanics theory, they are still based on a phenomenological strain gradient plasticity theory. Recent experimental investigations [58, 59] and numerical studies on microvoids [60-66] have shown that void growth in ductile materials depends heavily on void size. Micron- and submicron-sized voids tend to grow slower than larger voids under the same stress level. Without intrinsic material lengths, the classical plasticity theories cannot account for the void size effect. Liu *et al*. [66] investigated the void size effect on the void growth rate based on the Taylor dislocation model [27, 28], which involves an intrinsic material length. For large voids, the void growth rate agrees well with the Rice-Tracey model [44] and displays no size effect. However, for small voids, the void growth rate scales with the square of hydrostatic stress, $(\sigma_{kk}/\sigma_y)^2$, rather than the

exponential dependence in the Rice-Tracey model. Here σ_y is the tensile yield stress, and σ_{kk} is the first stress invariant. Wen *et al*. [67, 68] used a similar approach to extend the Gurson model to solids with cylindrical microvoids and spherical microvoids. These models show size-dependency, but the crystal orientation effect has still not been considered.

A few experiments have also shown that similar materials with different crystal orientation, exhibit different behaviors, such as fracture toughness [69, 70]. There are many void models for damage: some consider the void shape effect, while others consider the void size effect. But there exists no void model to date that takes into consideration the orientation effect. In order to incorporate the size and crystal orientation effects to the damage mechanics theory, a new mechanism-based damage mechanics theory has been developed and is presented in this chapter.

A constitutive law that accounts for crystal orientation and microvoid size effects is derived. Microvoid growth is determined by specific crystal orientation, as well as microvoid and grain size. The approach adopted here stands in direct contrast to the phenomenological methods employed in existing theories. This new theory is derived by means of the Taylor dislocation model and the recently developed strain gradient crystal plasticity. Given these specific characteristics, the new mechanics-based damage mechanics theory is different from existing theories. The results of the theory clearly show an axisymmetric loading leading to unsymmetric deformation due to crystal orientation. This deformation pattern, however, cannot be explained by existing damage mechanics theories since they

do not incorporate crystal orientation information. Simulation studies based on a single crystal plasticity theory are also conducted through finite element analysis (FEA) to investigate void area fraction effect, crack length effect, and representative volume element (RVE) size effect.

3.2 Taylor Dislocation Model

The Taylor dislocation model [27, 28, 71] gives the shear flow stress τ in terms of the dislocation density by

$$\boldsymbol{\tau = \alpha \mu b \sqrt{\rho} = \alpha \mu b \sqrt{\rho_s + \rho_G}} \qquad (3.1)$$

where μ is the shear modulus; b is the Burgers vector; and α is an empirical material constant (value around 0.3) [27, 28, 72]. The dislocation density ρ consists of two parts, namely the density of statistically stored dislocations ρ_s and the density of geometrically necessary dislocations ρ_G, where the former is determined from the relation between stress σ and plastic strain ε in uniaxial tension, $\alpha \mu b \sqrt{\rho_s} = \sigma_{ref} f(\varepsilon)/M$, and the latter is related to the gradient of plastic deformation by $\rho_G = \bar{r}\eta/b$ [73-75]. Here σ_{ref} is a reference stress (e.g., yield stress σ_Y); M is the Taylor coefficient; $M = \sqrt{3}$ for an isotropic solid and $M = 3.06$ for a face-centered-cubic (FCC) crystal [76-78]; $\bar{r}$ is the Nye factor to account for the effect of discrete slip systems on the distribution of geometrically necessary dislocations, and it is chosen to be 1.9 for FCC crystals [79]; and $\eta = 1/2\sqrt{\eta_{ijk}\eta_{ijk}}$ is the effective strain gradient and $\eta_{ijk} = u_{k,ij}$ is the strain gradient tensor.

The Taylor dislocation model, which has been used to develop strain gradient plasticity theory [73-75], is successfully explained in many micro-scale experiments and phenomena [57, 80-82]. In the foregoing strain gradient theories, the constitutive law does not depend on crystal orientation.

Han et al. [83, 84] recently developed a mechanism-based strain gradient crystal plasticity (MSG) theory and related ρ_S^α to the slip resistance function g^α for α-th slip system by $\rho_S^\alpha = (\frac{g^\alpha}{\alpha\mu b})^2$ and ρ_G^α to the effective density of geometrically necessary dislocations η_G^α by$\rho_G^\alpha = \eta_G^\alpha/b$. The effective density of geometrically necessary dislocations η_G^α is given by

$$\boldsymbol{\eta_G^\alpha} = \left\| \boldsymbol{m^\alpha} \times \sum_{\boldsymbol{\beta}} (\boldsymbol{s^{\alpha\beta}} \boldsymbol{\nabla \gamma^\beta} \times \boldsymbol{m^\beta}) \right\| \tag{3.2}$$

where $\| \ \|$ denotes the norm, γ^α is the plastic shear, $\boldsymbol{s}$ and $\boldsymbol{m}$ are the slip direction and slip plane normal, respectively, $|\boldsymbol{s^\alpha}| = |\boldsymbol{m^\alpha}| = 1$ and $\boldsymbol{s^\alpha \cdot m^\alpha} = 0$, $\boldsymbol{s^{\alpha\beta} = s^\alpha \cdot s^\beta}$, and the plastic shear γ^α is related to the macroscopic strain via Eqn. (3.3).

$$\boldsymbol{\varepsilon} = \sum_{\boldsymbol{\alpha}} \gamma^{\boldsymbol{\alpha}} (\boldsymbol{s^\alpha} \otimes \boldsymbol{m^\alpha})_{\boldsymbol{sym}} \tag{3.3}$$

Adding the density of statistically stored dislocations ρ_s and the density of geometrically necessary dislocations ρ_G in Eqn. (3.1) leads to shear stress:

$$\boldsymbol{\tau^\alpha} = \boldsymbol{g_0} \sqrt{(\boldsymbol{g^\alpha}/\boldsymbol{g_0})^2 + \boldsymbol{l\eta_G^\alpha}} \tag{3.4}$$

where $\boldsymbol{g_0}$ denotes a reference slip resistance and $\boldsymbol{l}$ is an intrinsic length scale associated with strain gradient as

$$\boldsymbol{l} = \frac{\boldsymbol{\alpha^2 \mu^2 b}}{\boldsymbol{g_0^2}} \tag{3.5}$$

Typically, $\boldsymbol{b}$ is around one tenth of a nanometer and $\boldsymbol{\mu/g_0} \approx 100$, and the intrinsic length scale $\boldsymbol{l}$ is estimated to be on the order of a micron, similar to the MSG theory [73, 74, 80, 85]. Thus the flow stress can be expressed as

$$\boldsymbol{\sigma_{flow} = M\tau = M g_0 \sqrt{\sum_{\alpha} (g^{\alpha}/g_0)^2 + l \sum_{\alpha} \eta_G^{\alpha}}} \tag{3.6}$$

The Taylor dislocation model will also be used in the development of the proposed mechanism-based damage mechanics. However, unlike the MSG theory developed by Gao et al. [73] and Huang et al. [74], this new theory will determine the effective strain gradient with respect to specific crystal orientations and the damage mechanism of microvoid growth.

3.3 Damage Model Accounting for Size and Orientation Effects

Nucleation, growth, and coalescence of microvoids are common damage mechanisms for ductile materials. The developed theory uses the microvoid growth rate as the damage index. Unlike existing damage mechanics theories [45] that do not account for the effect of orientation on microvoid growth rate, the damage index is directly determined from strain gradient crystal plasticity [83, 84] and specific crystal orientation in current work. A general procedure is introduced in this section and some results, based on a specific example, are presented.

For a microvoid in an infinite medium and subject to the remote strain field, $\varepsilon_{ij}^{\infty}$, the strain field in the solid depends on the remote strain field and the

geometry of the microvoid (e.g., the microvoid growth rate *D* and size and shape of the microvoid). Therefore orientation imaging microscope (OIM) is used to identify the crystal texture and the activated slip systems ($\boldsymbol{s}^{\alpha}$ and $\boldsymbol{m}^{\alpha}$) for the solid. According to Eqn. (3.3), the plastic shear γ^{α} can be calculated in terms of the remote strain fields and the microvoid growth rate *D* for each activated slip system obtained from OIM. Thus both the slip resistance $\boldsymbol{g}^{\boldsymbol{\alpha}}$ and the effective strain gradient $\boldsymbol{\eta}^{\boldsymbol{\alpha}}$ can be determined depending on the crystal orientation and microvoid growth rate *D*. Then the flow stress $\boldsymbol{\sigma}_{\boldsymbol{flow}}$ is given by Eqn. (3.6). Once again, the flow stress depends on the microvoid growth rate *D*, i.e.,

$$\boldsymbol{\sigma}_{\boldsymbol{flow}} = \boldsymbol{M\tau} = \boldsymbol{Mg_0}\sqrt{(\boldsymbol{g}^{\boldsymbol{Total}}(\boldsymbol{D})/\boldsymbol{g_0})^2 + \boldsymbol{l}\sum_{\boldsymbol{\alpha}}\boldsymbol{\eta}_{\boldsymbol{G}}^{\boldsymbol{\alpha}}(\boldsymbol{D})} \quad (3.7)$$

A power-law viscoplastic-limit model is adopted to link the plastic strain rate $\dot{\varepsilon}^{p}$ and the flow stress $\boldsymbol{\sigma}_{\boldsymbol{flow}}$ (Eqn. 3.7) by

$$\dot{\boldsymbol{\varepsilon}}^{\boldsymbol{p}} = \dot{\boldsymbol{\varepsilon}}\left(\frac{\boldsymbol{\sigma_e}}{\boldsymbol{\sigma}_{\boldsymbol{flow}}}\right)^{\boldsymbol{n}} \quad (3.8)$$

where $\dot{\varepsilon} = \sqrt{\frac{2}{3}\dot{\varepsilon}'_{ij}\dot{\varepsilon}'_{ij}}$, and $\dot{\varepsilon}'_{ij} = \dot{\varepsilon}_{ij} - \frac{1}{3}\dot{\varepsilon}_{kk}\delta_{ij}$ is the deviatoric strain rate; $\sigma_e = \sqrt{\frac{3}{2}\sigma'_{ij}\sigma'_{ij}}$ is the von Misses effective stress; *n* is a rate-sensitivity exponent, which usually takes a large value (≥ 20). Finally, a mechanism-based damage mechanics theory is developed based on the flow stress that depends on crystal orientation and microvoid growth rate *D*. The constitutive law is in the framework of J_2 flow theory and is given by substituting Eqn. 3.7 into Eqn. 3.8 and substituting Eqn. 3.8 into J_2 flow theory constitutive relation:

$$\dot{\boldsymbol{\sigma}}_{\boldsymbol{ij}} = \boldsymbol{K}\dot{\boldsymbol{\varepsilon}}_{\boldsymbol{kk}}\boldsymbol{\delta}_{\boldsymbol{ij}} + \boldsymbol{2\mu}\left\{\dot{\boldsymbol{\varepsilon}}'_{\boldsymbol{ij}} - \frac{\boldsymbol{3}\dot{\boldsymbol{\varepsilon}}}{\boldsymbol{2\sigma_e}}\left[\frac{\boldsymbol{\sigma_e}}{\boldsymbol{M g_0}\sqrt{(\boldsymbol{g^{Total}(D)/g_0})^2 + \boldsymbol{l}\sum_{\alpha}\boldsymbol{\eta}_{\boldsymbol{G}}^{\boldsymbol{\alpha}}(\boldsymbol{D})}}\right]^{\boldsymbol{n}}\boldsymbol{\sigma}'_{\boldsymbol{ij}}\right\} \tag{3.9}$$

This mechanism-based damage mechanics theory incorporates the crystal texture, activated slip systems, microvoid growth rate, and the size effect into the constitutive law. Although further simulation and experimental verification need to be conducted, this damage mechanism theory paves the way to study the damage of ductile materials from the fundamental mechanisms.

3.3.1 Continuum Model with Cylindrical Microvoid

Some results on the development of the constitutive law based on the growth of cylindrical microvoids are presented in this section. In the results, a microvoid is assumed to have been nucleated. For a cylindrical microvoid of initial radius r_0 in an infinite medium and subject to remote equi-biaxial tension, $\varepsilon_{11}^{\infty} = \varepsilon_{22}^{\infty} = \varepsilon^{\infty}$. Under the assumption of proportional deformation and ignoring the elastic deformation (i.e., the solid is incompressible), the non-vanishing displacement field is $u_r = \frac{r_0}{r}u_0 = \varepsilon D r_0^2/r$, where (r, θ, z) are the cylindrical coordinates, u_0 is the displacement on the microvoid surface, $\varepsilon = \sqrt{2\varepsilon_{ij}^{\infty}\varepsilon_{ij}^{\infty}/3} = 2\varepsilon^{\infty}/\sqrt{3}$ is the effective strain in the remote field, and $D = \frac{u_0}{\varepsilon r_0} = \dot{V}/2\dot{\varepsilon}V$ is the void growth rate under proportional deformation. The non-vanishing strains (also the plastic strain) are given by

$$\boldsymbol{\varepsilon_{rr} = -\varepsilon_{\theta\theta} = -\varepsilon D \frac{r_0^2}{r^2}} \tag{3.10}$$

In this analysis, two activated slip systems $\boldsymbol{s^1 = e_r(\omega), m^1 = e_\theta(\omega), s^2 = e_r\left(\omega + \frac{2\pi}{3}\right), m^2 = e_\theta\left(\omega + \frac{2\pi}{3}\right)}$, are considered, where $\boldsymbol{\omega}$ is the polar angle, i.e., the orientation of the first slip system as shown in Fig. 3.1. According to Eqn. (3.3), the plastic shear γ^α for each slip system can be determined and the effective strain gradient $\boldsymbol{\eta_G^\alpha}$ on a slip system $\boldsymbol{\alpha}$ can then be obtained from Eqn. (3.2),

$$\begin{aligned} \boldsymbol{\eta_G^1} &= \boldsymbol{\frac{4}{\sqrt{3}} \varepsilon^\infty D \frac{r_0^2}{r^3} \left|\sin\left(3\theta - 3\omega + \frac{\pi}{3}\right)\right|} \\ \boldsymbol{\eta_G^2} &= \boldsymbol{\frac{4}{\sqrt{3}} \varepsilon^\infty D \frac{r_0^2}{r^3} \left|\sin(3\theta - 3\omega - \frac{\pi}{3})\right|} \end{aligned} \tag{3.11}$$

where $\boldsymbol{\theta}$ is a polar angle of a material point in the solid. The uniqueness of this approach is the fact that in addition to depending on $\boldsymbol{\omega}$ (orientation of a slip system), the effective strain gradient also varies with polar angle $\boldsymbol{\theta}$, which is different from the mechanism-based strain gradient plasticity theory [74], where the effective strain gradient does not depend on polar angle for cylindrical microvoid growth. This is because in the developed theory the equi-biaxial tension in the remote field may not lead to symmetric dislocation slip systems for arbitrary crystal texture, and thus the symmetric loading may not produce symmetric deformation, while the mechanism-based strain gradient plasticity theory smears out the information for crystal orientation via homogenization. A similar unsymmetrical deformation mode due to symmetric loading was also observed in Nemat-Nasser, et al. [86] and numerically verified by Solanki, et al. [70].

By using linear strain hardening in slip resistance, $g^{\alpha} = g_0 + 4r_0^2 c_h \varepsilon^{\infty} D/r^2[\left|\cos 2\left(\theta - \omega - \frac{2\pi}{3}\right)\right| + |\cos 2(\theta - \omega)|]$, the flow stress is then obtained by Eqn. (3.7), where the effective strain gradient is given in Eqn. (3.11). It is obvious that the flow stress depends on microvoid growth rate *D*, the orientation of the slip system via $\boldsymbol{\omega}$, and the intrinsic length scale $\boldsymbol{l}$. Among these factors, the size effect has been well addressed [74, 87-89].

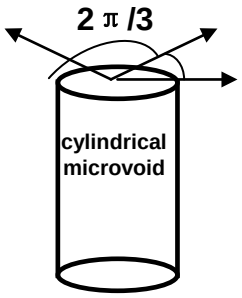

Figure 3.1 Cylindrical microvoid with two slip systems

In order to address the influence of microvoid growth rate *D* and the orientation of slip system on the flow stress, the Taylor coefficient $M = 3.06$ is chosen for FCC crystal,$c_h/g_0 = 0.2$ [84], $\theta = 2\pi/3$, $\varepsilon^{\infty} = 0.1$, $r_0/r = 0.5$, $l/r_0 = 1$. The flow stress is calculated for several values of *D* and $\boldsymbol{\omega}$. It should be pointed out that a value for the microvoid growth rate *D* is arbitrarily given in the simulation, though it depends on remote field and microvoid size. Figure 3.2 shows the flow stress σ_{flow}/g_0 with respect to various values of microvoid growth rate *D* for given $\omega = \pi/4$ and $\omega = \pi/3$, and Fig. 3.3 gives the flow stress for various values of slip system orientation for *D* = 20 and 30. It is obvious that both microvoid growth rate, *D*, and slip system orientation, $\boldsymbol{\omega}$, have very strong

effects on the flow stress. Therefore, it is critical to include the crystal orientation information in the constitutive law and the proposed mechanism-based damage mechanics can capture this crystal orientation dependence. This important orientation dependence cannot be studied within the existing framework of damage mechanics.

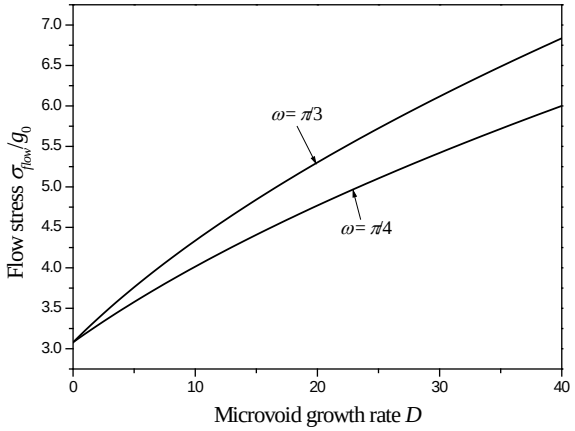

Figure 3.2 Dimensionless flow stress vs microvoid growth rate D

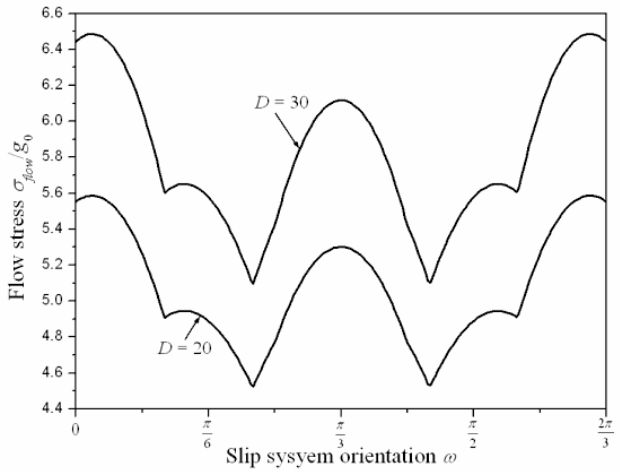

Figure 3.3 Dimensionless flow stress vs slip system orientation

3.3.2 Continuum Model with Spherical Microvoid

For a spherical void in an infinite medium subjected to remote spherical symmetric tension, ε^{∞}. Assume the material is incompressible. The displacement in the radial direction is:$u_R = \frac{R_0^2}{R^2}u_0$, where u_0 is the displacement on the void surface, R_0 and R are the void radius and radial coordinate, respectively. The non-vanishing strain in the spherical coordinates (R,θ,ϕ) and the strain are:$\varepsilon_{RR} = -2\varepsilon_{\theta\theta} = -2\varepsilon_{\phi\phi} = -2\frac{R_0^2}{R^3}u_0$, $\varepsilon = \frac{2R_0^2}{R^3}u_0 = \varepsilon^{\infty}$. The void growth rate under proportional deformation is also defined as:$D = \frac{u_0}{\varepsilon R_0} = \frac{\dot{V}}{3\dot{\varepsilon}V}$. So the non-vanishing strain in terms of the effective strain and void growth rate can be obtained as follows: $\varepsilon_{RR} = -2\varepsilon_{\theta\theta} = -2\varepsilon_{\phi\phi} = -2\varepsilon D\frac{R_0^3}{R^3}$. Three activated slip systems are considered (Fig. 3.4): $\{\tilde{\boldsymbol{s}}^{\boldsymbol{1}} = [\boldsymbol{\cos\omega, \sin\omega, 0}]^{\boldsymbol{T}}, \tilde{\boldsymbol{m}}^{\boldsymbol{1}} = [\boldsymbol{-\sin\omega, \cos\omega, 0}]^{\boldsymbol{T}}\}$, $\{\tilde{\boldsymbol{s}}^{\boldsymbol{2}} = [\boldsymbol{-\cos\omega, \sin\omega, 0}]^{\boldsymbol{T}}, \tilde{\boldsymbol{m}}^{\boldsymbol{2}} = [\boldsymbol{-\sin\omega, -\cos\omega, 0}]^{\boldsymbol{T}}\}$,
$\{\tilde{\boldsymbol{s}}^{\boldsymbol{3}} = [\boldsymbol{0, 0, 1}]^{\boldsymbol{T}}, \tilde{\boldsymbol{m}}^{\boldsymbol{3}} = [\boldsymbol{\cos\varphi, \sin\varphi, 0}]^{\boldsymbol{T}}\}$.

By using coordinate transformation and Eqn. (3.3), the resolved shear in each slip system is calculated as follows:

$$\begin{cases} \gamma^1 = \varepsilon D\frac{R_0^3}{R^3}\left(\frac{B}{\cos 2\omega} - \frac{A}{\sin 2\omega}\right) \\ \gamma^2 = \varepsilon D\frac{R_0^3}{R^3}\left(\frac{B}{\cos 2\omega} + \frac{A}{\sin 2\omega}\right) \\ \gamma^3 = -3\varepsilon D\frac{R_0^3}{R^3}\frac{\sin 2\phi\cos\theta}{\cos\varphi} \end{cases} \tag{3.12}$$

where $\begin{cases} A = \sin^2\theta + \sin^2\phi\cos^2\theta - 2\cos^2\theta\cos^2\phi \\ B = -3\cos\theta\sin\theta\cos^2\phi \end{cases}$, θ and ϕ are angles of a material point in the solid in spherical coordinates, and φ is the angle between the

normal to the third slip plane and x_1 axis in the Cartesian coordinate system. The effective strain gradient on a slip system can then be obtained from Eqn. (3.2). By substituting the linear relation of slip resistance, the total resistance is given by

$$g^{Total} = g_0 + c_h(|\gamma^1| + |\gamma^2| + |\gamma^3|) = g_0 + c_h \varepsilon D \frac{R_0^3}{R^3}\left[\left|\frac{B}{\cos 2\omega} - \frac{A}{\sin 2\omega}\right| + \left|\frac{B}{\cos 2\omega} + \frac{A}{\sin 2\omega}\right| + 3\left|\frac{\sin 2\phi \cos\theta}{\cos\varphi}\right|\right] \quad (3.13)$$

Using Eqn. (3.7), the flow stress accounting for size effect and orientation effect is obtained.

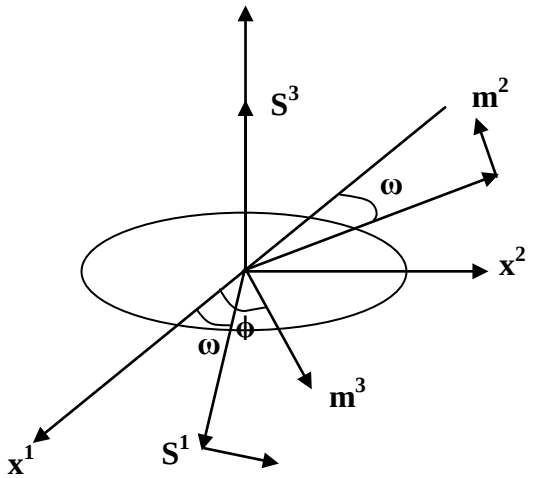

Figure 3.4 Three activated slip systems

For illustrating the size effect and orientation effect, $M = 3.06$, $c_h/g_0 = 0.2$, $\varepsilon^{\infty} = 0.1$, $r_0/r = 0.5$, and $l/r_0 = 1$ are chosen.

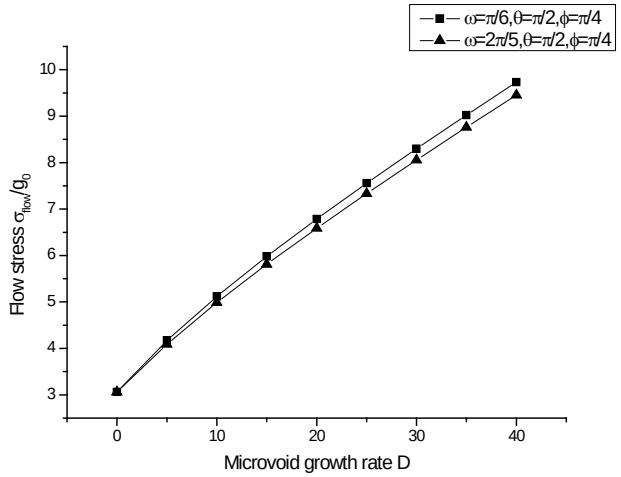

Figure 3.5 The flow stress vs microvoid growth rate D

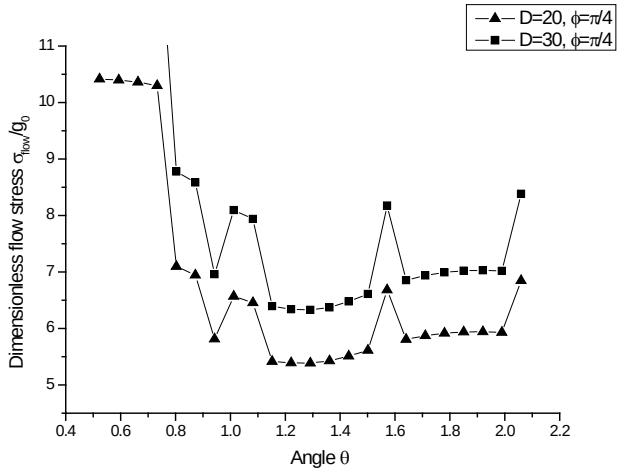

Figure 3.6 The flow stress vs spherical coordinate θ

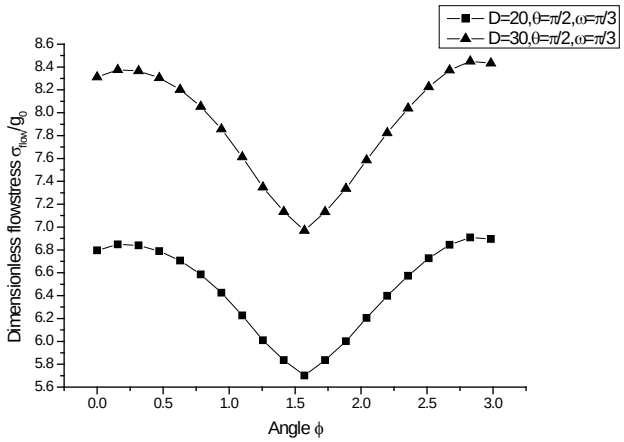

Figure 3.7 The flow stress vs spherical coordinate ϕ

Figure 3.5, 3.6, and 3.7 show that the flow stress depends strongly on microvoid size and orientation, a conclusion that can also be made from the cylindrical void analysis. Thus, the developed constitutive law is critical to the study of size and orientation effects in damage mechanics.

3.4 Simulation Studies

In the simulation studies, the effect of micro voids/micro cracks and RVE size on material stiffness is investigated. The single crystal plasticity theory is used to describe the material behavior in these studies. Microvoids or cracks are artificially induced in a simple structure. As shown in Fig. 3.8, nine microvoids (circled) are induced in the structure. Static loading is applied along the right edge. The comparison of the stress-strain curves along the loading direction is presented in Fig. 3.9, where the blue curve represents the undamaged structure and the purple curve represents the structure with the cracks (shown in Fig. 3.8).

The slopes of the elastic component in the two stress-strain curves shown in Fig. 3.9 are calculated where the stiffness drops by about 0.87% compared to the undamaged structure. Note that this reduction, although very small, represents a condition where the area ratio between micro cracks and the structure is only 0.2%. This can imply that the crack may cause a significant reduction in material stiffness as the area ratio increases. In addition, a small reduction in stress of 0.97% is observed in the structure with the cracks when the total strain reaches a value of 0.9%.

To further verify that the reduction is meaningful (and not caused by numerical noise), a second example is considered. A comparison is made of material behavior between an undamaged microstructure and the same microstructure with a single void inside. This time, the area fraction of the void is 1.59%. Figure 3.10 and 3.11 show the undamaged structure and the microstructure with a void, respectively. The comparison of the stress-strain response for the two microstructures is shown in Fig. 3.12. The stiffness decreases by 1.60% in the structure with the void compared to the undamaged structure. The maximum numerical error caused by the linear fitting is 0.28%, which means that the reduction cannot be caused by data fitting. The result also shows that in a microstructure with cracks, the defects as well as crystal orientations affect the stress distribution. This conclusion is also supported by comparing the differences of stress distributions shown in Fig. 3.10 and 3.11. The crystal orientations cause variations in the material behavior of each grain. Meanwhile, the micro crack causes stress concentrations at the crack tip (shown in the zoomed-in image in

Fig. 3.11). Such phenomena will help in understanding how cracks initiate at the microstructure and propagate through the length scales to the meso and macro levels.

The two examples presented here, however, are not comparable since they are based on different undamaged structures. In order to investigate the effect of micro voids distribution and to confirm that the existence of micro voids in the microstructure do cause material stiffness degradation, more simulations are conducted based on one structure. The results are shown in Table 3.1. Corresponding structures for simulation case 1 to case 5 in Table 3.1 are presented in Fig. 3.13. For case 2 and case 4, the shape and location of the single voids are approximately the same. The same condition is used for case 3 and case 5. Case 2 and case 3 used the same void area fraction. Similarly, case 4 and case 5 have been created under the same void area fraction. Two points can be concluded from the results shown in Table 3.1. First, it is clear that under the same area fraction, the single crack is more harmful than distributed micro voids due to more degradation on elastic stiffness. Second, the more void area fraction the structure has, the more is the elastic stiffness degradation.

Table 3.1 Comparison of elastic stiffness for different damaged structures

Simulation	Micro void type	Void area fraction	Elastic Stiffness (GPa)
Case 1	No void	0%	80.06
Case 2	Single void	0.901%	77.30
Case 3	Multiple voids	0.901%	77.50
Case 4	Single void	1.271%	76.24
Case 5	Multiple voids	1.271%	76.34

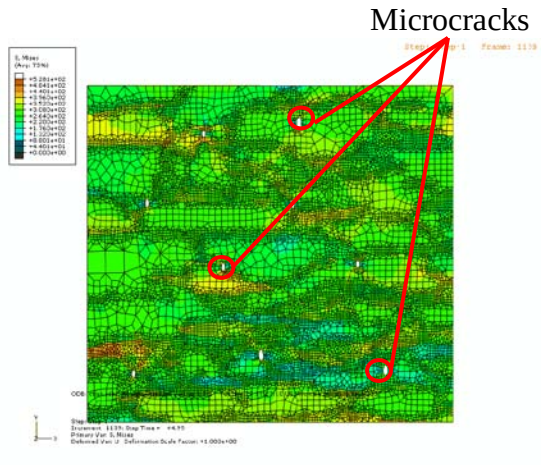

Figure 3.8 Mises stress distribution

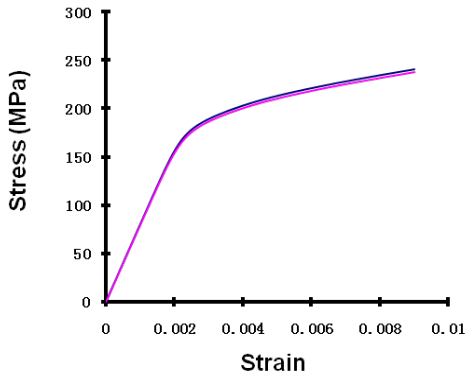

Figure 3.9 Comparison of stress-strain curve

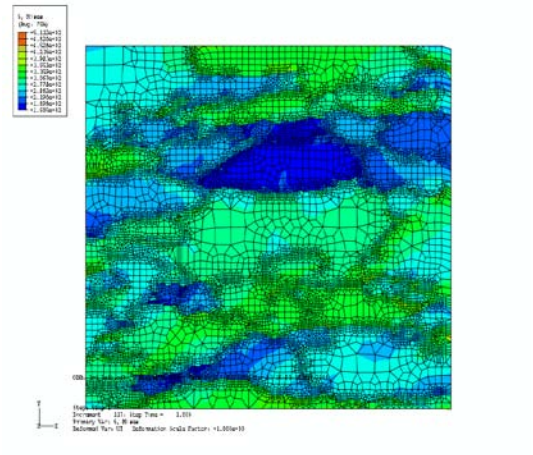

Figure 3.10 Undamaged structure

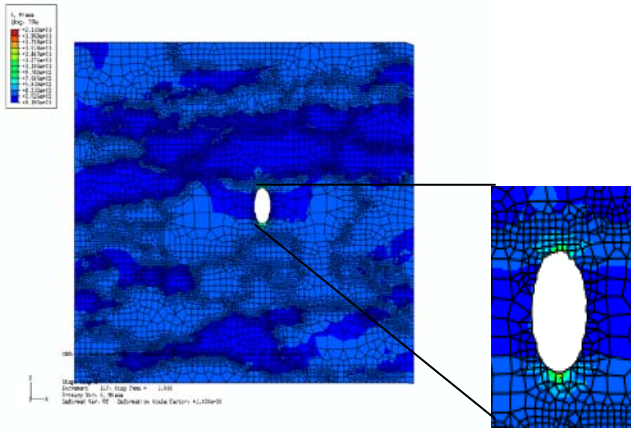

Figure 3.11 Structure with void

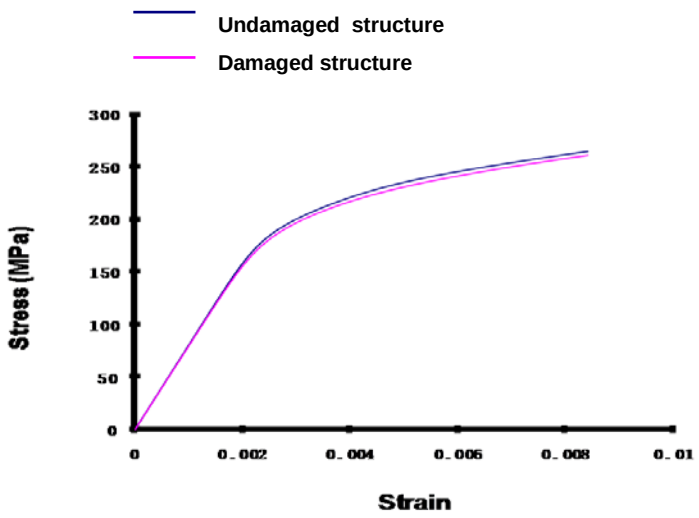

Figure 3.12 Comparison of stress-strain curve

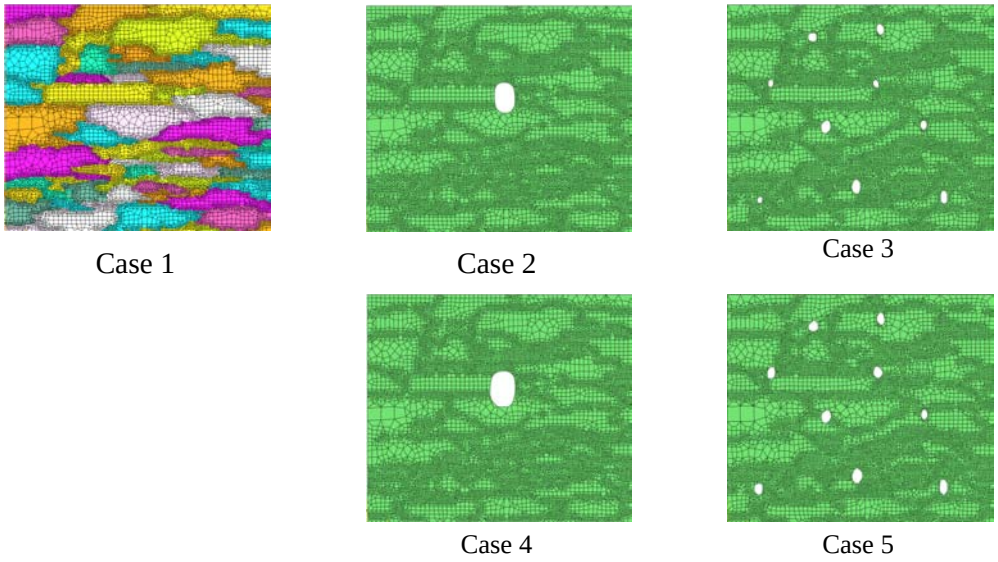

Figure 3.13 Healthy structure (Case1) and different damaged structures (Case2-5)

The effect of crack length on elastic stiffness is also investigated via numerical simulations. Cracks are induced at the same location of the structure with the same width but different length, as shown in Fig. 3.14. The elastic stiffness reductions for different crack lengths are listed in the Table 3.2.

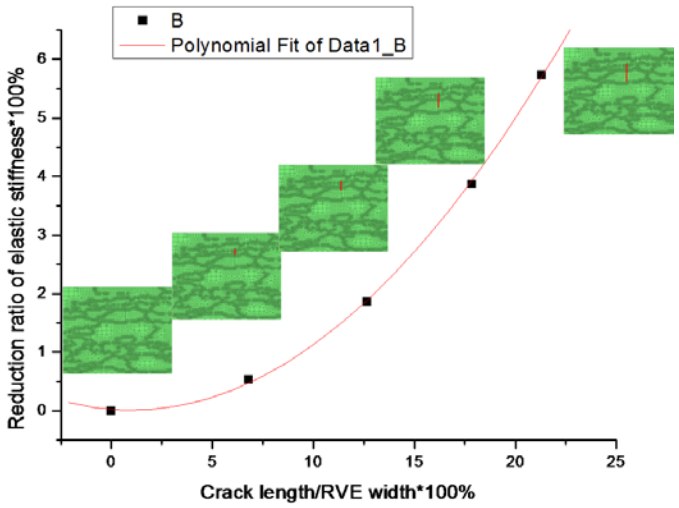

Figure 3.14 Crack length effect on material degradation

The elastic stiffness reduction rate accelerates incrementally with the crack length and it fits well into a quadratic curve as shown in Fig. 3.14.

Table 3.2 Elastic stiffness reduction for different crack lengths

No.	Dimensionless Reduction of Elastic Stiffness (%)	Normalized Crack Length (Crack Length/RVE Width*100 %)
1st	0.5302703753	6.801460042
2nd	1.859585398	12.66675878
3rd	3.869942982	17.85035079
4th	5.725240138	21.30345804

A convergence study on the RVE size was also conducted. Figure 3.15 shows that elastic stiffness changes with RVE size. All RVE sizes are normalized by the original RVE size, which is about 1194μm*951μm. As shown in Fig. 3.15, the elastic stiffness converges towards the original RVE elastic stiffness, which

means that the original RVE size adequately represents the general material behavior at macro scale.

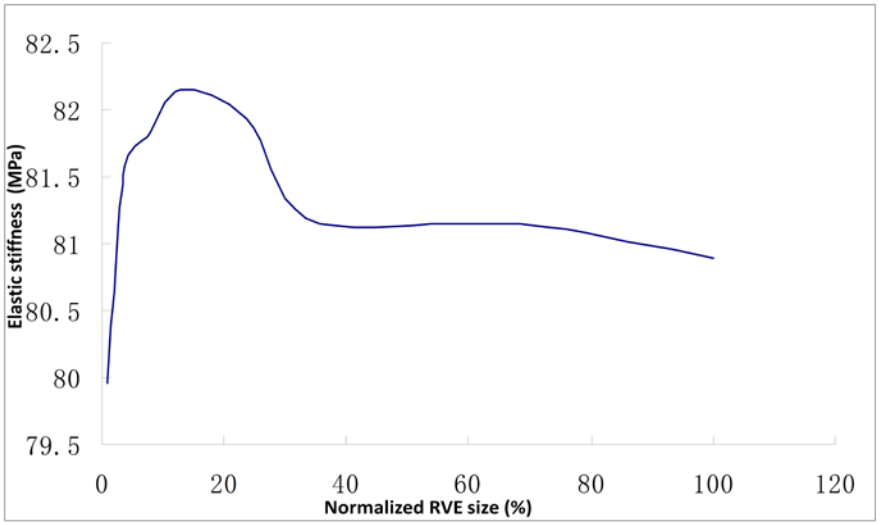

Figure 3.15 Elastic stiffness vs. RVE size

3.5 Summary

A size-dependent void model is developed considering crystal orientation effects. This void model is applied to different shapes of voids with certain activated slip systems. Strong dependence of flow stress on microvoid growth rate and slip system orientations is reflected in the simulation result. The effects of RVE size, defect area fraction and distribution on the material elastic stiffness are observed through simulation studies. A convergence study is used to determine the RVE size. Results from the crack length study shows that the crack propagation will accelerate material degradation in a quadratic manner. The results show that a single microvoid is more critical than distributed microvoids with the same area fraction.

Chapter 4

Single Crystal-Based Damage Model

4.1 Introduction

Better understanding of metal fatigue mechanisms have been achieved due to the development of digital image processing techniques. Fatigue damage models have progressively improved as a consequence [90-93]. Different stages of fatigue have been suggested based on an understanding of fatigue life. From experimental observations, for instance, fatigue cracks are known to usually start at the surface of a structural component. The cracks originate from shear cracks on crystallographic slip planes while gradually increasing approximately perpendicular to the external applied load. This two-stage fatigue life was first concluded by P.J.E. Forsyth [94]. Further investigation by Schijve [95] led to the division of fatigue phenomenon into four stages: crack nucleation, microcrack growth, macrocrack growth, and failure. Shang et al. [96] suggested similar divisions based on five stages: early cyclic formation and damage, microcrack nucleation, short crack propagation, macrocrack propagation, and final fracture. Miller [97, 98] introduced three types of cracks based on different mechanisms at different length scales. These are microstructurally small cracks, physically small cracks, and long cracks. Ritchie [99] proposed a slight change in classification of small cracks from Miller's definition and provided corresponding length scales for the different cracks: microstructurally small cracks of critical microstructural dimensions (grain size), physically small cracks (less than 1mm), mechanically small cracks (several mm) and chemically small cracks (10 mm).

In this chapter, a multiscale fatigue damage criterion, which is capable of predicting crack growth and propagation direction simultaneously, is presented. The first stage of fatigue life, which is dominated by shear crystallographic slip planes, is investigated using numerical simulation. In the damage model, relevant lengths are chosen based on the crack categories defined by Ritchie [99]. The characteristic crack length for critical damage is based on average grain size. The meso RVE is chosen as a 1 mm × 1 mm square according to the physically small crack size. The methodology for the fatigue damage estimation consists of two major parts. The stress-strain distribution is calculated based on the multiscale model. Then the multiscale fatigue damage criterion is used to estimate the failure of a meso RVE, as well as potential crack directions in the RVE based on the stress-strain distribution.

4.2 Constitutive Model

A single crystal plasticity theory offers several advantages over other techniques and is used in this research to describe the material behavior in the hotspot of an aluminum structure. The detailed introduction of single crystal plasticity is presented in chapter 2.

For the numerical simulation, a widely used commercial finite element software ABAQUS [41] is used, and a user-defined material subroutine (UMAT) that implements single crystal plasticity is developed based on Huang's work [39]. All the slip systems are treated as potentially active. Since negative $\dot{\gamma}^{(\alpha)}$ is allowed, slip system $(\mathbf{s}^{(\alpha)}, \mathbf{m}^{(\alpha)})$ and slip system $(-\mathbf{s}^{(\alpha)}, \mathbf{m}^{(\alpha)})$ are considered as

one slip system. The same rule is applied when calculating the damage parameters within each slip system. The results in chapter 2 and Refs. 100 indicate that the modified UMAT code is able to capture fatigue hardening and saturation. The most important feature of the model is that single crystal plasticity has the capability to capture local material anisotropic behavior due to different grain orientations.

4.3 Multiscale Damage Criterion

4.3.1 Damage Criterion for Crystalline Material

Jiang et al. [101-103] have shown that their fatigue damage criterion is capable of multiaxial and non-proportional loading. The advantages of this model consist not only the practicability in different loading conditions but also the capability of capturing changing loading directions [102]. However, in this model, accumulated fatigue damage is calculated along all directions in three-dimensional (3D) space. The critical material plane is determined by checking the plane in which the maximum accumulated fatigue damage reaches a critical value and the direction of crack propagation is along the critical material plane. Thus, it makes this method computationally expensive to implement in 3D. Furthermore, this model is applied at macroscale and cannot be directly used for damage prediction at microscale.

In this chapter, the Jiang's model is incorporated to single crystal plasticity based on the fact that fatigue cracks in metals tend to nucleate and propagate initially along slip planes. Accumulated fatigue damage is calculated only among

potential active slip systems rather than along all directions in 3D space. The corresponding criteria are rewritten as:

$$dD^{(\alpha)} = < \frac{\sigma_{mr}}{\sigma_0} - 1 >^m \left(1 + \frac{{\sigma_n}^{(\alpha)}}{\sigma_f}\right) dY^{(\alpha)} \tag{4.1}$$

$$dY^{(\alpha)} = \delta {\sigma_n}^{(\alpha)} (d\varepsilon^p)^{(\alpha)} + \frac{1-\delta}{2} {\sigma_s}^{(\alpha)} (d\gamma^p)^{(\alpha)} \tag{4.2}$$

where m and δ are material constants. It should be noted that the direction of the maximum material plane is a unit vector along the critical plane rather than a normal vector to the plane. This will be further clarified in the results section. In this chapter, all the simulations are focused on face centered cubic (FCC) crystal structures, such as copper and aluminum. A single FCC crystal has 12 slip systems, comprised of four slip planes, each with three slip directions. Preliminary results showing the damage parameter evolution of a single grain of aluminum inside the meso RVE for 12 potential active slip systems under uniaxial cyclic loading is presented here.

Cyclic loading is applied at the right edge of the mesoscale structure (shown in Fig. 4.1). Figure 4.2 shows the accumulative shear strain in each slip system in the element where the maximum damage is obtained. The fatigue damage evolution at different slip systems in the same element is presented in Fig. 4.3. The flat part of the curve indicates the unloading portion of a cycle. When these two figures are compared, a unique slip system (slip system 5) is prevalent with respect to the others, and this is considered as the dominant slip system. Slip system 5 is the maximum shear strain plane. It also has the highest damage value,

which agrees with the findings of Lemaitre [104]. Figure 4.2 and 4.3 indicate that the slip plane for maximum shear strain is the same for maximum damage parameters. However, this behavior is not exhibited by other slip planes due to the influence of normal stress on damage parameter. Table 4.1 lists the normal and slip direction of slip system 5. The Z coordinate of normal is very small compared to the X and Y coordinates. This means the slip plane lies almost in the X-Y plane. The X-Y plane projection of normal is shown in Fig. 4.4. It shows that the critical slip plane is approximately 45^{o} to the loading direction.

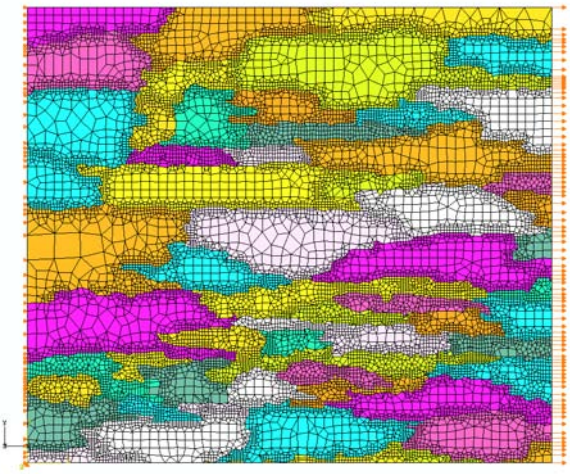

Figure 4.1 Finite Element model

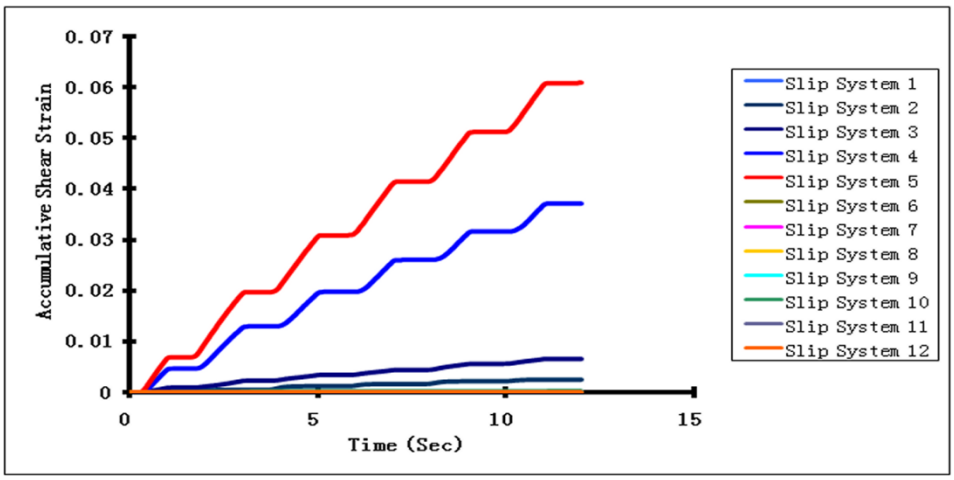

Figure 4.2 Accumulative shear strain in 12 slip systems

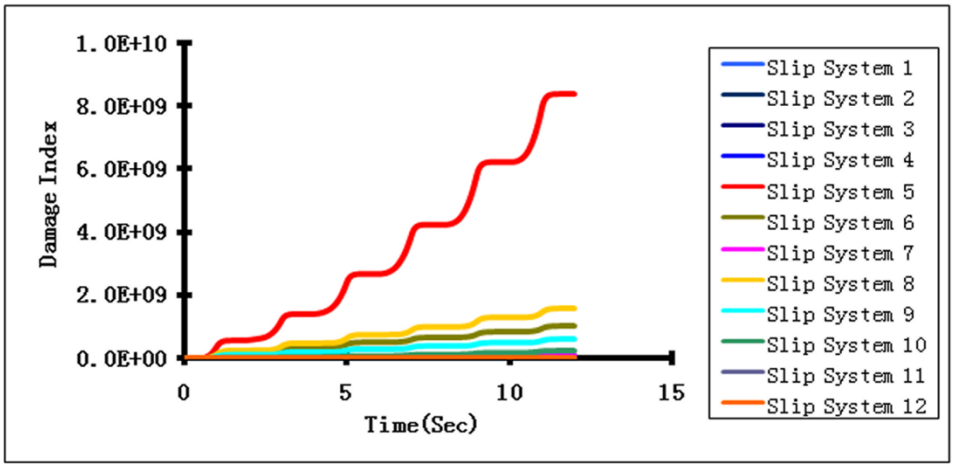

Figure 4.3 Fatigue damage evolution in 12 slip systems

Table 4.1 Normal and slip direction of the critical slip system

	Normal to the slip plane	Slip direction in the slip plane
X coordinate	-0.713215	-0.662362
Y coordinate	-0.693905	0.620869
Z coordinate	0.0991835	-0.41925

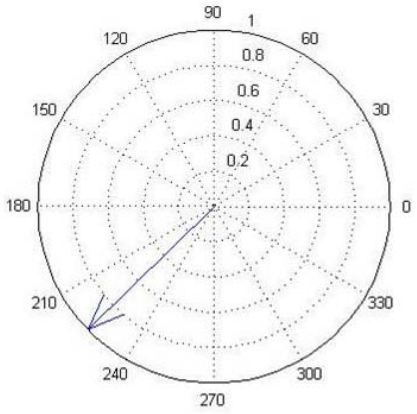

Figure 4.4 X-Y plane projection of the normal

4.3.2 Microscale Damage Tensor

As mentioned earlier, a single FCC crystal will contain 12 slip systems, comprised of four slip planes each with three slip directions. By using Eqn. (4.1 and 4.2), the damage parameter $\boldsymbol{D}^{(\beta)}$ for each slip system can be calculated. In order to incorporate all the damage information from 12 slip systems, a damage tensor is developed to indicate the damage status at a certain point. From the Eqn. (4.1), the damage parameters in 12 slip systems are in a strain energy density form. Therefore, it is reasonable to assume the damage tensor is a symmetric tensor. On the other hand, the required damage tensor should reflect the direction effect for different slip systems. Thus, the relation between the damage tensor increment and the damage parameter increment in each slip system is developed as follows:

$$\mathbf{dD^k = n^k dDs^k}, \text{ k=1 to 12} \qquad (4.3)$$

A symmetric tensor has six components. The first attempt to derive the unique damage tensor from the 12 equations failed; therefore, another attempt was made

using optimization to derive the damage tensor. The objective function in increment form is shown below:

$$\mathbf{E^2} = \sum_{k=1}^{12} [\mathbf{Error^k}]^2 \; ; \; \mathbf{Error^k} = \mathbf{dD^k} - \mathbf{n^k dDs^k} \qquad (4.4)$$

where k denotes the number of slip system; n and s denote the normal and slip direction for each slip system, respectively.

Minimization of the objective function yields:

$$\begin{aligned} \frac{\partial \mathbf{E^2}}{\partial \mathbf{D}} &= \sum\nolimits_{\mathbf{k=1}}^{\mathbf{12}} \left[2\mathbf{n_m^k dD_{ml} s_l^k n_i^k s_j^k} - 2\mathbf{dD^k n_i^k s_j^k} \right] \\ &= 2 \sum\nolimits_{\mathbf{k=1}}^{\mathbf{12}} \left[\mathbf{n_m^k dD_{ml} s_l^k n_i^k s_j^k} \right. \\ &\quad \left. - \mathbf{dD^k n_i^k s_j^k} \right] = \mathbf{0} \end{aligned} \qquad (4.5)$$

By expanding Eqn. (4.5):

$$\mathrm{A} + \mathrm{B} + \mathrm{C} + \mathrm{D} + \mathrm{E} + \mathrm{F} = \sum\nolimits_{k=1}^{12} \mathbf{n_i^k s_j^k dD^k} \qquad (4.6)$$

where $\mathrm{A} = \left[\sum_{k=1}^{12} \mathbf{n_i^k s_j^k n_1^k s_1^k}\right] \mathbf{dD_{11}}$, $\mathrm{B} = \left[\sum_{k=1}^{12} \mathbf{n_i^k s_j^k} (\mathbf{n_1^k s_2^k + n_2^k s_1^k})\right] \mathbf{dD_{12}}$

$$\mathrm{C} = \left[\sum_{k=1}^{12} \mathbf{n_i^k s_j^k} \left(\mathbf{n_1^k s_3^k + n_3^k s_1^k}\right)\right] \mathbf{dD_{13}}, \; \mathrm{D} = \left[\sum_{k=1}^{12} \mathbf{n_i^k s_j^k n_2^k s_2^k}\right] \mathbf{dD_{22}}$$

$$\mathrm{E} = \left[\sum_{k=1}^{12} \mathbf{n_i^k s_j^k} (\mathbf{n_2^k s_3^k + n_3^k s_2^k})\right] \mathbf{dD_{23}}, \; \mathrm{F} = \left[\sum_{k=1}^{12} \mathbf{n_i^k s_j^k n_3^k s_3^k}\right] \mathbf{dD_{33}};$$

With the constraint that the slip normal is perpendicular to the slip direction, i.e. $n_i s_i = 0$, the linear equations shown in Eqn. (4.6) reduce to only five independent equations. To determine the six components of the damage tensor, an

additional equation is required. The additional equation comes from the constraint that the sum of the error for each slip system obtained from Eqn. (4.4) should be zero. It gives:

$$\begin{aligned}
&\left[\sum_{k=1}^{12} n_1^k s_1^k\right] \mathbf{d}D_{11} + \left[\sum_{k=1}^{12} (n_1^k s_2^k + n_2^k s_1^k)\right] \mathbf{d}D_{12} \\
&\quad + \left[\sum_{k=1}^{12} (n_1^k s_3^k + n_3^k s_1^k)\right] \mathbf{d}D_{13} \\
&\quad + \left[\sum_{k=1}^{12} n_2^k s_2^k\right] \mathbf{d}D_{22} \\
&\quad + \left[\sum_{k=1}^{12} (n_2^k s_3^k + n_3^k s_2^k)\right] \mathbf{d}D_{23} \\
&\quad + \left[\sum_{k=1}^{12} n_3^k s_3^k\right] \mathbf{d}D_{33} = \sum_{k=1}^{12} dD^k
\end{aligned} \tag{4.7}$$

This procedure yields a damage tensor capable of predicting damage growth rate and direction of damage evolution simultaneously by computing the maximum eigenvalue and the corresponding eigenvector.

A simulation for a simple test case is illustrated in Fig. 4.5. All the material properties for Al 2024 used in the model are represented in Chapter 2 (Table 4.2). The results are slightly counterintuitive. At some points, the maximum eigenvalue becomes negative, which has no physical meaning. Consequently, the damage tensor is decomposed into a deviatoric part and a hydrostatic part. Since damage is driven by plasticity and the damage tensor is developed to reflect the slip effect, the deviatoric part of the damage tensor should also contain the necessary information. The maximum eigenvalue and the corresponding eigenvector of the

deviatoric part appear to provide reasonable results in the context of damage accumulation.

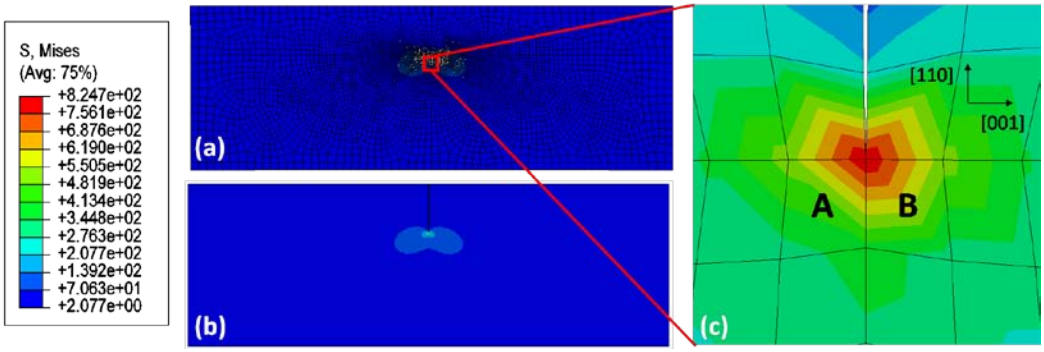

Figure 4.5 Simulation for simple tension on a pre-cracked single crystal plate. (a) Mesh of the plate; (b) Mises stress distribution in the plate; (c) Enlarged area at the crack tip.

The corresponding eigenvectors shown in Table 4.2 for element A, which is in front of the crack tip, are very close to the experimental results. Table 4.2 shows that the damage accumulates almost in the X-Y plane for most of the time and slowly changes direction from approximately [1 0 0] to [0.756 -5.38 0.00831]. This direction almost lies in the X-Y plane and in the slip plane, whose normal is [0.577 0.816 0] as shown in Table 4.3. It should be noted that all the directions presented in Table 4.3 are based on a global Cartesian coordinate system. By checking element B, which lies at the right side of the crack tip, the direction of the corresponding eigenvector and the one on the LHS are symmetric with respect to the [110] direction. This is in accordance with experimental results observed in Refs. 105 and 106 (shown in Fig. 4.6), with the two potential slip planes being [0.577 0.816 0] and [0.577 -0.816 0].

Table 4.2 Eigenvector corresponding to the maximum eigenvalue of deviatoric part

Time(s)	X	Y	Z
7.95E-02	9.20E-01	-1.47E-01	2.22E-01
9.95E-02	8.68E-01	-1.73E-01	3.69E-01
1.10E-01	8.71E-01	-1.88E-01	3.58E-01
1.30E-01	8.27E-01	-3.70E-01	3.63E-01
⋮	⋮	⋮	⋮
2.30E-01	7.94E-01	-5.10E-01	2.75E-01
2.60E-01	7.59E-01	-4.90E-01	3.27E-01
2.70E-01	7.49E-01	-5.37E-01	-6.77E-03
2.80E-01	7.56E-01	-5.38E-01	8.31E-03

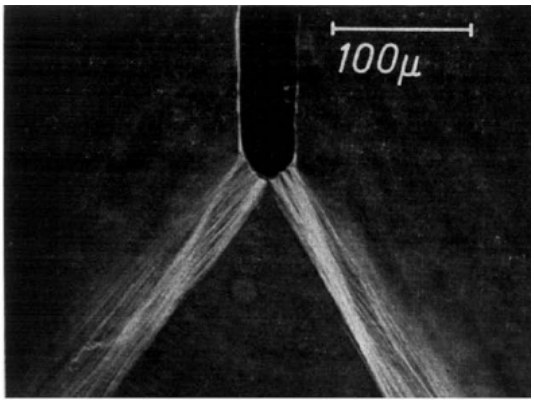

Figure 4.6 SEM micrograph showing the slip prior to the crack tip [106]

Table 4.3 Twelve slip systems

Normal to slip plane	slip directions
0.577,0,0.816	0.707,0.5,-0.5
	-0.707,0.5,0.5
	0,-1,0
0.577,-0.816,0	0.707,0.5,0.5
	0,0,1
	0.707,0.5,-0.5
0.577,0.816,0	0.707,-0.5,0.5
	0,0,1
	-0.707,0.5,0.5
-0.577,0,0.816	0.707,-0.5,0.5
	0.707,0.5,0.5
	0,-1,0

4.3.3 Mesoscale Damage Vector

Kreisselmeier-Steinhauser (KS) Function

Damage is believed driven by plastic deformation. Thus, in this chapter, the coupling between damage and elasticity is not considered. The principal idea of this approach is to develop a multiscale concept and formulate a damage index for an RVE based on current stress-strain distribution, which can represent the damage status of the RVE considering some of the microstructure features. Therefore, several optimization methods and averaging techniques are used to select the critical local damage information and transfer it to a global damage variable. For this purpose, a Kreisselmeier-Steinhauser (KS) function based approach is used to account for the contribution from all grains to the total damage accumulation at mesoscale. The KS function-based approach makes the current multiscale model a statistical model rather than a progressive damage model. It incorporates the criteria that allow contribution from the more critical grains to be reflected in the damage calculation. Traditionally, KS function is used in optimization applications involving multiple objective functions and/or constraints [107]. From a mathematical point of view, the KS function represents an envelope function (for a set of functions), as shown in Fig. 4.7 and defined as:

$$\boldsymbol{KS}[\boldsymbol{g_i}(\boldsymbol{x})] = -\frac{\mathbf{1}}{\boldsymbol{\rho}}\mathbf{ln}[\sum_{\boldsymbol{i}} \boldsymbol{e}^{-\boldsymbol{\rho h_i}(\boldsymbol{x})}] \tag{4.8}$$

where $\boldsymbol{\rho}$ is a parameter that determines the proximity of the KS function to the boundary of the multiple objective functions $\boldsymbol{h_i}(\boldsymbol{x})$. In this work, the multiple objective functions ($\boldsymbol{h_i}(\boldsymbol{x})$) are the damage growths of all the grains in a meso

RVE as functions of the time. When $\boldsymbol{\rho}$ is positive, the KS function is close to the lower bound of $\boldsymbol{h_i(x)}$, and when $\boldsymbol{\rho}$ is negative, the KS function is close to the upper bound of $\boldsymbol{h_i(x)}$. However, Eqn. (4.8) cannot be used directly in this application due to the nature of the exponential term. The modified KS function form is derived as:

$$\mathbf{KS}[\boldsymbol{h_i(x)}] = \begin{cases} \mathbf{Max}\big(\boldsymbol{h_i(x)}\big) + \dfrac{\mathbf{1}}{\boldsymbol{\rho}}\mathbf{ln}[\sum_{\boldsymbol{i}} \boldsymbol{e}^{\boldsymbol{\rho}(\boldsymbol{h_i(x)}-\mathbf{Max}(\boldsymbol{h_i(x)}))}], & \textbf{upper bound} \\ \mathbf{Min}\big(\boldsymbol{h_i(x)}\big) - \dfrac{\mathbf{1}}{\boldsymbol{\rho}}\mathbf{ln}[\sum_{\boldsymbol{i}} \boldsymbol{e}^{-\boldsymbol{\rho}(\boldsymbol{h_i(x)}-\mathbf{Min}(\boldsymbol{h_i(x)}))}], & \textbf{lower bound} \end{cases} \quad (4.9)$$

where the max and min terms represent the gains with the highest and the lowest damage parameter, respectively.

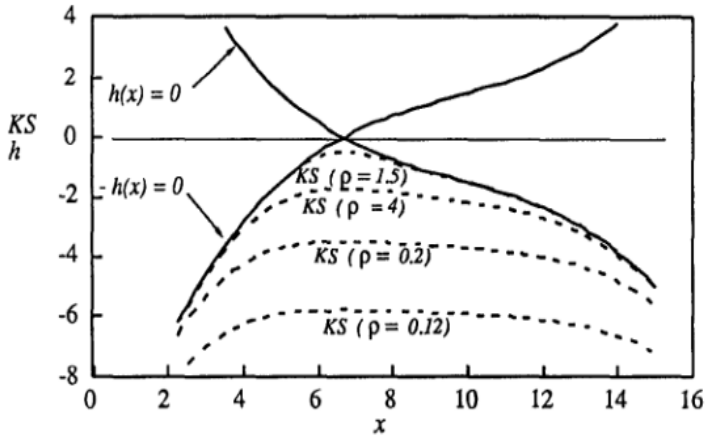

Figure 4.7 KS function [107]

Damage Parameter and Direction at the Mesoscale

As mentioned in section 4.1, a 1 mm×1 mm square is chosen as a meso RVE (Fig. 4.1) based on Ritchie's length definition of a physically small crack [99].

The procedure to create meso RVE mesh comprises two steps. First, an Electron Backscattering Diffraction (EBSD) scan is used to acquire the microstructure of the material including grain orientations, grain shapes, and sizes. Second, a software package OOF (Object-Oriented Finite element analysis from NIST) is used to graphically assign the material properties to a microstructure image for meshing. It should be pointed out that all the meso RVEs are generated directly from the EBSD scans of the material so that all the grain information used in the FE simulation is maintained similar to a real microstructure. Grain size and shape can affect the stress-strain distribution in the RVE, and consequently can impact damage prediction to some extent. However, grain size and shape effects are not explicitly considered in the constitutive model. Traditional single crystal plasticity is used to describe the material behavior at the hotspot area of the structural components. Stress/strain gradient effect, which takes account of the size effect in the constitutive model such as the mechanism based strain gradient crystal plasticity (MSG-CP) or other strain gradient theory, is not considered here. In order to get the damage parameter and direction at the mesoscale, each grain in the meso RVE (Fig. 4.1) is treated as a single unit. The output of each grain is a damage vector $\vec{D}$ obtained by using an averaging technique. Three simple steps are carried out to calculate the damage vector in each grain. First, the deviatoric part of the damage tensor is calculated for each element within a grain. Next, the deviatoric damage tensors of all the elements in the grain are averaged to get a single averaged damage tensor in which each component of the damage tensor comes from the mean value of the corresponding components of all the elements'

deviatoric damage tensor. Finally, the damage vector of each grain is calculated where the magnitude of the damage vector, D, is set equal to the maximum eigenvalue of the averaged damage tensor. The direction of the damage vector is defined by the corresponding eigenvector.

The magnitude of the damage vector, *D*, in each grain is a function of time. The upper and lower bound for *D* of all the grains within a meso RVE can be obtained by applying the KS function. The damage index for the meso RVE can be defined as:

$$D_{meso} = (\boldsymbol{\theta} \boldsymbol{KS_u} + (\mathbf{1} - \boldsymbol{\theta}) \boldsymbol{KS_l})/D_c \qquad (4.10)$$

where $\boldsymbol{\theta}$ is related to the critical damage value defined in Eqn. (4.11), total grain damage, and the total number of grains within a meso RVE. Physically, this parameter measures the number of grains that reaches the critical damage value, D_c . The critical damage value is also used to determine crack initiation in the meso RVE. The damage direction in the meso RVE can be obtained by normalizing the sum of all damage vectors for all grains. For prediction of fatigue crack initiation, the criteria should be related to the local damage parameter, i.e., the damage parameter *D* of each grain. When the maximum damage parameter of each grain within a meso RVE reaches the critical damage threshold, the corresponding number of fatigue cycles is treated as fatigue crack initiation and the corresponding grain with the maximum damage parameter is regarded as the crack initiation location. Moreover, the goal of using a damage index for meso RVE, D_{meso}, is to determine the failure of the RVE by checking whether D_{meso}

reaches one or not. In this work, for convenience of experimental validation, the failure crack length of the meso RVE is taken as 1mm considering the size of the meso RVE and the resolution of the digital image acquisition system used in the experiments. The meso RVE size is about 1mm×1mm and only the failure of the meso RVE is validated considering our current experimental capabilities.

4.3.4 Critical Damage Value for Crack Nucleation

For aluminum, the surface energy density [108] ω that corresponds to the energy variation per unit area due to the creation of surface at room temperature is 865.18 (MJ/m^2). In order to initiate a crack, the minimum energy required should be $2\times865.18\times l\times t$, where 2 indicates that there are two free surfaces for a crack. Parameters l and t are the characteristic length and width of the crack surface, respectively. In the simulation, l is chosen to be the average grain size obtained from an EBSD scan. In order to determine the critical damage value, an assumption is made that the cumulative damage due to plastic deformation in the meso RVE should be greater than the minimum energy for creating two free surfaces of a crack. The width of the meso RVE is chosen to be the same as the crack width so that the critical damage value is only a function of the average grain size l, the meso RVE size A and the surface energy density ω. The critical damage value is represented as follows:

$$D_c = \frac{2\times\omega\times l}{\mathrm{A}} \tag{4.11}$$

4.4 Results & Validation

4.4.1 Lug Joint Fatigue Tests

The lug joint is one of several ‘hotspots’ in aerospace structures that experience fatigue damage. Fatigue tests were performed on lug joint samples prepared from an Al 2024 T351 plate. An Instron 1331 hydraulic load frame was used to apply load to the samples. Figure 4.8 shows the experimental setup of the test. A digital image acquisition system was used to collect pictures from a Charge-Couple Device (CCD) camera to monitor potential locations of crack initiation and measuring crack length. A cyclic loading of 490 N (110 lbs) to 4900 N (1100 lbs) with a frequency of 20 Hz in sinusoidal waveform was applied to the lug joint sample through the bottom clevis. From images taken from the digital image acquisition system, a crack length vs. a number of cycles curve can be plotted. The number of cycles to get a 1mm crack in the sample can then be interpolated from this curve. Table 4.4 shows the number of cycles to obtain a 1mm crack for different lug specimens. The experiment results for 1 mm crack will be compared with the estimations of the 1 mm×1 mm meso RVE failure from the simulations. The images can also be measured to get the initial crack direction on the lug joint specimen, and subsequently compared with the potential crack directions obtained from the simulations.

Table 4.4 No. of cycles for 1mm crack in Lug joint fatigue tests

Lug Joint Specimens	No. of cycles to obtain 1mm crack
Sample 1	213k
Sample 2	220k
Sample 3	223k
Sample 4	125k

(a) 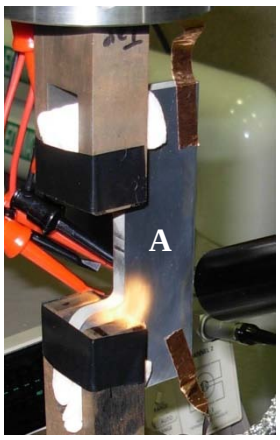

(b) 

Figure 4.8 Lab setup for fatigue tests of structural components with digital image acquisition system monitoring the crack length; A-Lug joint sample, B-Hydraulic Frame, C-CCD camera, D-Digital Image Acquisition system

4.4.2 Lug Joint Numerical Simulations

For computational efficiency, a two-scale mesh is used in the multiscale analysis of complex structural components such as a lug joint. Preliminary stress analysis has been conducted by applying homogeneous elasto-plastic material model to identify the hotspot of the structural component in ABAQUS. The meso RVE mesh generated using the software OOF has been used at the hotspot of the lug joint. A detailed description of this procedure is presented in chapter 2. The rest of the lug joint is described as a homogenous material. The constitutive relation of this homogeneous material was obtained by homogenizing the meso RVE stress-strain response. First, a force was applied at the right edge of the meso RVE where plane stress elements were used. The UMAT based on single crystal plasticity has been used to describe material behavior for each grain within the meso RVE. Then, the displacement of each node at the edge was calculated. The corresponding homogenized meso RVE stress-strain response can be plotted

based on the applied load and the displacement of each node. This curve was used to perform the plane stress simulations [100]. The two-scale mesh was generated using the commercial software Altair Hypermesh. Figure 4.9 shows the two-scale mesh of the lug joint. For this work, all the simulations were carried out in 2D. Three nodes and four nodes plane stress elements (CPS3 and CPS4) are used for the FE simulations of the lug joint to investigate the surface of the specimen. Symmetric boundary conditions were used for simulation so that only half of the lug joint was analyzed in ABAQUS. The same cyclic loading condition which was used during the fatigue test, that is, 490 N (110 lbs) to 4900 N (1100 lbs) with a frequency of 20 Hz in sinusoidal waveform applied at the pin hole of the lug is used in simulation. Figure 4.10 shows the von Mises stress distribution in the lug joint under simple tension with the enlarged hotspot area showing the non-uniform distribution due to different grain orientations.

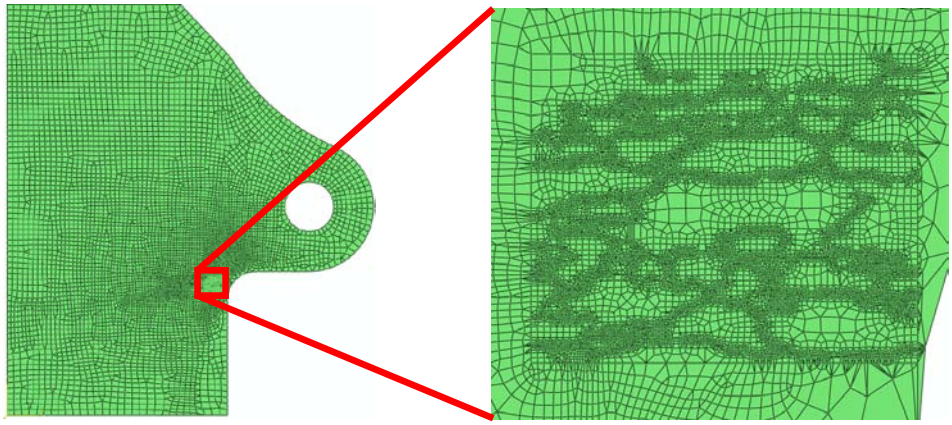

Figure 4.9 Finite element mesh of lug joint

The previously described damage tensor was implemented in the UMAT and a data processing code was also developed in Matlab. Damage evolution for all

grains in the meso RVE is plotted in Fig. 4.11 for 20 cycles. Figure 4.11 shows that after 10 cycles, the damage evolution in each grain becomes stable, which provides a basis for using a linear fit to extrapolate the damage evolution in individual grains. It should be noted that, the focus of this work was to propose a new methodology for fatigue damage prediction taking into consideration microstructure features. Therefore, all simulations conducted and presented here are under constant cyclic loading. Thus, the damage evolution in each grain becomes almost linear after 10 cycles. For random loading conditions, future work will address building a relationship between the applied load and the damage growth in individual grains. Figure 4.12 (a) shows the damage parameter of all the grains within the RVE at time, t=1.2667s, and Fig. 4.12 (b) presents the enlarged area of the RVE and highlights the crack initiation area where the damage parameter was maximum. This critical grain is labeled as grain no. 9, shown in Fig. 4.12 (a). The results confirm that the critical grain in the RVE is located close to the free surface at the shoulder of the lug joint.

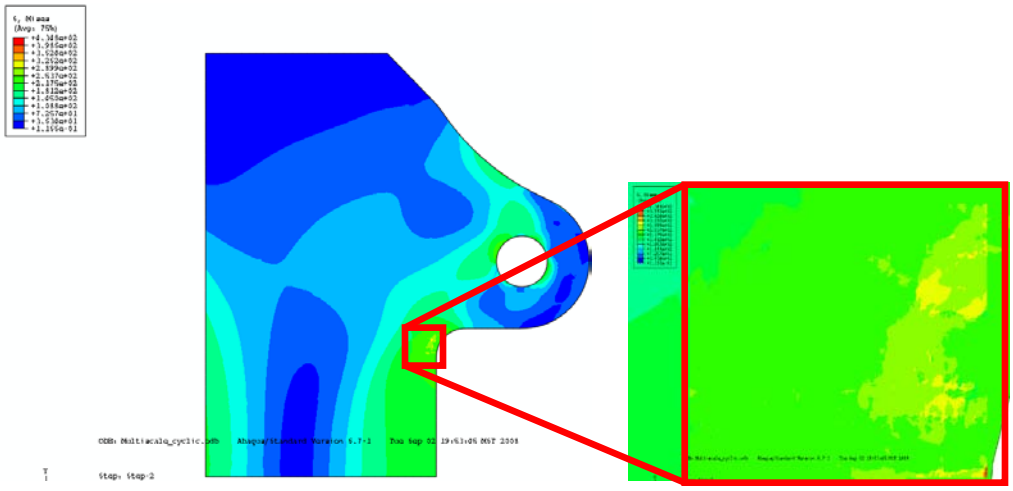

Figure 4.10 Mises stress distribution of lug joint

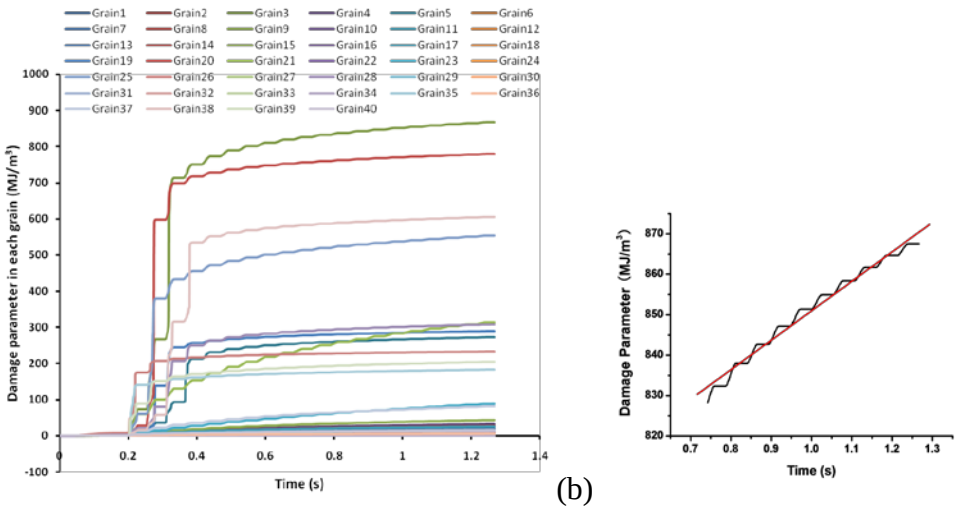

(a) (b)

Figure 4.11 (a) Damage evolution in each grain for 20 cycles, (b) An example shows that damage grows linearly after 10 cycles in each individual grain

(a)

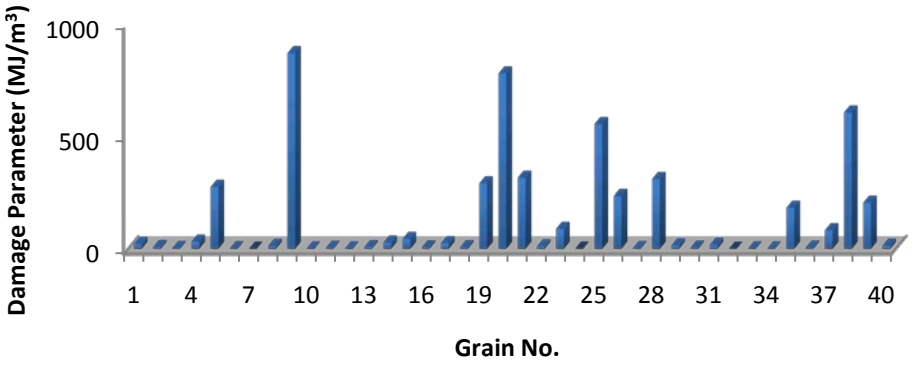

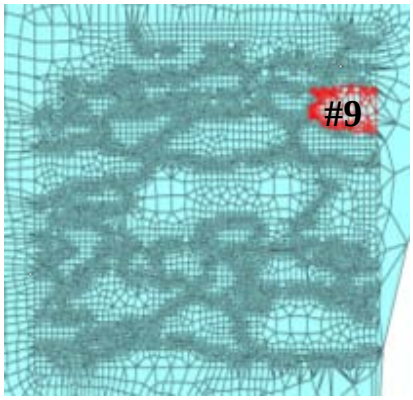

(b)

Figure 4.12 (a) Damage distribution in RVE for all grains, (b) Location of critical grain

A Matlab program was developed for post-processing of finite element results. Figure 4.13 shows the microstructure and the grain size distribution of the meso RVE used. Figure 4.14 presents the normalized damage parameter for the meso RVE versus the number of cycles. The simulation data fit a quadratic polynomial well, which is intuitive given that as more grains reach the critical damage value, the accumulation of damage in the meso RVE accelerates. The estimated number of cycles until failure in the meso RVE, i.e., when the normalized damage index of the meso RVE reaches an unit value, is 208Kcycles. The result of the simulation matches well with the experimental results of samples 1-3 shown in Table 4.5. The corresponding eigenvector, an indicator of the potential damage direction, is calculated by the weighted average method from all the grains. A histogram showing the frequency of damage occurrence along a particular direction is presented in Fig. 4.15 (a). The figure indicates that the directions of maximum damage in the RVE, obtained from simulation, are approximately -30°and 52 °. The experimental crack directions from lug joint fatigue tests are shown in Fig. 4.15 (b). Comparing the simulation results with the experimental data, one of the potential damage directions (-30°) obtained from the simulation matches the experiments well. Further simulations were conducted to verify the model and consider uncertainty of the meso RVE shown in Fig. 4.16. The same lug joint with only one meso RVE located at the shoulder was used. The meso RVEs, however, contain different oriented grains and different number of grains. As mentioned before, all meso RVE sizes are approximated to

1mm×1mm. The average grain size and estimated failure of meso RVEs are shown in Table 4.5.

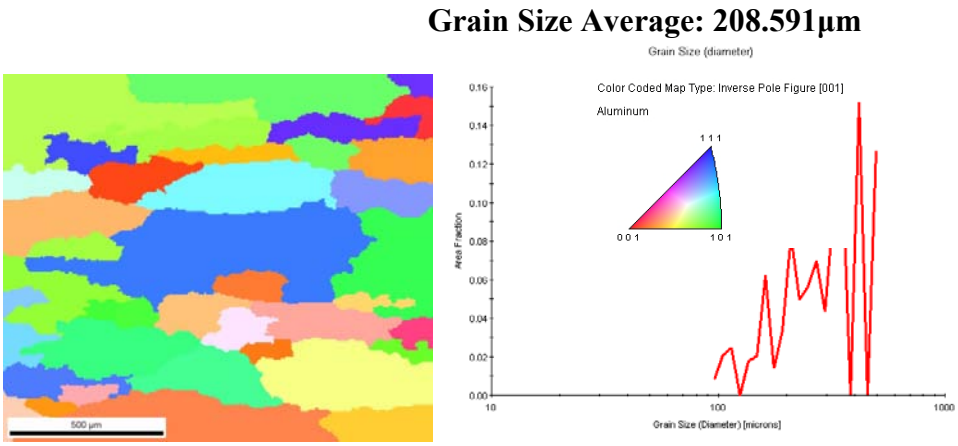

Figure 4.13 Microstructure and grain size distribution of the meso RVE

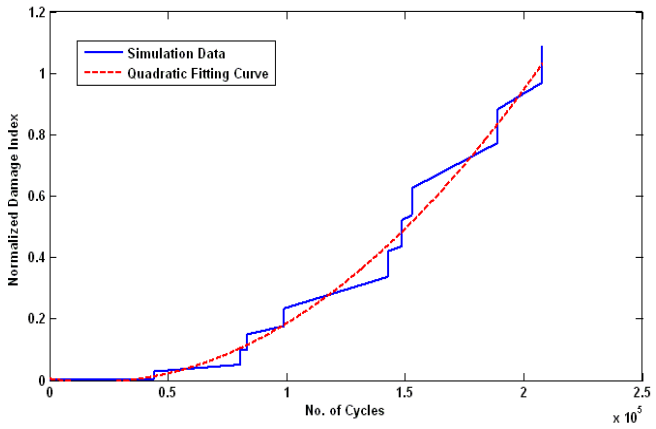

Figure 4.14 Normalized damage index for meso RVE vs. No. of cycles

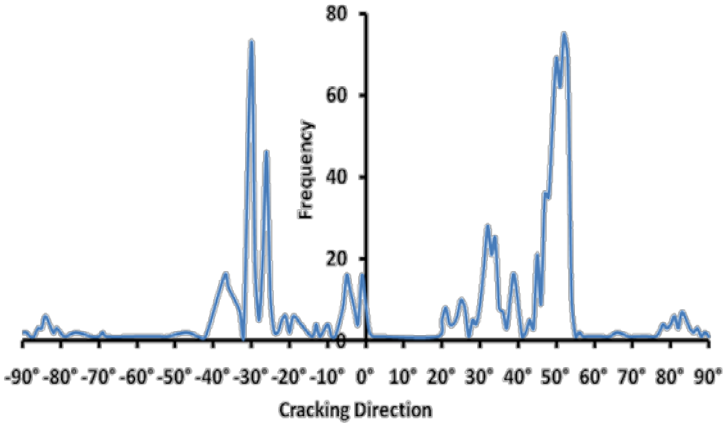

(a)

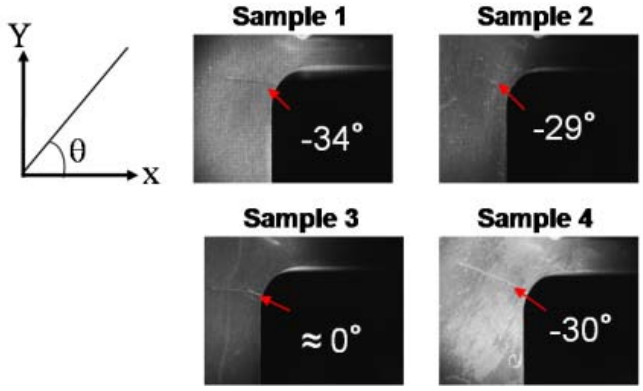

(b)

Figure 4.15 (a). Histogram of damage direction in RVE; (b). Cracking directions from fatigue tests

Figure 4.16 Finite element meshes of different lug joints

It can be observed that the estimation of RVE failure in simulation 5 is close to the fatigue test results obtained in sample 4. Variability in the simulation results

indicates that the fewer number of cycles required in sample 4 to obtain a 1mm crack could be due to different oriented grains.

The five simulations suggested that grain orientation will affect the estimation of RVE failure. The common feature in all five simulations is the fact that the RVEs used in the simulations are generated from the scans taken from the same Al alloy plate. However, those scans are not directly taken from the lug joint samples, which results in the variability of the input data for the model. To prevent this variability, an RVE which is directly scanned from the lug joint shoulder is created (shown in Fig. 4.17). The procedure involves obtaining four scans from both shoulders of the lug joint on both sides and conducting a fatigue test on the same lug joint sample to determine which scan should be used in the validation simulation. For this fatigue test, the loading was changed from 150 lbs to 1500 lbs. Because of the high loading condition and high frequency, the number of cycles to obtain a 1 mm crack in the lug joint was not recorded. The lowest number of cycles recorded was 33k cycles to initiate a 1.5 mm crack (shown in Fig. 4.18).

Table 4.5 Average grain size and estimation of failure for different meso RVEs

Lug Joint Simulations	Simulation 1	Simulation 2	Simulation 3	Simulation 4	Simulation 5
Average grain size (μm)	208.591	191.866	190.266	242.684	191.082
Estimate failure of RVE (K cycles)	208	184	298	177	116

(a) 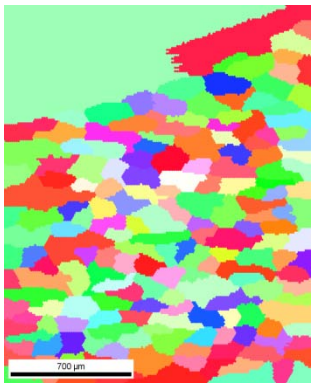

(b) 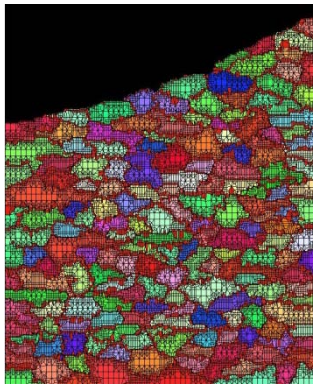

Figure 4.17 (a). EBSD scan directly from the shoulder of lug joint sample; (b). Finite element meshes created from OOF

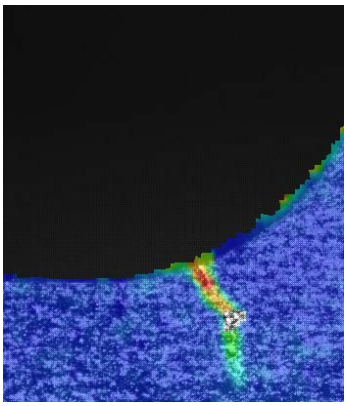

Figure 4.18 Crack reaches 1.5 mm

The simulation result of RVE failure is found to be 12.4 k cycles. Considering the number of cycles required for short crack propagation up to 1.5 mm that can be obtained experimentally, the author believes the simulation result is acceptable. The direction of crack propagation at the early stage of fatigue test is around -53° with respect to the horizontal direction, as shown in Fig. 4.18. The histogram of the simulation for potential crack direction is presented in Fig. 4.19. Results show two major potential crack direction bands. One is from approximately -58° to -43° and the other is from 60° to 85°. The experiment result shows the crack

propagated along one of the potential crack direction ranges obtained from the simulation, indicating that the model can predict potential crack directions.

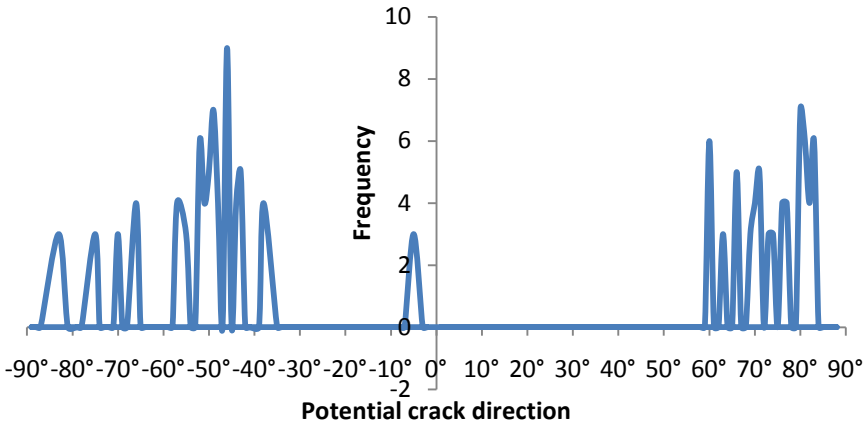

Figure 4.19 Histogram for potential crack direction

4.4.3 Cruciform Fatigue Tests

In this section, the energy-based damage model is applied for multiaxial loading. The simulation results are verified through experiments conducted using the biaxial torsion MTS test frame. A cruciform specimen is designed for biaxial loading. The dimensions of the cruciform specimen are shown in Fig. 4.20. Initial stress analysis on the cruciform specimen under equibiaxial loading is first conducted in ABAQUS to obtain an insight into the high stress concentration zones. Only one quarter of the specimen is analyzed due to symmetry of the specimen and the equibiaxial loading condition (Fig. 4.20). Figure 4.21 shows a perfect uniform 2D stress distribution in the gage area of the cruciform specimen. This makes it hard to initiate crack at the gage area. In order to make the specimen conducive to crack initiation, a quarter-inch diameter hole was made at the center of the gage area, shown in Fig. 4.22. A fatigue test on the cruciform

specimen with a hole at the center was conducted. It was found that crack initiation still takes considerable time to appear. Therefore, a 1 mm notch at the hole along a 45 degree angle with respect to the vertical direction was made to accelerate crack initiation as shown in Fig. 4.23. Image mesh software OOF (from NIST) is used to generate refined mesh from the EBSD scan in the high stress concentration zone at the tip of the notch. Single crystal plasticity theory is adopted to capture grain size and orientation effects of Al 2024 in the refined mesh area. Subsequently, a two-length scale mesh for cruciform specimen is generated, as shown in Fig. 4.24 via a powerful mesh software called Hypermesh. This two-length scale mesh combines two parts Part A, the high stress concentration area, i.e. the tip of the notch, and Part B, the remaining area of the cruciform sample. Single crystal plasticity is used to describe the material behavior at Part A, while the average stress-strain response of the meso RVE, which is obtained from around 1mm×1mm EBSD scan, is used to describe the rest of the homogenized area of the cruciform sample. The multiscale fatigue damage criterion is applied to the cruciform simulation.

In order to take into account the effect of individual grain sizes, the weight factor $\boldsymbol{\theta}$ in Eqn. (4.10) is modified in this section. The original weight factor measures the number of grains that reach the critical damage value and is simply calculated as:

$$\boldsymbol{\theta} = \frac{\boldsymbol{n}}{\boldsymbol{N}} \tag{4.12}$$

where $\boldsymbol{n}$ is the number of grains that reaches the critical damage value, and $\boldsymbol{N}$ is the total number of grains within the RVE. Considering individual grain sizes, Eqn. (4.10) is modified as follows:

$$\boldsymbol{\theta = \frac{a}{A}} \tag{4.13}$$

It should be noted that Eqn. (4.12) and Eqn. (4.13) are identical when all the grains in the meso RVE are the same size.

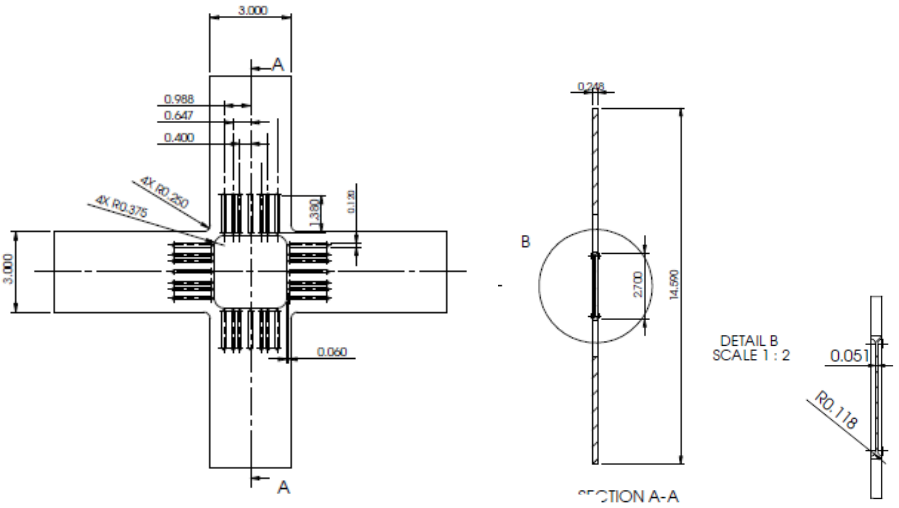

Unit: inch

Figure 4.20 Detail dimensions of the cruciform specimen

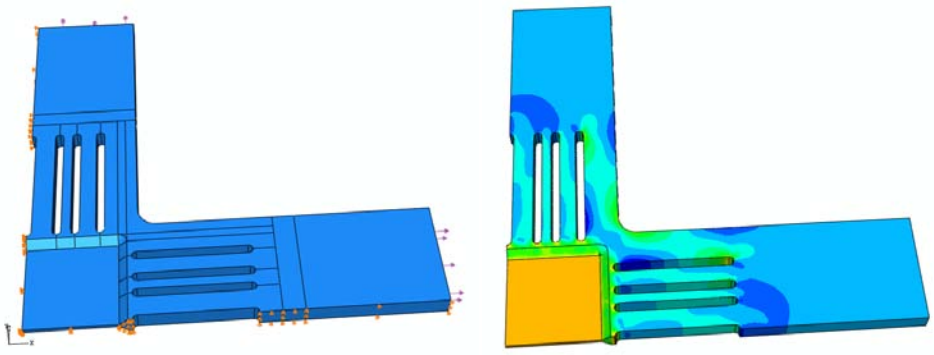

Figure 4.21 a) A quarter part of the cruciform specimen b) Mises stress distribution in the cruciform quarter part under equibiaxial loading

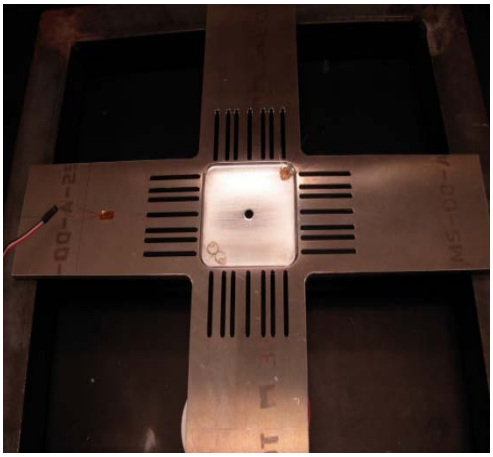

Figure 4.22 Cruciform specimen with a hole at the center for fatigue test

Figure 4.23 Cruciform specimen with a 45o notch at the center hole for fatigue test

(a) 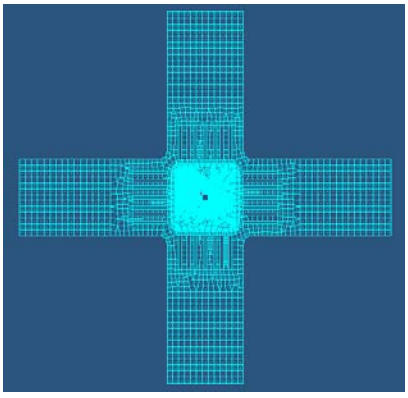

(b) 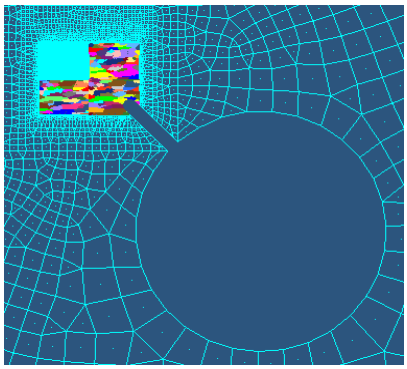 **(c)** 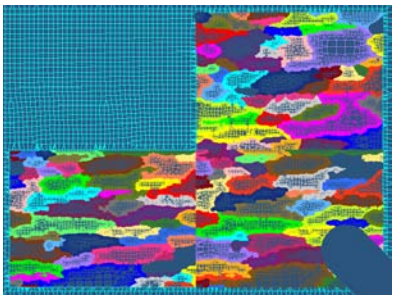

Figure 4.24 (a) Two length scale mesh of cruciform specimen; (b) Enlarged image of mesh at the hole; (c) Enlarged image of mesh at the tip of the notch (including 3 refined meshes from 3 EBSD scan; different colors represent different grains)

4.4.4 Experiment Setup & Fatigue Tests

The biaxial torsion MTS machine shown in Fig. 4.25 was used for biaxial loading. Digital image acquisition system was used to collect pictures from a CCD camera for monitoring potential locations of crack initiation and measuring crack length. A cyclic equibiaxial loading of 480 lbs to 4800 lbs with a frequency of 20 Hz in sinusoidal waveform was applied to the cruciform sample along horizontal and vertical directions, respectively.

It took 30K cycles to get a 1mm crack at tip of the notch and 143K cycles to get the gage area ruptured as shown in Fig. 4.26 & 4.27, respectively.

Figure 4.25 Experiment setup

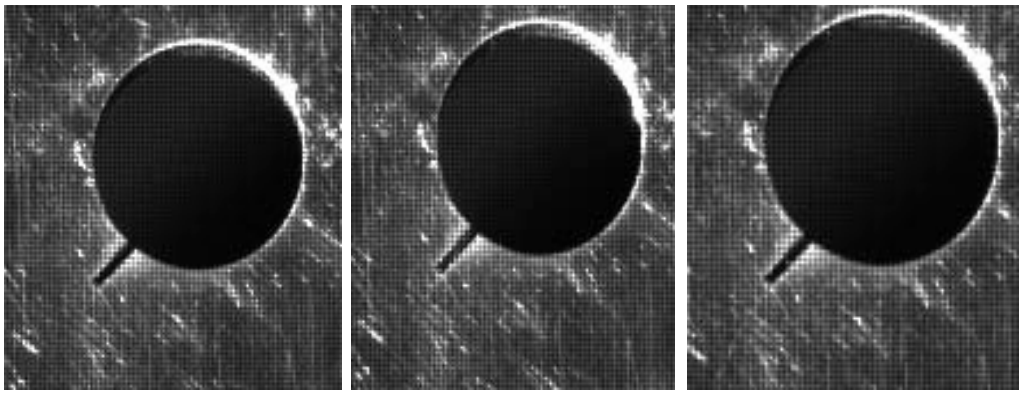

Figure 4.26 Crack propagation in cruciform sample; second image shows a 1mm crack start from notch tip

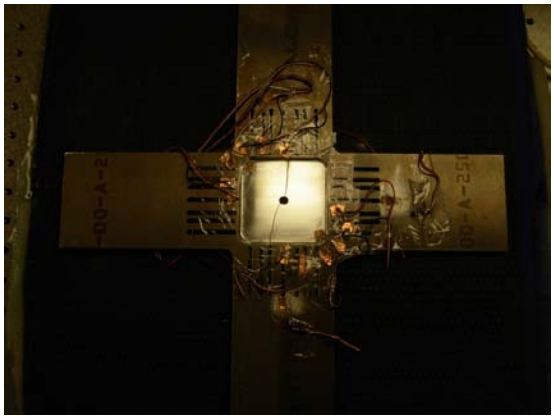

Figure 4.27 Fatigue experiment

Three more fatigue tests were conducted under the same load condition to check the variability. The initial crack directions from the four fatigue tests are presented in Fig. 4.28. The number of cycles needed to get 1mm crack that corresponds to the dimension of the meso RVE and the initial crack direction are measured carefully and listed in Table 4.6.

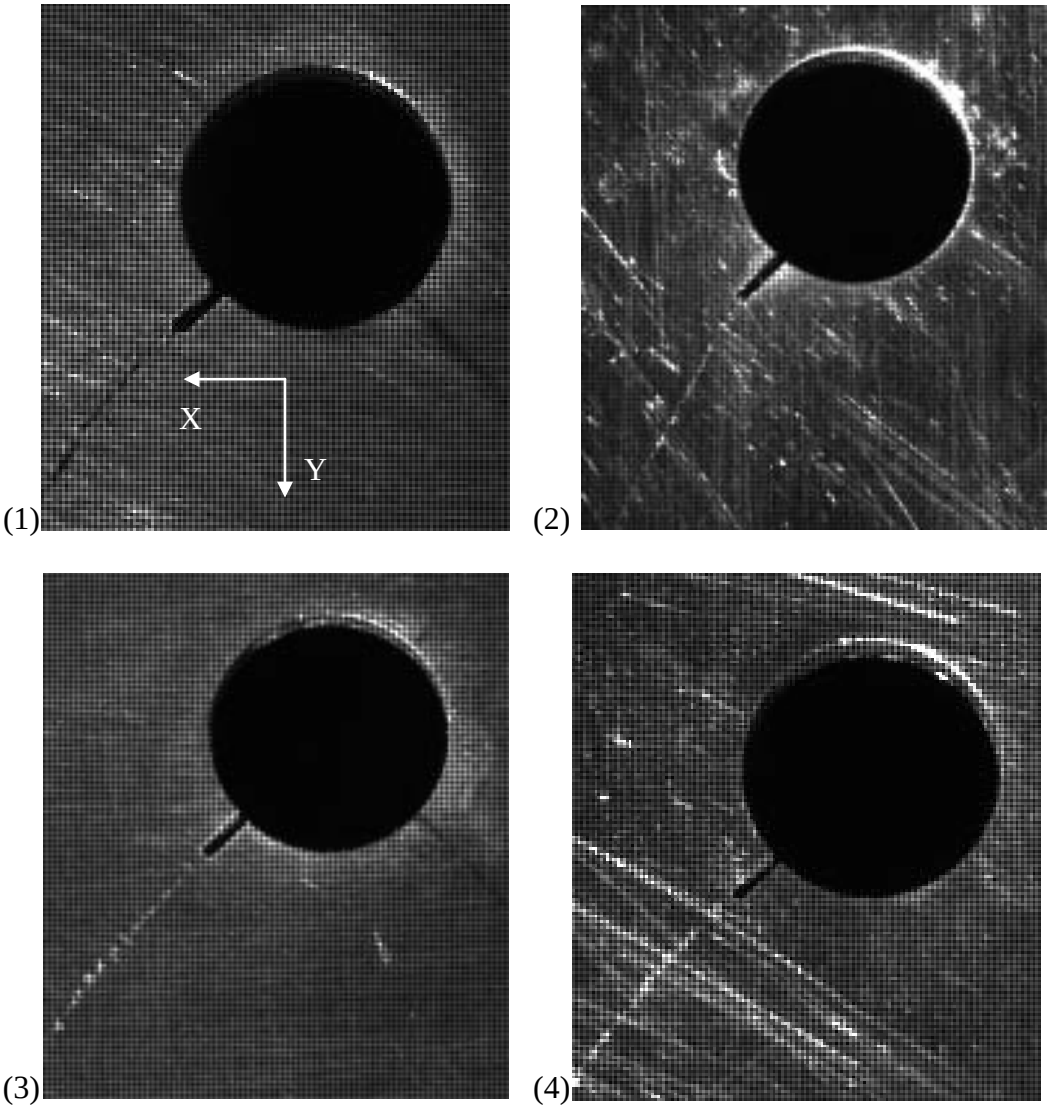

Figure 4.28 Initial crack directions in four fatigue tests

Table 4.6 Fatigue tests to 1mm crack

Sample No.	1	2	3	4
No. of cycles to 1 mm crack (Kcycles)	30	25.5	31.5	31.5
Initial crack direction	48°	62°	47°	47°

4.4.5 Cruciform Simulation Results

Two major steps were conducted to predict the failure of the meso RVE. First step was to calculate stress and strain distribution in the cruciform sample for 20 cyclic loading. Second step was to apply the fatigue damage criterion to estimate the failure of meso RVE and the direction of the crack based on the stress-strain distribution obtained from the first step. Stress analysis was performed in ABAQUS with a user-defined material subroutine (UMAT), which can implement single crystal plasticity for the refined mesh area using the two-length scale mesh generated in Hypermesh. The same equibiaxial load condition as used in fatigue test, i.e., 480 lbs to 4800 lbs with a frequency 20 Hz was applied to the cruciform model in the numerical simulation. The Mises stress distribution around the notch is shown in Fig. 4.29 (a) and (b). The two images are taken at the same time to show where the refined mesh is located (Fig. 4.29 (a)) and to provide a clear visual representation of the Mises stress distribution around the notch tip without mesh (Fig. 4.29 (b)). Figure 4.29 (b) shows clearly that only a small area around the notch tip experienced plastic deformation while the rest of the cruciform experienced only about 30% of yield stress during first 20 cycles. Since

fatigue damage is mainly caused by plastic deformation, the stress distribution demonstrated suggests that the limited high stress concentration zone around notch tip is a major part of the contribution to crack initiation and short crack growth. It also justifies the adoption of the two-length scale mesh with separated material constitutive models. After stress and strain are calculated in the cruciform sample, the fatigue damage criterion is applied for calculating the damage index of meso RVE for the RVE failure estimation and for crack direction prediction. As shown in Fig. 4.29 (a), the refined mesh area consists of three square meso RVEs formed as an L-shaped mirror image. Damage parameters are calculated only within the meso RVE, which is directly connected to the notch tip regarding the stress distribution around the tip.

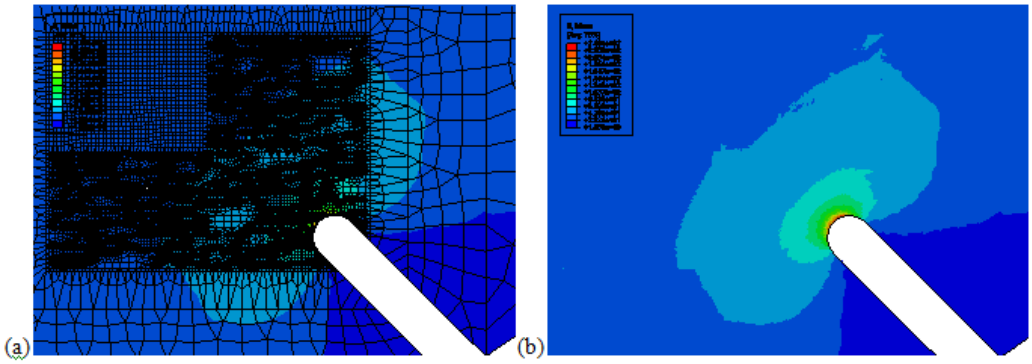

Figure 4.29 (a) Refined mesh located in front of notch tip; (b) Mises stress distribution around the notch tip

Figure 4.30 shows the damage parameter evolution in all the grains of the meso RVE. Figure 4.30 shows an important observation, namely the damage evolution in each grain becomes stable after 10 cycles (around 0.73s in time); thereafter, damage increment of individual grain during one cycle almost remains the same. Using a linear fit to extrapolate the damage evolution for each grain

seems feasible. Following this approach and using the modified equation for weight $\boldsymbol{\theta}$ (see Eqn. (4.13)), the damage index for meso RVE is calculated and shown in Fig. 4.31. The failure of meso RVE is defined as when damage index reaches 1. The estimated failure of meso RVE from numerical simulation is about 29.5K cycles as shown in Fig. 4.31, which is close to the experimental result of 30K cycles. In section 4.4.2, the damage index growth of meso RVE for the lug joint under uniaxial loading is presented, which fits well into a quadratic polynomial. Unlike the damage index growth in the lug joint sample, the damage index in the cruciform specimen grows approximately linearly. Comparing the stress field within the high stress concentration zone in the lug joint sample and cruciform sample explains the difference in damage index growth. High stress is scattered more uniformly in the lug joint sample than in the cruciform sample. Therefore, more grains in the meso RVE reach the critical damage value and contribute to the damage index of meso RVE in the lug joint sample. As more grains reach the critical damage value, the accumulation of damage in meso RVE is accelerated. Conversely, only several grains reach the critical damage value before the failure of meso RVE in the cruciform case. This makes the damage index of meso RVE depend on those grains for the most part of the RVE failure's life. Since the damage parameter is extrapolated linearly for each grain, the damage index of meso RVE will grow linearly if only a few grains contribute to the damage evolution of meso RVE.

The same procedure described in section 4.3.4 is applied to predict the most potential cracking directions in meso RVE. The result for the potential crack

directions of the first simulation is shown in Fig. 4.32. Figure 4.32 shows that within the life span of the RVE, there are three directions, i.e., -50°, 47°, and 72° that accumulate the most damage. These three directions also represent the most potential crack directions in meso RVE. The crack direction at the tip of the notch is accurately measured using the digital image from the fatigue test (Fig. 4.33). This shows that the crack direction at the beginning of the crack is 48° with respect to positive X-axis, which is close to one of the predicted potential crack directions.

Four more simulations were conducted to investigate the multiscale fatigue model and the uncertainty of the meso RVE through the same procedures. All simulations were performed on the same cruciform sample with the same load condition. The locations for the meso RVE and the RVE size were the same whereas different meso RVEs were used at the tip of the notch. The meso RVEs have similar material properties, but with different oriented grains and different number of grains. The estimated failure of the meso RVE and the potential crack directions for each simulation are listed in Table 4.7. It should be noted that the number of cycles to failure in simulation 3 & 4 are much higher than the other three simulations. This might be caused by the difference of the grain orientation distribution. It should be mentioned that all the meso RVE scans are taken from the same Al 2024 plate, which was used to make the cruciform samples. However, the scans are not directly taken from the exact area at the tip of the notch in the cruciform samples. Thus, strictly speaking, each meso RVE cannot represent the exact grain orientation distribution at the notch tip of the cruciform

samples used in fatigue tests. This is the reason why some of the simulation results are much different from the experimental data. It is noteworthy that once RVE failure estimation matches the test, the estimated crack direction is also close to the corresponding fatigue test. For example, comparing the fatigue tests from Table 4.6, simulation 1 gives the closest estimation of RVE failure to fatigue test 1. Meanwhile, the potential crack directions from simulation 1 also provide a close approximation to the test result. It was believed that the meso RVE used in simulation 1 is close to the real microstructure at the notch tip of the cruciform sample 1. Another example is from simulation 5 when compared to fatigue test 2. The failure of the RVE predicted from simulation 5 is close to the test 2. Simulation 5 provides an angle of 68° for potential crack direction, which is close enough to the test result of 62°. Although results from simulations 3 & 4 do not correspond exactly to the experimental data, the author believes that this may be true if the microstructure at the notch tip of a cruciform sample is close to the meso RVE used in simulation 3 & 4. In particular, simulation 4 provides only one crack direction of 84°. This means that the damage accumulates only along that direction during its life span. This direction also reflects the grain orientation distribution in the RVE, which indicates that slip planes of most grains in the RVE are oriented along this direction. The 84° direction is far away from the notch direction, which makes the damage accumulation along the direction difficult. This may explain why it takes much longer time to get the RVE failure.

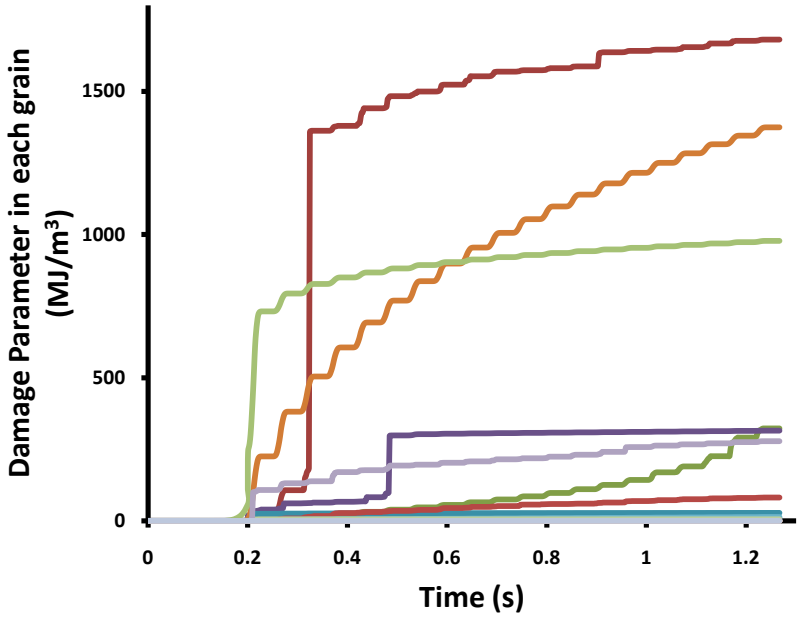

Figure 4.30 Damage evolution in each grain for 20 cycles

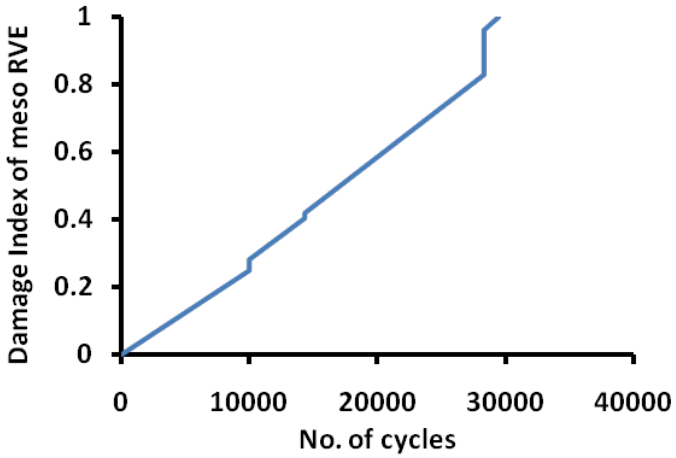

Figure 4.31 Damage index growth of meso RVE

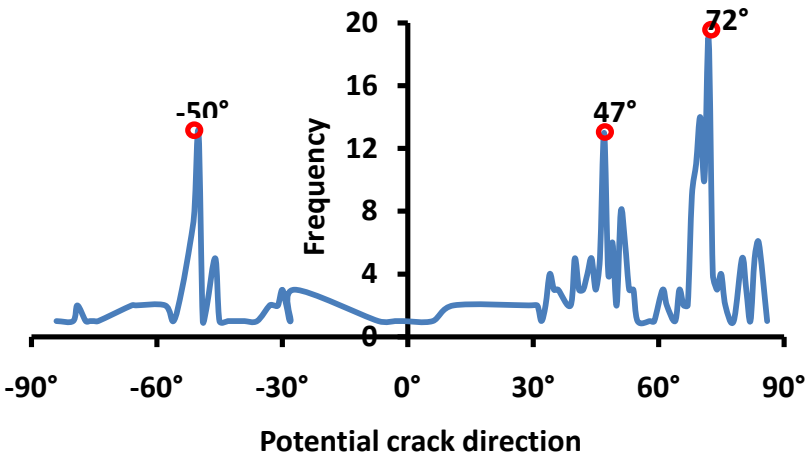

Figure 4.32 Potential crack direction obtained from simulation

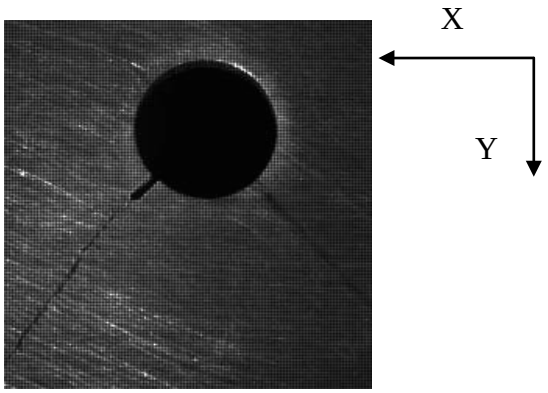

Figure 4.33 Crack direction from fatigue test

Table 4.7 Simulation results about failure of meso RVE

Simulation No.	1	2	3	4	5
No. of cycles to Failure (Kcycles)	29.5	19	70	236	26
Potential crack direcitons	-50°,47° 72°	-85°,17° 74°	-63°,18° 69°	84°	-85°,-34° 68°

4.5 Concluding Remarks

A multiscale damage criterion is developed considering grain orientation and size effects. Numerical simulations are conducted for lug joint and cruciform samples. The results show that the developed damage criterion is able to provide accurate prediction of the RVE failure as well as potential cracking directions in complex structural components under different load conditions. The simulation results of different RVEs indicate that structural failure has a strong dependence on the material microstructures.

Chapter 5

Virtual Sensing

5.1 Introduction

Research in structural health monitoring (SHM) has been focused, for the most part, at the structural or component level where repair and maintenance decisions are made using data obtained from sensors and macroscale models [105-111]. However, defects, such as cracks, initiate at the smaller length scales before manifesting at the macroscale, which constitutes a crucial factor in ultimate structural failure. Physics-based multiscale modeling can be used for predicting nucleation and growth of defects that track the evolution of the microstructure and forecast structural failure. These models also provide useful information for identifying the presence of micro cracks, which are the precursors to macro level damage. However, for the models to be effective, they must incorporate mechanisms to quantify and propagate important damage related parameters across the relevant length scales while considering major uncertainties, such as grain orientation and size at the microscale. Development of efficient multiscale modeling techniques will eliminate the need to test every conceivable damage scenario for every system. This will result in improved state estimation and robust prognosis procedures capable of assessing system performance under a broad range of future loading conditions. The importance of incorporating multiscale models in an SHM framework has gained recognition in recent years [100, 112-114]. An integrated framework for structural health monitoring (SHM) and

damage prognosis of metallic aerospace components is currently being developed by Chattopadhyay et al. [115].

The detection of incipient damage in metallic structures has been a challenge for decades. The guided wave-based damage detection techniques that are currently available focus on the detection of millimeter to centimeter level cracks [116-119]. The detection of incipient damage, however, such as plastic zones due to fatigue loading is still in its infancy. Incipient damage induces subtle changes in the measured guided wave signals, and these changes are often disregarded as noise. By modeling the interaction of a Lamb wave with incipient damage in a noise free environment allows for the evaluation of the perturbation of sensor signals due to previously undetectable damage. This information can then be used to extract detailed damage information to improve detection performance.

In this chapter, the multiscale damage model discussed in the chapter 4 is combined with a wave propagation model to capture the effect of the damage precursor on the guided wave. The integrated multiscale model is used to simulate sensor signals, referred to as virtual sensing, in aluminum plates. The proposed virtual sensing concept developed in this work offers a number of advantages: i) provide information on micro crack nucleation; ii) extract information from regions on the structure that are not easily accessible for placing physical sensors, and iii) optimize the sensor locations and thereby reduce the number of physical sensors. An Al 6071 plate with a 1mm notch, provided for damage initiation and propagation, is used as the test article for numerical simulation and experimental validation.

5.2 Physics-based Multiscale Model

The crystal plasticity based multiscale damage criterion was developed and presented in the chapter 4. The evolution of damage is determined through identification of the crystallographic plane at which the maximum accumulated fatigue damage reaches a critical value. The direction of crack propagation is expected to be in the direction of the critical material plane. The results show that the damage criterion can predict the damage growth, as well as the cracking directions. In fact, the damage criterion can also provide local damage information versus global damage information. The damage distribution within the hotspot of structural components is calculated. Figure 5.1 shows the local damage information at six selected locations. The bar chart in Fig. 5.1 (b) shows the damage in six locations at four different times. At location 1, the damage parameter is very high at all times, which indicates a very high probability of crack initiation at location 1 when compared to location 3. In addition, damage accumulation at location 2 is much faster than the other five locations, which suggests that the crack is likely to occur at location 1 and propagate towards location 2. This damage information helps us to investigate damage growth and identify weak points in the structure component. It also aids in the design of sensor placement.

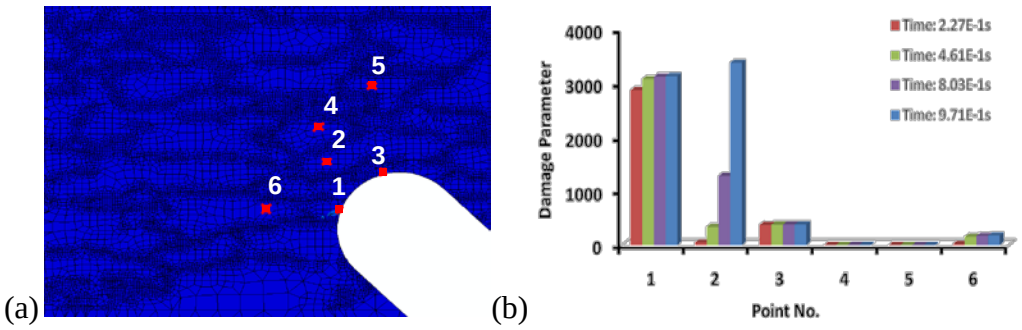

Figure 5.1 (a) Six selected locations around notch tip in a structure; (b) Damage information of the six locations at four different times

5.3 Virtual Sensing

5.3.1 Finite Element Model

Structural fatigue life is typically divided into two major sensing domains: undetectable region and detectable region. In the undetectable region, damage initiates and propagates at the microscale and cannot be detected using off-the-shelf sensors. In this approach, the multiscale model is used to investigate fatigue life in the undetectable region, thereby enhancing the sensitivity of damage detection and state awareness. The sensor data is simulated using FE models accounting for piezoelectrical-mechanical coupling. This concept is referred to as virtual sensing in this study. A three dimensional FE model is created with the commercial FE software ABAQUS/Standard [41] for an Al 6061 plate with 304.8 mm in length, 152.4 mm in width and 6.35 mm in thickness. A 150 kHz excitation frequency is used in this study. One approach to model guided wave propagation in plate-like structures is to solve the governing wave equations with the appropriate boundary conditions; however, for complicated geometries the

complexity of the problem increases and hence computational techniques are used for analysis.

The ABAQUS model of the plate with sensor/actuator architecture is shown in Fig. 5.2. The maximum element size is determined by the wave length following Eqn. (5.8):

$$Maximum\ element\ size \leq \frac{L}{N} \tag{5.8}$$

where L denotes the wavelength and N can be chosen from 6 to 10 as recommended [121]. The FE mesh and displacement boundary condition is shown in Fig. 5.3. The plate with sensors/actuator is modeled as an assembly of three different parts, i.e., Al plate, piezoelectric transducer (PZT), and the adhesive layer. The material properties and the piezoelectric properties are listed in Table 5.1 [122]. Tie constraints are used to the surfaces between the plate/adhesive layer and the adhesive layer/PZT to simulate perfect bonding. Equation constraints are also used to ensure that the top and bottom surfaces of the PZTs have separate uniform electrical potential. The plate is initially modeled as an isotropic, homogeneous material, and continuum three-dimensional wedge elements (C3D6) are used for meshing. Piezoelectric transducers are defined as orthotropic materials and are meshed with continuum three-dimensional piezoelectric elements (C3D6E). The adhesive layer, which acts as the bonding between the piezoelectric transducers and the plate, is modeled as an isotropic, homogenous material, and continuum three dimensional wedge elements (C3D6) are used for meshing. An implicit dynamic scheme is used for the ABAQUS/Standard analysis. Since the implicit dynamic analysis is unconditionally stable, there is no

limit on the size of the time increment. Only accuracy governs the time increment in ABAQUS/Standard. However, in order to capture the small change on the PZT sensing signal due to the smallest element change, the time increment is determined to be less than the time required for the wave traveling through the smallest element. Overall, 36724 elements are used to model the plate. Considering the large number of elements and the small time increment, displacement at every ten steps and the electrical potential in the top surfaces of PZT1 and PZT2 (Fig. 5.2) are used to reduce the ABAQUS output database (odb) file.

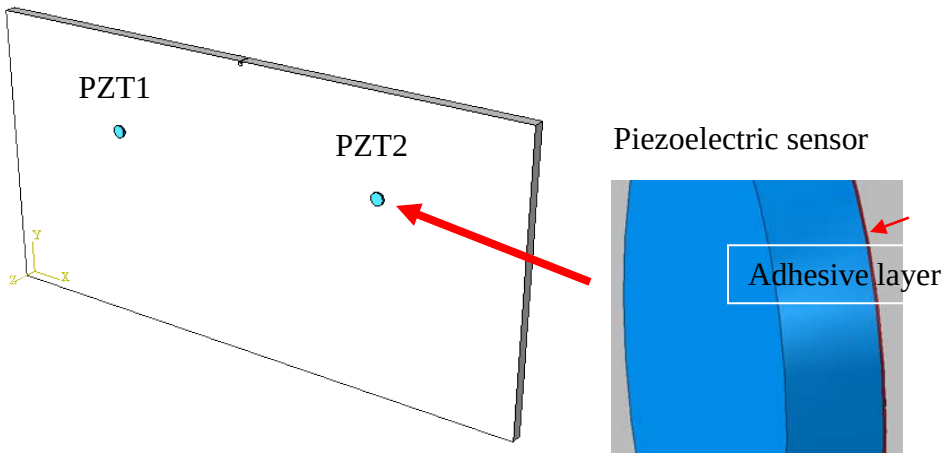

Figure 5.2 Finite element model of the Al 6061 plate with surface mounted piezoelectric sensors; Adhesive layer is also modeled.

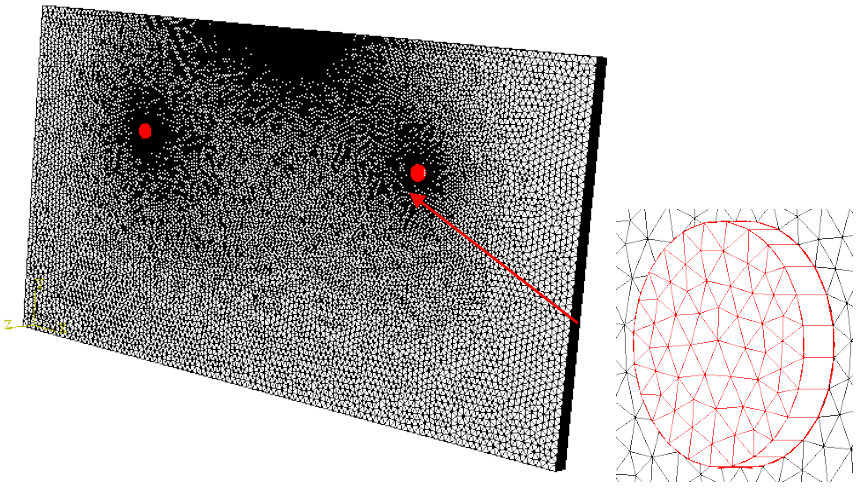

(a)

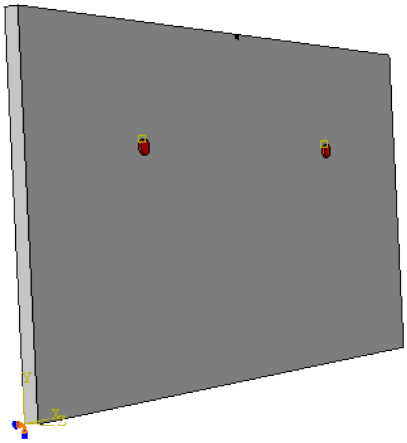

(b)

Figure 5.3 (a) Finite element mesh and (b) boundary condition used for the analysis

Table 5.1 Material properties of Al 6061, adhesive layer & piezoelectric sensors/actuator [122]

Elastic Properties		
	Young's Modulus (Pa)	Density (kg/m^3)
Al 6061	6.89E+10	2780
Layer	2.15E+09	1600

Piezoelectric Sensors/Actuator (PZT APC 850)

Elastic Properties					
Elastic Moduli (Pa)		Poisson's ratios		Shear Moduli (Pa)	
E1	6.30E+10	n12	0.301	G12	2.35E+10
E2	6.30E+10	n13	0.532	G13	2.30E+10
E3	5.40E+10	n23	0.532	G23	2.30E+10
Density (Kg/m^3)		7.50E+03			
Piezoelectric Properties (m/Volt)					
d1 11	0	d2 11	0	d3 11	-1.75E-10
d1 22	0	d2 22	0	d3 22	-1.75E-10
d1 33	0	d2 33	0	d3 33	4.00E-10
d1 12	0	d2 12	0	d3 12	0
d1 13	5.90E-10	d2 13	0	d3 13	0
d1 23	0	d2 23	5.90E-10	d3 23	0

Dielectric (Farad/m)					
D11	1.51E-08	D22	1.51E-08	D33	1.30E-08

5.3.2 Experiment Setup

An experiment was conducted using an aluminum plate to validate the proposed integrated multiscale damage/ wave propagation model. The dimension of the aluminum plate made of Al 6061 alloy is shown in Fig. 5.4. Two surface bonded PSI-5A4E type lead zirconate titanate (PZT) wafer transducers (diameter:

0.25″ and thickness: 0.04″) were used as actuators and sensors (Fig. 5.4). The data acquisition system used consisted of an arbitrary waveform generator (AWG), an 8-channel high-speed signal digitizer (DIG) and 16-channel multiplexer (Fig. 5.5). Using the 14-bit AWG, a tone-burst signal with a ± 10 peak-to-peak voltage was generated and used as an actuation signal. In the experiments, a 4.5 cycle tone-burst signal with the center frequency of 150 kHz was used as an input signal to generate only the fundamental modes, S_0 and A_0. The responses were measured by the PZTs used as sensors. The voltage outputs from sensing PZTs were measured by the DIG. The sampling rate of the DIG was set to 20 MS/sec. In order to improve the signal-to-noise ratio, the signals were measured 100 times and averaged.

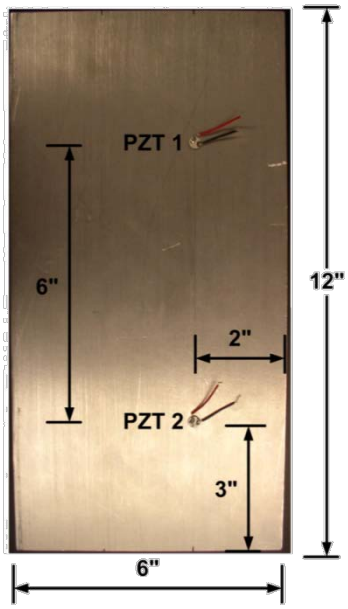

Figure 5.4 Dimensions of a plate made of Al 6061 in inches

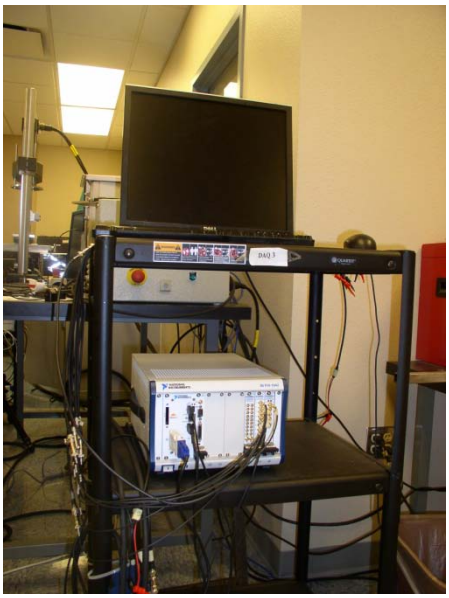

Figure 5.5 Data acquisition system

5.4 Results

Figure 5.6 shows the comparison between the experimental data and the lamb wave signal from the plate under no loading (referred to as the healthy plate) obtained using the FE without an RVE. Each signal contains three distinct wave groups. The first group is composed of direct S_0 mode and reflected S_0 mode from the upper boundary of the plate. The combination of direct A_0 and reflected S_0 from the left and right boundaries are shown in the second group. The third group includes multiple reflections from the boundaries. Figure 5.7 shows the propagation of lamb waves in the plate at three different times. Figure 5.7 (a) captures the arrival of the first wave group (direct S_0 and S_0 reflection from the top), and Fig. 5.7 (b) and Fig. 5.7 (c) show the other two aforementioned wave groups, respectively. While the amplitudes of both signals are in the same order, a time shift is observed between both signals. The possible causes of the discrepancy in the signals are imperfect bonding conditions and improper installation of the PZT sensors in the experiment. Temperature effects can also lead to time shift. It must be noted that the developed 3-D multiscale model does not account for temperature effect at this time.

Figure 5.8 shows the simulation results obtained from the plate modeled with and without the microscale RVE. As seen from this figure, the incorporation of the RVE in the FE modeling does not cause an obvious change on the sensing signal. This is expected as in the absence of loading, the microscale constitutive relations used in the RVE do not impact the elastic plate properties. Figure 5.9 shows noticeable change in signals obtained from the simulation after the

loading/unloading process is applied to the model. After subtracting the healthy signal (under no loading, as in Fig. 5.8) from the damage case signal, the attenuation of S_0 reflection from the upper plate boundary is observed. This is equivalent to amplitude increase in the S0 reflection from the upper boundary. The formation of a plastic zone affects the material properties by reducing density due to residual strain. Therefore, the plastic zone formed around the notch interacts with propagating waves in a different manner compared to the aluminum in pristine condition, resulting in an increase in reflection. However, the presence of mode conversion due to a plastic zone is not observed in the damage case. This is because the RVE used in the current model is uniform over the thickness. The results can be improved by using a full 3-D RVE in the analysis.

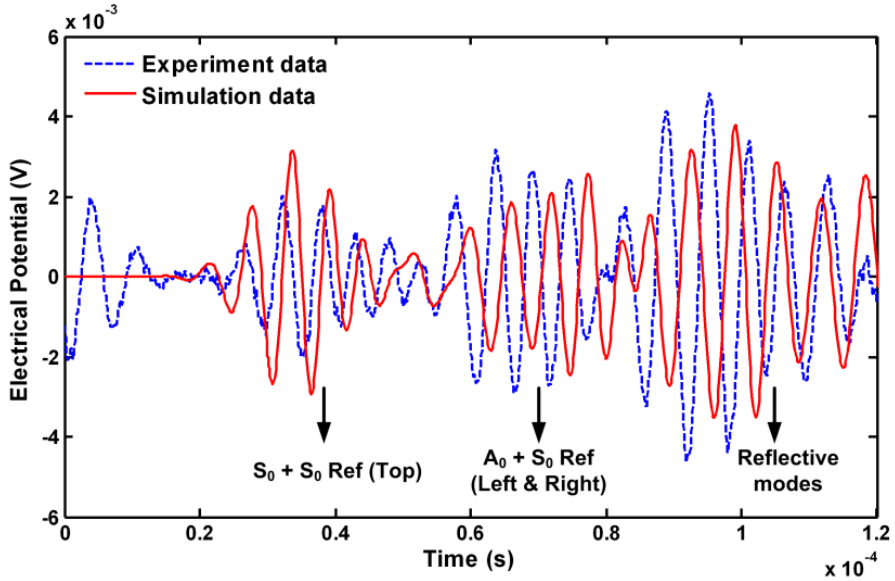

Figure 5.6 Comparison between simulated sensing signal with experiment data on healthy samples

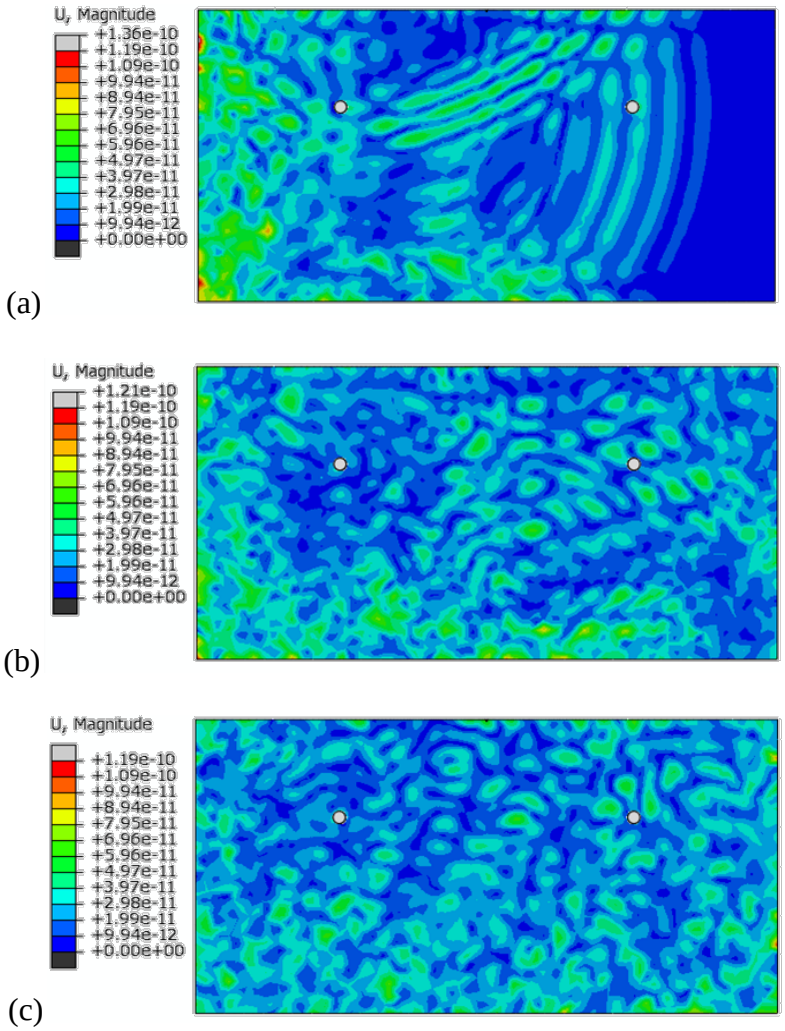

Figure 5.7 Propagation of Lamb waves in plate at three different times (Unit: m)

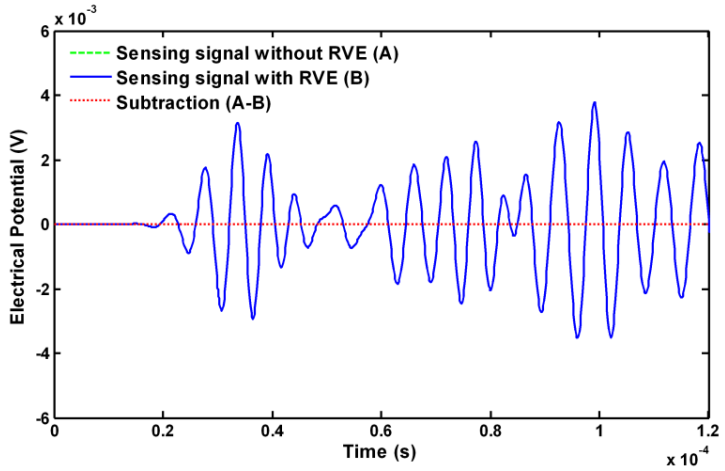

Figure 5.8 Comparison between sensing signals with/without RVE

(a)

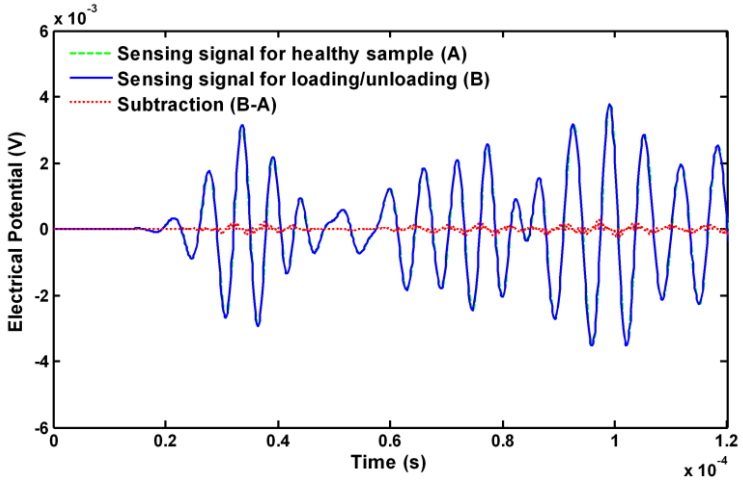

(b)

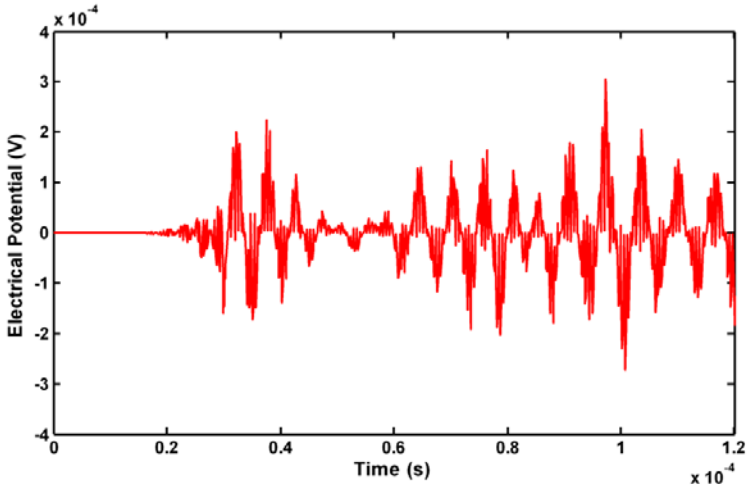

Figure 5.9 (a) Sensing signal comparison between loading/unloading case and healthy sample (b) Enlarged subtraction

Figure 5.10 shows the comparison between sensing signals in the plate after 10 cyclic loadings and the healthy sample. Additional change in the sensing signal is observed compared to just one cyclic loading case.

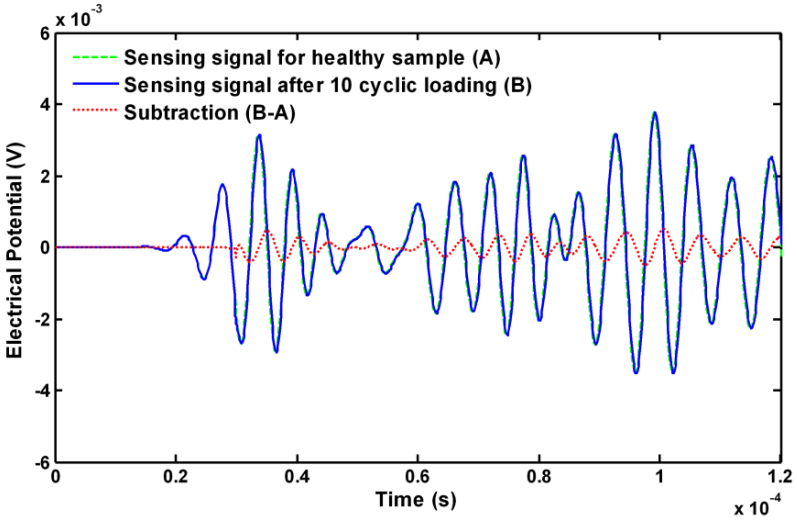

(a)

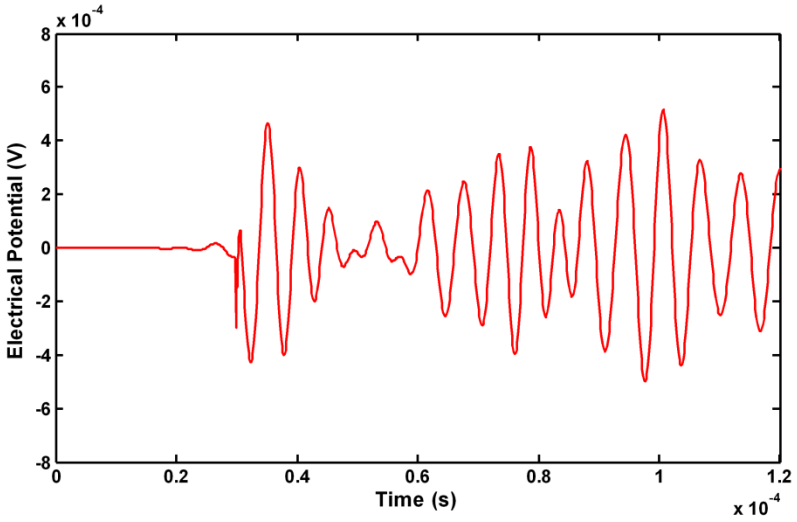

(b)

Figure 5.10 (a) Sensing signal comparison between 10 cyclic loading case and healthy sample (b) Enlarged subtraction

5.5 Concluding Remarks

The finite element based wave propagation model is incorporated into the multiscale model to characterize the effect of plastic zone and damage in metallic structures. The results indicate that the wave model can capture a slight change in

sensing signal due to plastic deformation and the accumulative damage in the plastic zone provided by the multiscale model. As the plastic zone increases, the change in the sensing signals between the healthy plate (no loading) and the plate subject to cyclic loading is more pronounced. Future work will include investigation of wave interaction due to material degradation from damage obtained from the multiscale model. Advanced algorithms for feature extraction from the sensor signals will be implemented for efficient damage detection.

Chapter 6

Summary and Future Directions

6.1 Summary

The focus of the research work presented in this dissertation is on the development of multiscale modeling for SHM. The goal is to develop a multiscale damage model accounting for microstructural features and provide data for information management and prognosis. The model developed has been tested on metallic specimens typically used in existing aerospace platforms. A size-dependent void model is also developed as a separate work for porous materials. Different effects including RVE size, defect area and distribution effects on material properties are investigated through numerical simulations.

The conclusions from different sections are summarized as follows:

1. A systematic methodology for multiscale stress analysis starting from material characterization is developed. Orientation and grain shape/size effects are considered through single crystal plasticity at the microscale level. A kinematic hardening law is added to the single crystal plasticity theory, which is important for fatigue analysis. A corresponding Fortran code is compiled with the UMAT subroutine developed by Huang [39]. The results show that the multiscale model is able to capture local anisotropic material behavior at grain level due to different grain orientations. Parametric study for determination of material parameters used in the Asaro's hardening rule [34] is performed. Three key

parameters are reevaluated by matching the simulation result to simple tension experimental results. Initial backstress caused by the manufacturing process is determined through experimentation. A second parametric study is carried out to correlate the kinematic hardening parameters with experimental data.

2. A microvoid model accounting for size and crystal orientation effects is developed. Applications of the size-dependent microvoid model are investigated for different shapes of voids under speicific activated slip systems. The results show that the flow stress strongly depends on microvoid growth rate and slip system orientations. Simulation studies are conducted to investigate the effects of RVE size and defect area fraction and distribution on the material elastic stiffness. The results indicate that as the RVE size increases, the elastic stiffness will converge. This convergence study provides one of the explanations for determination of current RVE size used in the research work. The results from the crack length effect study shows that crack propagation will accelerate material degradation in a quadratic manner. A comparison between the single microvoid and distributed multiple microvoids reveals that single microvoid is more harmful than distributed microvoids with the same area fraction.

3. A multiscale damage criterion that captures damage initiation at the microscale has been developed. This criterion focuses on the crack initiation in fatigue life. Experimental observation of a fatigue test on a lug

joint shows that fatigue life is significant prior to crack initiation as detected using available sensors and SHM techniques. Once the initiation occurs, crack growth rate is very high. It is evident therefore that damage initiation is very important for estimating structural fatigue life. Different techniques such as average methods and optimization approaches are used to construct the final damage index. Fatigue life up to a physically small crack (1 mm) is estimated from the damage model. The results show that the estimation of RVE failure at the lug joint hotspot under cyclic loading obtained from the multiscale damage criterion matches the number of cycles needed to get a 1 mm crack in the structural component from the experiment. In addition, the damage criterion has the capability to provide the potential directions for crack growth. Simulations for RVE failure estimation in the cruciform sample are performed by applying the damage model. Results indicate that the developed multiscale damage model is capable of providing accurate damage estimation and potential cracking directions for multiaxial loading condition.

4. The multiscale damage model is applied at structural hotspots to capture plastic zone and damage. Piezoelectric transducers and bonding layers are modeled in ABAQUS, and the 4.5 cycle excitation is used for the actuator. Wave propagation is simulated based on finite element analysis. The results show that plastic deformation and the accumulative damage in the plastic zone provided by the multiscale model will result in a change of sensing signals, and this change will increase as the plastic zone increases.

6.2 Innovative Nature of the Research

In this thesis, unique contributions are being made to multiscale damage modeling and virtual sensing techniques. They can be summarized as follows:

1. Multiscale modeling techniques start from real material characterization where all grain information, including grain size, shape, and orientations are obtained from the EBSD technique via Scanning Electron Microscope (SEM). Global stress-strain responses from the model are correlated with experimental data in both monotonic loading and cyclic loading.
2. A systematic procedure to create a two-length scale mesh associated with different constitutive models is developed using OOF to specify properties from microstructural images and by using Hypermesh to embed microstructural mesh into the structural component.
3. An energy based multiscale damage criterion is developed to incorporate crystal plasticity. Damage parameters are identified at every length scale. The associated damage variables are reduced from a damage tensor at microscale to a scalar at mesoscale. The developed criterion is able to provide local damage information as well as global damage information. It can also predict potential cracking directions simultaneously. The local damage information can be used to predict damage initiation and the global damage information is helpful to predict the RVE failure and cracking directions.
4. A size-dependent void is developed that takes account size effect and orientation effect. The orientation parameters and an intrinsic length are

introduced in the constitutive model. RVE size, defect area fraction, and distribution effects are studied through virtual experimental simulations, which help to better understand material degradation caused by defects.

5. A finite element based virtual sensing technique is developed. Multiscale modeling is used to provide damage information for the virtual sensing. The advantages of the virtual sensing technique are 1) it is noise-free, which makes it more sensitive; 2) it is easily repeatable; and 3) it costs less than other methods.

6.3 Future Directions

The following directions can be undertaken as a continuation of this research:

1. In order to implement online SHM and prognosis, the computational efficiency of the multiscale modeling needs to be enhanced. Improved algrithms for the crystal plasticity theory should be developed to reduce UMAT subrountine computational time.
2. A statistical microstructure builder is neccersary to reduce the sample scans of the material in engineering applications. The objective for the microstructure builder will be forcused on solving the problem on how to statistically generate a representative microstructure based on a few material sample scans.
3. Element deletion is required to be implemented for progressive damage simulations. The function of element deletion is to automatically perform the task of deleting elements when the damage index of the element meets certain criterion. This can be implemented via a user-defined element

(UEL) subroutine that interfaces with the commercial FE software ABAQUS.

4. Better sensing signal processing techniques should be developed. For small damage or plastic zone, the change in simulated sensing signals is very small. Most current signal processing techniques cannot extract useful features from the signals. Thus, signal processing techniques suitable for small damage or plastic zone are an imperative.
5. Formulas that directly relate the damage index obtained from the multiscale damage model to the material properties should be derived. This can be used in virtual sensing simulation to simulate the wave propagation relating to the material degradation caused by damage.
6. Other effects such as thermal effect can be included in the multiscale damage model to expand its application field. For example, thermal effect is crucial in naval structures. Therefore, the extended multiscale damage model can be used for damage prediction in those structures.

REFERENCES

[1] Chang, P., & Liu, S. (2003). Recent Research in Nondestructive Evalution of Civil Infrastructures. *Journal of materials in civil engineering* , 298-304.

[2] Frangopol, D., & Peil, U. (2006). Life-cycle Assessment and Life Extension of Structures via Innovative Methods. *Proceedings of the Third European Workshop on Structural Health Monitoring* , 49-57.

[3] B. Glisic & D. Inaudi (2008). Fibre Optic Methods for Structural Health Monitoring. *Wiley*. ISBN 978-0-470-06142-8

[4] Giurgiutiu, V. (2008). Structural Health Monitoring with Piezoelectric Wafer Active Sensors. *Elsevier*, ISBN 978-0-12- 088760-6

[5] Farrar, C. R., Park, G., Allen, D. W. and Todd, M. D. (2006), Sensor network paradigms for structural health monitoring. *Structural Control and Health Monitoring*, 13: 210–225. doi: 10.1002/stc.125

[6] Mohanty, S., Chattopadhyay, A., Wei, J and Peralta, P., "Unsupervised Time-Series Damage State Estimation of Complex Structure Using Ultrasound Broadband Based Active Sensing", 2010, *Structural Durability & Health Monitoring Journal*, vol.130, no.1, pp.101-124

[7] Liu, Y., Mohanty, S., Chattopadhyay, A., "Condition Based Structural Health Monitoring and Prognosis of Composite Structures under Uniaxial and Biaxial Loading, 2010, *Journal of Nondestructive Evaluation*, Volume 29, Number 3, 181-188

[8] Chattopadhyay, A., Peralta, P., Papandreou-Suppappola, A., et al., "A multidisciplinary approach to structural health monitoring and damage prognosis of aerospace hotspots", Aeronautical Journal, Vol. 113, No.1150, 2009, pp. 799-810

[9] Park, S. Yun, C. B. & Inman, D. J., "Structural Health Monitoring Using Electro-mechanical Impedance Sensors", 2008, *Fatigue & Fracture of Engineering Materials & Structures*, Vol. 31, No. 8, 714-724

[10] Majumder, M., Gangopadhyay, T. K. & Chakraborty, A. K., et al., "Fibre Bragg Gratings in Structrual Health Monitoring – Present Status and Applications", 2008, *Sensors and Actuators A-Physical*, Vol.147, No. 1, 150-164

[11] S. Das, A. Chattopadhyay, and X. Zhou, "Acoustic based structural health monitoring for composites using optimal sensor placement: Analysis and experiments", 2009, *Journal of Reinforced Plastics and Composites*, vol. 28, no. 1, pp. 83–97

[12] S. Soni, S. B. Kim, and A. Chattopadhyay, "Reference-free fatigue crack detection, localization and quantification in lug joints", in 51st AIAA/ASME/ASCE/AHS/ASC Structures, Structural Dynamics, and Materials Conference, 2010.

[13] U. S. Air Force Scientific Advisory Board (1992). *Report of the AdHoc Committee on Air Force Aircraft Jet Engine Manufacturing and SAF/AQQS*. Washington, D.C.: The pentagon.

[14] Horstemeyer M.F., "Multiscale Modeling: A Review," Practical Aspects of Computational Chemistry, ed. J. Leszczynski and M.K. Shukla, Springer Science+Business Media, pp. 87-135, 2009

[15] Benssousan, A., Lions, J. L., Papanicoulau, G., 1978. Asymptotic analysis for periodic structures. North Holland, Amsterdam.

[16] Hao, S., Liu, W.K., Moran, B., Vernerey, F., Olson, G.B., 2004. Multiple-scale constitutive model and computational framework for the design of ultra-high strength, high toughness steels. Comput. Meth. Appl. Mech. Eng. 193, 1865.

[17] Liu, W.K., Karpov, E.G., Zhang, S., Park, H.S., 2004a. An introduction to computational nanomechanics and materials. Comput. Methods Appl. Mech. Eng. 193, 1529 – 1578.

[18] Liu, W.K., Hao, S., Vernerey, F.J., Kadowaki, H., Park, H., Qian, D., 2004b. Multi- scale analysis and design in heterogeneous system. Presented at VII International Conference on Computational Plasticity (COMPLAS VII).

[19] Liu, W.K., Karpov, E.G., Parks, H.S., 2006. Nano Mechanics and Materials, Theory, Multiscale Methods and Applications. Wiley, New York.

[20] Ghosh, S., Valiveti, D. M., Harris, S. J., and Boileau, J., “A domain partitioning based pre-processor for multi-scale modelling of cast aluminium alloys,” Modelling Simul. Mater. Sci. Eng. 14 (2006) 1363-1396.

[21] Chao H, Moorthy S and Ghosh S 2004 A Voronoi cell finite element model for ductile damage in MMCs Materials Processing and Design: Modeling, Simulation and Application: Proc. NUMIFORM (Columbus, Ohio, USA) ed S Ghosh et al (New York: AIP Publishers) pp 1893 – 99

[22] Ewing, J. A. and Humfrey, J. C. W., “The Fracture of Metals under Repeated Alternations of Stress,” Philosophical Transactions of the Royal Society, Vol. 210, 1903, pp. 241-253

[23] Production Processes (1992). United States Air Force Scientific Advisory Board, Report of the AdHoc Committee on Air Force Aircraft Jet Engine Manufacturing and SAF/AQQS: the Pentagon, Washington, D.C

[24] Socie DF, Marquis GB. Multiaxial fatigue. Warendale, PA: SAE International; 2000, ISBN 0-7680-0453-5

[25] Gough, H. J., Pollard, H. V., and Clenshaw, W. J., " Some Experiments on the Resistance of Metals Under Combined Stress," Ministry of Supply, Aeronautical Research Council Reports and Memoranda No. 2522, HMSO, London, 1951

[26] Gough, H. J., and Pollard, H. V., "The strength of metals under combined alternating stresses," *Proc. Inst. Mech. Engrs*, Vol. 131 (1935), pp.3-103.

[27] Taylor, G. (1934). The mechanism of plastic deformation of crystals. Part I.-theoretical . *Proc. R. Soc. London* , 362-387.

[28] Taylor, G. (1938). Plastic strain in metals. *J. Inst. Met.* , 307-325.

[29] Hill, R. (1966). Generalized Constitutive Relations for Incremental Deformation of Metal Crystals by Multislip. *J. Mech. Phys. Solids* , 95-102.

[30] Rice, J. (1971). Inelastic Constitutive Relations for Solids: An Internal-Variable Theory and its Application to Metal Plasticity . *J. Mech. Phys. Solids* , 433-455.

[31] Hill, R., & Rice, J. R. (1972). Constitutive Analysis of Elastic-Plastic Crystals at Arbitrary Strain. J. Mech. Phys. Solids , 401-413.

[32] Asaro, R., & Rice, J. (1977). Strain Localization in Ductile Single Crystals. J. Mech. Phys. Solids , 309-338.

[33] Asaro, R. (1983). Crystal Plasticity. J. Appl. Mech , 921-934.

[34] Asaro, R. (1983). Micromechanics of Crystals and Polycrystals. Adv. Appl. Mech. , 1-115.

[35] Bassani, J. (1994). Plastic Flow of Crystals. Advances in Applied Mechanics, 191-258.

[36] Horstemeyer, M., & McDowell, D. (1998). Modeling effects of dislocation substructure in polycrystal elastoplasticity. Mech. Mater , 145-163.

[37] Horstemeyer, M., McDowell, D., & McGinty, R. (1999). Design of experiments for constitutive model selection: Application to polycrystal elastoplastictiy. Modeling and Simulation in Mats. Sci. Engng. , 253-273.

[38] Peirce, D., Asaro, R., & Needleman, A. (1982). An analysis of Nonuniform and Localized Deformation in Ductile Single Crystals. Acta Metall. , 1087-1119.

[39] Huang, Y. (1991). A User-Material Subroutine Incorporating Single Crystal Plastictiy in the ABAQUS Finite Element Program. Harvard University: Mech Report 178, Division of Engineering and Applied Sciences.

[40] Peirce, D., Shih, C., & Needleman, A. (1984). A Tangent Modulus Method for Rate Dependent Solids. Computers & Structures , 875-887.

[41] Abaqus Version, 6.7. (2007). Abaqus/CAE and Abaqus/Standard. Simulia World Headquarters, Providence.

[42] Farrar, C., Sohn, H., Hemez, F., Anderson, M., Bement, M., Cornwell, P., Doebling, S., Schultze, J., Lieven, N., Robertson, A., 2003. Damage Prognosis: Current Status and Future Needs. Los Alamos National Laboratory.

[43] Singh, G.K., Kazzaz, S.A.S.A., 2003. Induction machine drive condition monitoring and diagnostic research - a survey. Electric Power Systems Research 64, 145-158.

[44] Rice, J.R., Tracey, D.M., 1969. On the ductile enlargement of voids in triaxial stress fields. J Mech Phys Solids, 17, 201–217 .

[45] Gurson, A.L., 1977. Continuum theory of ductile rupture by void nucleation and growth: Part I – yield criteria and flow rules for porous ductile media. J. Engrg. Mater. Technol. 99, 2–15.

[46] Tvergaard,V., 1990. Material failure by void growth to coalescence. Adv Appl Mech, 27, 83–147.

[47] Fleck, N.A., Muller, G.M., Ashby, M.F., et al., 1994. Strain gradient plasticity: theory and experiment. Acta Metall Mater, **42**, 475–487.

[48] Stolken, J.S., Evans, A.G., 1998. A microbend test method for measuring the plasticity length scale. Acta Mater, **46**, 5109–5115.

[49] Shrotriya, P., Allameh, S.M., Lou, J., et al., 2003. On the measurement of the plasticity length scale parameter in LIGA nickel foils. Mech Mater, **35**, 233–243.

[50] Haque, M.A., Saif, M.T.A., 2003. Strain gradient effect in nanoscale thin films. Acta Mater, **51**, 3053–3061.

[51] Stelmashenko, N.A., Walls, M.G., Brown, L.M., et al., 1993. Microindentation on W and Mo oriented single crystals: an STM study. Acta Metall Mater, **41**, 2855–2865.

[52] McElhaney, K.W., Vlassak, J.J., Nix, W.D., 1998. Determination of indenter tip geometry and indentation contact area for depth-sensing indentation experiments. J Mater Res, **13**, 1300–1306.

[53] Saha, R., Xue, Z.Y., Huang, Y., et al., 2001. Indentation of a soft metal film on a hard substrate: strain gradient hardening effects. J Mech Phys Solids, **49**, 1997–2014.

[54] Lloyd, D.J., 1994. Particle reinforced aluminum and magnesium matrix composites. Int Mater Rev, **39**, 1–23.

[55] Xue, Z., Saif,T.M.A.,Huang,Y., 2002. The strain gradient effect in microelectro-mechanical systems (MEMS). J Microelectromechanical Systems, **11**, 27–35.

[56] Douglass, M.R., 1998. Lifetime estimates and unique failure mechanisms of the digital micromirror device (MDM). In: Annual Proceedings-Reliability Physics Symposium (Sponsored by IEEE), Mar 31-Apr **2**, 9–16.

[57] Jiang, H., Huang, Y., Zhuang, Z., et al., 2001. Fracture in mechanismbased strain gradient plasticity. J Mech Phys Solids, **49**, 979–993.

[58] Schlueter, N., Grimpe, F., Bleck,W. et al., 1996. Modeling of the damage in ductile steels. Comp Mater Sci, **7**, 27–33.

[59] Khraishi, T.A., Khaleel, M.A., Zbib, H.M., 2001. Parametric-experimental study of void growth in superplastic deformation. Int J Plasticity, **17**, 297–315.

[60] Fond, C., Lobbrecht, A., Schirrer, R., 1996. Polymers toughened with rubber microspheres:An analytical solution for stresses and strains in the rubber particles at equilibrium and rupture. Int J Fracture, **77**, 141–159.

[61] Fleck, N.A.,Hutchinson, J.W., 1997. Strain gradient plasticity. In: Hutchinson JW and Wu TY eds. Advances in Applied Mechanics, New York: Academic Press, **33**, 295–361.

[62] Shu, J.Y., 1998. Scale-dependent deformation of porous single crystals. Int J Plasticity, **14**: 1085–1107.

[63] Huo, B., Zheng, Q.S., Huang, Y., 1999. A note on the effect of surface energy and void size to void growth. Euro J Mech -A/Solids, **18**, 987–994.

[64] Zhang, K.S., Bai, J.B., Francois, D., 1999. Ductile fracture of materials with high void volume fraction. Int J Solids Struct, **36**, 3407–3425.

[65] Zhang, S., Hsia, K.J., 2001. Modeling the fracture of a sandwich structure due to cavitation in a ductile adhesive layer. ASME Trans. J Appl Mech, **68**, 93–100.

[66] Liu, B., Qiu, X., Huang, Y., et al., 2003. The size effect on void growth in ductile materials. J Mech Phys Solids, **51**, 1171–1187.

[67] Wen, J., Huang,Y., Hwang, K.C., et al., 2005. The modified Gurson model accounting for the void size effect. Int J Plasticity, **21**(2), 381–395.

[68] Wen, J., Hwang, K.C., Huang,Y., 2005. Extension of the gurson model accounting for the void size effect. Acta Mech Sinica 21, 142-150.

[69] Suresh, S., 1998. Fatigue of Materials. Cambridge University Press.

[70] Solanki, K., Horstemeyer, M.F., Baskes, M.I., Fang, H., 2005. Multiscale study of dynamic void collapse in single crystals. Mechanics of Materials 37 (2-3), 317-330.

[71] Bailey, J.E., Hirsch, P.B., 1960. The Dislocation Distribution, Flow Stress, and Stored Energy in Cold-Worked Polycrystalline Silver. Philosophical Magazine 5 (53), 485-&.

[72] Wiedersich, H., 1964. Hardening Mechanisms + Theory of Deformation. Jom-Journal of Metals 16 (5), 425-&.

[73] Gao, H., Huang, Y., Nix, W.D., Hutchinson, J.W., 1999. Mechanism-based strain gradient plasticity - I. Theory. Journal of the Mechanics and Physics of Solids 47 (6), 1239-1263.

[74] Huang, Y., Gao, H., Nix, W.D., Hutchinson, J.W., 2000a. Mechanism-based strain gradient plasticity - II. Analysis. Journal of the Mechanics and Physics of Solids 48 (1), 99-128.

[75] Huang, Y., Qu, S., Hwang, K.C., Li, M., Gao, H., 2004. A conventional theory of mechanism-based strain gradient plasticity. International Journal of Plasticity 20 (4-5), 753-782.

[76] Bishop, J.F.W., Hill, R., 1951a. A theoretical derivation of the plastic properties of a polycrystalline face-centered metal. Philos. Mag. 42, 1298–1307.

[77] Bishop, J.F.W., Hill, R., 1951b. A theory of plastic distortion of a polycrystalline aggregate under combined stresses. Philos. Mag. 42, 414-427.

[78] Kocks, U.F., 1970. Relation between Polycrystal Deformation and Single-Crystal Deformation. Metallurgical Transactions 1 (5), 1121-&.

[79] Arsenlis, A., Parks, D.M., 1999. Crystallographic aspects of geometrically-necessary and statistically-stored dislocation density. Acta Materialia 47 (5), 1597-1611.

[80] Huang, Y., Xue, Z., Gao, H., Nix, W.D., Xia, Z.C., 2000b. A study of microindentation hardness tests by mechanism-based strain gradient plasticity. Journal of Materials Research 15 (8), 1786-1796.

[81] Xue, Z., Huang, Y., Hwang, K.C., Li, M., 2002a. The influence of indenter tip radius on the micro-indentation hardness. Journal of Engineering Materials and Technology-Transactions of the Asme 124 (3), 371-379.

[82] Xue, Z., Huang, Y., Li, M., 2002b. Particle size effect in metallic materials: a study by the theory of mechanism-based strain gradient plasticity. Acta Materialia 50 (1), 149-160.

[83] Han, C.S., Gao, H.J., Huang, Y.G., Nix, W.D., 2005a. Mechanism-based strain gradient crystal plasticity - I. Theory. Journal of the Mechanics and Physics of Solids 53 (5), 1188-1203.

[84] Han, C.S., Gao, H.J., Huang, Y.G., Nix, W.D., 2005b. Mechanism-based strain gradient crystal plasticity - II. Analysis. Journal of the Mechanics and Physics of Solids 53 (5), 1204-1222.

[85] Nix, W.D., Gao, H.J., 1998. Indentation size effects in crystalline materials: A law for strain gradient plasticity. Journal of the Mechanics and Physics of Solids 46 (3), 411-425.

[86] Nemat-Nasser, S., Okinaka, T., Nesterenko, V., Liu, M.Q., 1998. Dynamic void collapse in crystals: computational modelling and experiments. Philosophical Magazine a-Physics of Condensed Matter Structure Defects and Mechanical Properties 78 (5), 1151-1174.

[87] Huang, M.S., Li, Z.H., 2005. Size effects on stress concentration induced by a prolate ellipsoidal particle and void nucleation mechanism. International Journal of Plasticity 21 (8), 1568-1590.

[88] Huang, M.S., Li, Z.H., Wang, C., 2005. Coupling effects of void size and void shape on the growth of prolate ellipsoidal microvoid. Acta Mechanica Sinica 21 (3), 272-277.

[89] Huang, Y., 1991. Accurate Dilatation Rates for Spherical Voids in Triaxial Stress-Fields. Journal of Applied Mechanics-Transactions of the Asme 58 (4), 1084-1086

[90] Stephens, R.I., Fatemi, A., Stephens, R.R. &Fuchs, H.O., *Metal fatigue in engineering, 2nd Edition*, Wiley, 2000.

[91] Frost, N.E., Marsh, K.J. & Pook, L.P., *Metal fatigue*. Clarendon Press, Oxford, 1974.

[92] Kocanda, S., *Fatigue failures of metals*. Sijthoff and Noordhoff International Publishers, Netherlands,1978.

[93] Klesnil, M. & Lukas, P., *Fatigue of metallic materials*, Elsevier Science & Technology, 1992.

[94] Forsyth, P.J.E., *The physical basis of metal fatigue*, American Elsevier Pub Co, 1969.

[95] Schijve, J., "Significance of fatigue cracks in micro-range and macro-range," ASTM STP 415, 1967, pp.415–459.

[96] Shang, D.G., Yao, W.X. & Wang, D.J., "A new approach to the determination of fatigue crack initiation size," Int J Fatigue, Vol. 20, No. 9, 1998,pp.683–687.

[97] Miller, K.J., "The behavior of short fatigue cracks and their initiation. Part I. A review of two recent books," Fatigue Fract Eng Mater Struct, Vol.10, 1987, pp.75–91.

[98] Miller, K.J., "The behavior of short fatigue cracks and their initiation. Part II. A general summary," Fatigue Fract Eng Mater Struct, Vol. 10, 1987, pp. 93–113.

[99] Ritchie, R.O. & Lankford, J., " Small fatigue cracks: a statement of the problem and potential solutions," Mater Sci Eng, Vol. 84, No. 1-2, 1989, pp.11–16.

[100]Luo, C., Wei, J., Parra-Garcia, M., Chattopadhyay, A. and Peralta, P.,"Fatigue Damage Prediction in Metallic Materials Based on Multiscale Modeling," AIAA Journal, Vol. 47, 2009, pp. 2567-2576.

[101]Jiang, Y., "A fatigue criterion for general multiaxial loading", *Fatigue Fract. Engng. Mater. Struct.* Vol. 23, No. 1, 2000, pp. 19-32.

[102]Ding, F., Zhao, T., Jiang, Y., "A study of fatigue crack growth with changing loading direction", *Engng. Fract. Mech*, Vol. 74, No. 13, 2007, pp. 2014-2029

[103]Kalnaus, S., Jiang, Y., “Fatigue life prediction of copper single crystals using a critical plane approach”, *Engng. Fract. Mech*, Vol. 73, No. 6, 2006, pp. 684-696

[104]Lemaitre, J., and Desmorat, R., Engineering Damage Mechanics, Springer Berlin Heidelberg New York, 2005.

[105]Laird, C., “The Influence of Metallurgical Structure on the Mechanisms of Fatigue Crack Propagation,” *Fatigue Crack Propagation, ASTM STP 415*, Philadelphia, 1967, pp. 131-180.

[106]Neumann, P., "New Experiments Concerning the Slip Processes at Propagating Fatigue Cracks-I." *Acta metall*. 22, 1974a, pp. 1155-1165

[107]Haftka, R.T. & Gürdal, Z., “Elements of Structural Optimization,” Netherlands: Kluwer Academic Publishers, 1992.

[108]Garruchet, S., Politano, O., Salazar, J.M. and Montesin, T., “An empirical method to determine the free surface energy of solids at different deformations and temperature regimes: An application to Al,” *Surface Science*, Vol. 586, Issues 1-3, 20 July 2005, pp. 15-24.

[109]Farrar, C. R., Allen, D. W., Park, G., Ball, S. and Masquelier, M. P., “Coupling sensing hardware with data interrogation software for structural health monitoring”, *Shock and Vibration*, Vol. 13, No. 4-5, 2006, pp. 519-530

[110]Sohn, H., et al., " A Review of Structural Health Monitoring Literature: 1996-2001,” Los Alamos National Laboratory report in preparation, 2002

[111]Giurgiutiu, V. and Cuc, A., “Embedded Non-destructive Evaluation for Structural Health Monitoring, Damage Detection, and Failure Prevention”, *The Shock and Vibration Digest*, Vol. 37, No. 2, March 2005, pp. 83-105

[112]Papazian, J.M.; Anagnostou, E.L.J.; Engel, S.; Fridline, D.; Hoitsma, D.; Madsen, J.; Nardiello, J.; Silberstein, R.P.; Welsh, G.; Whiteside, J.B.; , "SIPS, A Structural Integrity Prognosis System," *Aerospace Conference*, 2007 IEEE , pp.1-10

[113]Luo, C., Chattopadhyay, A., “Prediction of Fatigue Crack Initial Stage Based on a Multiscale Damage Criterion,” International Journal of Fatigue, Vol. 33, Issue 3, March 2011, Pages 403-413, doi:10.1016/j.ijfatigue.2010.09.014

[114]Luo, C., Mohanty, S. and Chattopadhyay, A., “A Study of Fatigue Damage Growth under Biaxial Loading Based on Multiscale Damage Criterion”,

51th AIAA/ASME/ASCE/AHS/ASC Structures, Structural Dynamics, and Materials Conference, 12–15 April 2010, Orlando, Florida USA.

[115]Chattopadhyay, A., Peralta, P., Papandreou-Suppappola, A., et al., "A multidisciplinary approach to structural health monitoring and damage prognosis of aerospace hotspots", Aeronautical Journal, Vol. 113, No.1150, 2009, pp. 799-810

[116]Santoni, G. B.; Yu, L.; Xu, B.; Giurgiutiu, V. (2007) "Lamb Wave Mode Tuning of Piezoelectric Wafer Active Sensors for Structural Health Monitoring", ASME Journal of Vibration and Acoustics, Vol. 129, No. 6, pp. 752-762, Dec. 2007

[117]Rizzo, P., Cammarata, M., Dutta, D., Sohn, H. and Harries, K., "An unsupervised learning algorithm for fatigue crack detection in waveguides," *Smart Structures and Materials* 18, 025016 (2009).

[118]Kim, S. B. and Sohn, H., "Instantaneous reference-free crack detection based on polarization characteristics of piezoelectric materials," *Smart Mater. Struct.*, Vol. 16, 2375, 2007.

[119]Soni, S. O., Kim, S. B. and Chattopadhyay, A., "Fatigue crack detection and localization using reference-free method," Proc. of SPIE 7648, 2010.

[120]Luo, C., Wei, J., Garcia, M., Chattopadhyay, A. and Peralta, P.,"A Multiscale Model for Fatigue Damage Prediction in Metallic Materials,"49th AIAA/ASME/ASCE/AHS/ASC Structures, Proc. Structural Dynamics and Materials Conference, Schaumburg, Illinois, April 2008

[121]Yang, C., Ye, L., Su, Z. and Bannister, M., "Some aspects of numerical simulation for Lamb wave propagation in composite laminates", *Composite Structures*, Vol. 75, Issues 1-4, September 2006, pp. 267-275

[122]Soni, S., Das, S. and Chattopadhyay, A., "Simulation of Damage-features in a Lug Joint using Guided Waves", *Journal of Intelligent Material Systems and Structures,* Vol. 20, No. 12, 2009, pp. 1451-1464